
Interface Simulation of All-Solid-State Lithium-ion Thin Film Battery

Zur Erlangung des akademischen Grades Doktor-Ingenieur (Dr.-Ing.)

Genehmigte Dissertation von Yao Liu aus Hubei, China

Tag der Einreichung: 28. September 2021, Tag der Prüfung: 14. Dezember 2021

1. Gutachten: Prof. Dr. Bai-Xiang Xu, Technische Universität Darmstadt

2. Gutachten: Prof. Dr. Wolfram Jaegermann, Technische Universität Darmstadt

Darmstadt – D 17



TECHNISCHE
UNIVERSITÄT
DARMSTADT

Materials and Earth
Sciences Department

Mechanics of Functional
Materials

Interface Simulation of All-Solid-State Lithium-ion Thin Film Battery

Accepted doctoral thesis by Yao Liu

1. Review: Prof. Dr. Bai-Xiang Xu, Technische Universität Darmstadt
2. Review: Prof. Dr. Wolfram Jaegermann, Technische Universität Darmstadt

Date of submission: 28. September 2021

Date of thesis defense: 14. Dezember 2021

Darmstadt – D 17

Bitte zitieren Sie dieses Dokument als:

URN: urn:nbn:de:tuda-tuprints-206626

URL: <http://tuprints.ulb.tu-darmstadt.de/20662>

Dieses Dokument wird bereitgestellt von tuprints,
E-Publishing-Service der TU Darmstadt
<http://tuprints.ulb.tu-darmstadt.de>
tuprints@ulb.tu-darmstadt.de

CC BY-SA 4.0 International

Erklärungen laut Promotionsordnung

§8 Abs. 1 lit. c PromO

Ich versichere hiermit, dass die elektronische Version meiner Dissertation mit der schriftlichen Version übereinstimmt.

§8 Abs. 1 lit. d PromO

Ich versichere hiermit, dass zu einem vorherigen Zeitpunkt noch keine Promotion versucht wurde. In diesem Fall sind nähere Angaben über Zeitpunkt, Hochschule, Dissertationsthema und Ergebnis dieses Versuchs mitzuteilen.

§9 Abs. 1 PromO

Ich versichere hiermit, dass die vorliegende Dissertation selbstständig und nur unter Verwendung der angegebenen Quellen verfasst wurde.

§9 Abs. 2 PromO

Die Arbeit hat bisher noch nicht zu Prüfungszwecken gedient.

Darmstadt, 28. September 2021

Yao Liu

Acknowledgement

First and foremost, Prof. Bai-Xiang Xu and Prof. Wolfram Jaegermann are sincerely appreciated since they offer me the precious opportunity to study at TU Darmstadt. Then, I would like to express my gratitude to Prof. Xu again and Dr. René Hausbrand for their kind supervision in recent years. They devoted many efforts to guide me to learn independent thinking, scientific criticizing, and manuscript writing. I am truly grateful for your guidance, inspiration, and all the opportunities you have given me. Thank you for always being available whenever I need help.

Besides my supervisors, I would like to express my gratitude to Dr. Ying Zhao and Dr. Peter Stein for their helpful discussions and constructive suggestions in battery modelling. My sincere thanks also give to Dr. Yang-Bin Ma for his assistance with my life in Germany and the insightful reviews on handwriting. Moreover, I would like to acknowledge Dr. Yang Bai and Yangyiwei Yang, who provide me with many supports in the finite element computation and the MOOSE software. Thanks a lot to Dr. Zhen Liu, Dr. Zi-Qi Zhou, and Hamid Nouri for the interesting lunch talking every day, and it greatly broadens my horizon. I am sincerely grateful to Dr. Xian-Dong Zhou, Dr. Min Yi, Dr. Shuai Wang, Dr. Habib Pouriayevali, Dr. Dagmar Eder-Goy, Wei Liu, Qi-Hua Gong, Bin-Bin Lin, Reimuth Christoph, and other colleagues for their help from all aspects and the wonderful working atmosphere in the MFM (Mechanics of Functional Materials) group. As well, I am quite grateful to all members of the surface science group for their fruitful scientific discussions and practical advice. Especially, many thanks to Thimo Ferber, for your expert help regarding the XPS operation and analysis. I sincerely appreciate my friends Zhuo Na, Bing-Shu Zhang, Dr. Yao Feng and Wei Li for their assistance whenever I had a problem in Germany. To all of my friends, new and old, thank you for all the help, I wish you all the best of luck!

I would like to acknowledge both the Chinese Scholarship Council (CSC) and Deutsche Forschungsgemeinschaft (DFG) for their financial support. Lichtenberg high performance computer of TU Darmstadt is also appreciated for the calculation resources, which provided reliable facilities to carry out my research. I dedicate this work to my lovely wife Dr. Wen-Bei Yu and our parents, for your constant support and encouragement throughout my Ph.D. studies. Travelling with her in Europe was the happiest time, and it will be the most precious memory of all my life. Last, I sincerely wish you could succeed in your next scientific research career.

Abstract

Lithium-ion batteries have attracted extensive research attention in the past decades, and have become the premier energy storage technology due to their high energy density and long cycling life. Up to date, commercial lithium-ion batteries heavily rely on liquid organic carbonate electrolytes. Nevertheless, liquid electrolytes can trigger the explosion after the thermal runaway in batteries, and are electrochemically unstable at high voltage. To address these issues, all-solid-state batteries (ASSBs) are widely researched as promising alternatives. Even though ASSBs show impressive merits in comparison to the conventional LIBs, the solid/solid interface remains one of the main bottlenecks that limit currently its application. Particularly, the influence of the space charge layer on the total interface impedance remains controversial in the community. Different theoretical electrochemical models have been employed to help understand the solid/solid interface in ASSBs.

The electrochemical models in the literature have paved a solid fundament and have helped to gain important insights on the electrochemical behavior of the interface, but can be improved in different aspects. For instance, the exchange current is assumed to be an important input parameter in these models and is widely employed in the dynamic study of ASSBs. But it is difficult to experimentally determine the exchange current. The first contribution of this thesis is devoted to intrinsic interface equilibrium study, which allows both the determination of exchange current and the interface resistance from fundamental material properties. Thereby, an advanced electrochemical model was proposed on the basis of the Planck-Nernst-Poisson (PNP) and the Frumkin-Butler-Volmer (FBV) theories. In particular, it takes the electrical double layer (EDL) structure and the unoccupied regular lattice sites (vacancies) into account, as lithium-ion migration at the solid/solid interface is limited by the available lattice sites. The model is implemented using the finite element method and applied to simulate a model thin-film half-cell consisting of LiCoO_2 as cathode and LiPON as solid electrolyte. Numerical results based on this model have demonstrated its capability and are verified well against theoretical and experimental results. They show that vacancies play an important role in the concentration and the electrostatic potential distributions in the space charge layer region. The influence on concentration and electrostatic potential by the different EDL structures, the state of charge (SOC), and the diffusivity are also investigated through a comprehensive parameter study. A few conclusions can be drawn, e.g., the total electrostatic potential drop is only related to the free enthalpy difference of materials, even

with the different electrical double layer structures. Furthermore, the charge transfer resistance with the diffuse double layer structure is higher than that with the compact double layer.

Besides the interface equilibrium, the thesis also delivers a comprehensive ASSBs interface impedance study based on the proposed electrochemical model. One important new aspect is thereby the consideration of the activation energy of materials in the reaction kinetics. It allows the subsequent results for both electrolytes and battery half-cells, such as new equivalent circuit models and extended analytical results directly linked to material properties. Owing to the advantages of the proposed modified Planck-Nernst-Poisson (MPNP) model, the space charge layer impedance investigation has been carried out here. Compared to the conventional model, we provide a new analytical solution for the space charge layer capacitance because of the vacancy effect. Moreover, due to the charge accumulation or depletion in the space charge layer, a constant resistance has been considered in some equivalent circuit models. Nevertheless, the charge density in the space charge layer region should be frequency-dependent with the perturbation potential. Consequently, a new space charge layer resistance is introduced in the corresponding equivalent circuit model. Results indicate that our new model can explain well the experimentally observed impedance tail at the low-frequency region. Additionally, the quantifications of the circuit elements are presented based on material properties.

Thereafter, the proposed model has been employed to investigate ASSBs impedance with consideration of the reaction kinetics determined by the free enthalpy difference. Additionally, we derive from the electrochemical model a comprehensive equivalent circuit model with all elements are quantified from material properties. Results show that the high-frequency semicircle in the impedance spectroscopy attributes to the bulk impedance and is associated with ion migration. Moreover, the plots at low and medium frequencies are assigned to the charge transfer resistance and the space charge layer capacitance. Moreover, batteries with a higher free enthalpy difference lead to a significant decrease of the charge transfer resistance, but, increase the total electrostatic potential drop across the interface.

This thesis provides not only an advanced electrochemical model for ASSBs, but also an in-depth understanding of the space charge layer and the interface impedances. The knowledge obtained is general and can be applied for high-performance batteries investigation.

List of Symbols and Units

c_i	Concentration	mol m^{-3}
c_{max}	Maximum concentration	mol m^{-3}
ρ	Immobile concentration	mol m^{-3}
D_i	Diffusion coefficient	$\text{m}^2 \text{s}^{-1}$
Φ_i	Electrostatic potential	V
E_i	Electric field	V m^{-1}
μ_i^*	Chemical potential	J mol^{-1}
μ_i^\ominus	Standard chemical potential	J mol^{-1}
μ_i	Electrochemical potential	J mol^{-1}
G_i	Gibbs free enthalpy	eV
G_i^\ominus	Standard Gibbs free enthalpy	eV
ΔG_i	Activation energy	eV
ΔG_i^\ominus	Standard activation energy	eV
ΔG	Free enthalpy difference	eV
J_i	Concentration flux	$\text{mol m}^{-2} \text{s}^{-1}$
σ_i	Conductivity	$\Omega^{-1} \text{m}^{-1}$
$R_{i,ct}$	Charge transfer resistance	Ω
R_i^{bu}	Bulk resistance	Ω
C_i^{bu}	Electrolyte bulk capacitance	F
R_i^{in}	Space charge layer resistance	Ω
C_i^{in}	Space charge layer capacitance	F
C_i^δ	Chemical capacitance	F
I	Total current	A
I_0	Exchange current	A
I_d	Displacement current	A
I_f	Faraday current	A
Z	Total impedance	Ω
Z_{re}	Real impedance	Ω
Z_{im}	Imaginary impedance	Ω

λ_D	Thickness of Debye length	nm
λ_s	Thickness of Stern layer	nm
L_i	Length	nm
t_i	Transference number	-
t	Time	s
R	Gas constant	$\text{J mol}^{-1} \text{K}^{-1}$
T	Temperature	K
F	Faraday constant	C mol^{-1}
z_i	Valence	-
ω	Frequency	Hz
ε_0	Vacuum permittivity	F m^{-1}
ε_i	Relative permittivity	-
k_b	Boltzmann constant	J K^{-1}
N_A	Avogadro constant	mol^{-1}
A	Geometrical surface area	m^2
η	Over potential	V
β	Symmetry factor	-

Contents

List of Symbols and Units	ix
1 Introduction	1
1.1 Basics of Lithium-ion Batteries	1
1.1.1 Cathodes of Lithium-ion Batteries	2
1.1.2 Electrolytes of Lithium-ion Batteries	3
1.2 All-Solid-State Batteries	5
1.2.1 Types of Solid-State Electrolytes in ASSBs	5
1.2.2 Mechanism of Ionic Transport in Solids	6
1.2.3 Challenges in ASSBs	7
1.3 Goal and Outline	8
2 Electrochemical Models of All-Solid-State Batteries	11
2.1 Thermodynamics of Solid Materials	11
2.2 Electrochemical Models for ASSBs	13
2.2.1 Planck-Nernst-Poisson (PNP) Model	14
2.2.2 Pseudo-Two-Dimensional (P2D) model	14
2.2.3 Simple Binary Diffusion (SBD) Model	16
2.3 The Electrical Double Layer Structure	18
2.4 Reaction Kinetics at the Interface	19
2.5 Summary	22
3 Impedance Models of All-Solid-State Batteries	25
3.1 Methodology of Impedance Calculation	26
3.2 Equivalent Circuit Model of Solid-State Electrolytes	27
3.2.1 Ideally Conducting Electrolytes	27
3.2.2 Ideally Blocking Electrolytes	30
3.2.3 Non-ideally Blocking Electrolytes	32
3.3 Equivalent Circuit Models of ASSBs	34
3.4 Impedance Calculation Benchmark	39

3.5	Summary	40
4	Interface Equilibrium of ASSBs	43
4.1	Electrochemical Model	43
4.1.1	Governing Equations	44
4.1.2	The Reaction Kinetics with Vacancies	45
4.1.3	Boundary Conditions	46
4.1.4	Benchmark	47
4.2	Vacancy Effect in ASSBs	47
4.3	Intrinsic Equilibrium State	51
4.4	Influence of Initial Concentrations	53
4.5	Influence of Diffusivity	56
4.6	Summary	57
5	Impedance of Solid-State Electrolytes: Influence of the Contacted Space Charge Layer	59
5.1	Solid-State Electrolytes Impedance Modelling	60
5.1.1	Equivalent Circuit Model	60
5.1.2	Electrochemical Model	62
5.2	Impedance Simulation of Solid-State Electrolytes	63
5.2.1	Analytical Capacitance of the Space Charge Layer	63
5.2.2	Impedance Analysis of Ideally Blocking Solid-State Electrolytes	66
5.2.3	Impedance Analysis of Non-ideally Blocking Solid-State Electrolytes	73
5.2.4	Impedance Analysis of Grain Boundaries in Solid-State Electrolytes	73
5.2.5	Impedance Analysis of Temperature Influence	75
5.3	Experimental Verification	76
5.4	Summary	78
6	Impedance Modelling of ASSBs: Influence of the Kinetic Reaction	79
6.1	Impedance Models for ASSBs	80
6.1.1	Interface Reaction Kinetics	80
6.1.2	Electrochemical Model and Methodology	82
6.1.3	Equivalent Circuit Model and Element Quantification	83
6.2	Results and Discussion	85
6.2.1	EIS Current	86
6.2.2	Charge Transfer Resistance with Dependency on the Free Enthalpy Difference	88
6.2.3	Influence of Standard Activation Energy on the Battery Impedance	90
6.2.4	Influence of Concentration on the Battery Impedance	94
6.2.5	Influence of Diffusivity on the Battery Impedance	97



6.2.6 Influence of Electrical Double Layer on the Battery Impedance 98

6.2.7 Experimental Verification of Charge Transfer Resistance 102

6.3 Concluding Remarks 103

7 Conclusions and Outlook 105

7.1 Conclusion 105

7.2 Outlook 107

Appendix A 109

Appendix B 113

Publication 115

Curriculum Vitae 117

1 Introduction

1.1 Basics of Lithium-ion Batteries

Over the past several decades, the global tendency towards decarbonization has stimulated extensive research on the electric energy storage [1, 2]. Fig. 1.1 illustrates a comparison of the current electric energy storage technologies [2–4] in terms of the energy and power densities. Among these technologies, batteries provide a relatively high conversion efficiency and do not generate gaseous pollutants, are therefore widely studied. In addition, of all available batteries, lithium-ion secondary batteries are considered as the most promising ones because of the high volume and gravimetric energy density [5–13].

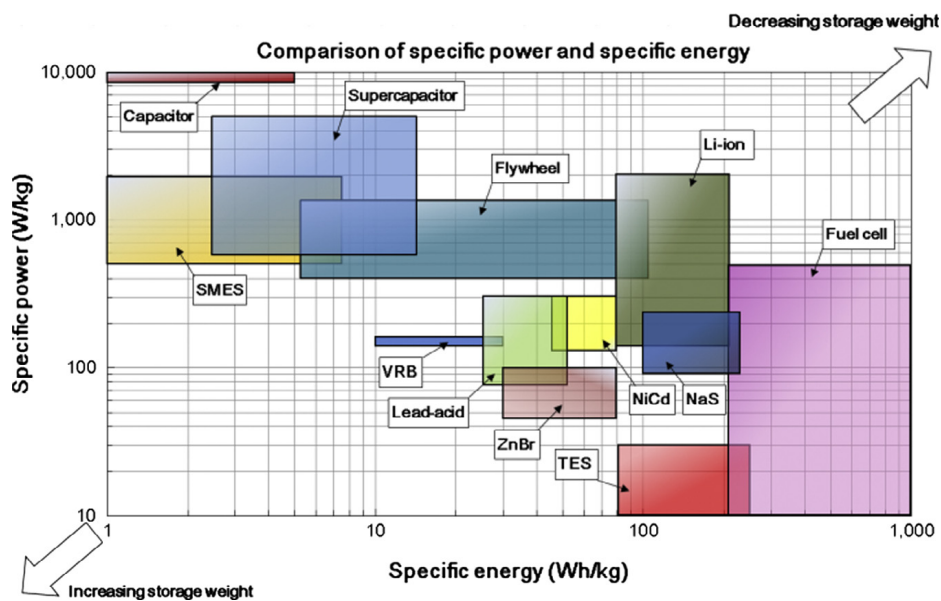


FIGURE 1.1 Comparison of specific energy and specific power [2, 3]. Reproduced with permission from Elsevier.

Lithium-ion battery was first commercialized by Sony corporation in 1991 with a carbon-based anode and $\text{Li}_{1-x}\text{CoO}_2$ as the cathode. After that, intensive developments and technological diversification have taken place with an increasing range of applications. Fig. 1.2 depicts a typical schematic of lithium-ion batteries and the operating mechanism. Battery cell stores the electrical energy as the chemical energy in two electrodes, e.g., a cathode (oxidant) and an anode

(reductant). These two electrodes are separated by an electrolyte which only transfers the ionic component inside the cell. Electrodes consist of a host framework into which the mobile cation can insert reversibly, therefore, lithium-ion transfers forward and backward like a “rocking chair” between two electrodes. During the charging, lithium-ion deintercalates from the cathode and inserts into the anode, and vice versa for the discharging. Because the electrolyte is an electronic insulator, electron flow can only go through an external circuit to maintain the electrical neutrality [14–20].

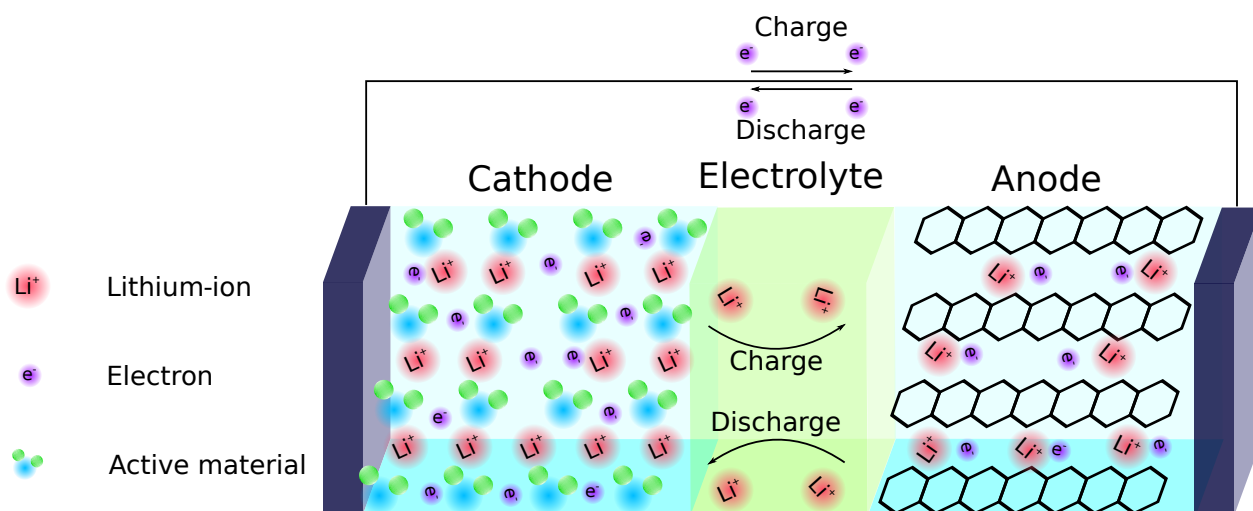


FIGURE 1.2 Schematic of lithium-ion batteries

1.1.1 Cathodes of Lithium-ion Batteries

Since the commercial breakthrough in 1991 based on LiCoO_2 and graphite, researchers have continuously looked for new electrode materials for high-performance batteries over the past decades. The commonly applied cathode materials in lithium-ion batteries are summarized in Tab. 1.1. It can be seen that each material has advantages and disadvantages, which constrains its applicability in lithium-ion batteries [21–23]. Although the layered structure LiCoO_2 cathode has been widely applied in the portable devices, it has the chemical instability at deep charging state and cannot be charged over 50%. Therefore, the spinel LiMn_2O_4 and the olivine LiFePO_4 cathodes have been proposed to partially replace LiCoO_2 . Now, these cathodes have become attractive in electric vehicles because of the good structural and chemical stability, and high charge-discharge rate capability as well. Nevertheless, LiFePO_4 cathode has the poor electronic conductivity in comparison to LiCoO_2 . To maintain the high conductivity, LiFePO_4 particles are synthesized with a small size and coated with conductive carbon, which often increases the processing cost and introduces inconsistencies in performance. As illustrated in Tab. 1.1, the spinel LiMn_2O_4 cathode is unstable by the conventional synthetic method and the $\text{Mn}^{3+/4+}$ is easily oxidized.

In addition to these materials, there are other commercial cathodes based on LiCoO_2 , such as $\text{LiNi}_{0.8}\text{Co}_{0.1}\text{Mn}_{0.1}\text{O}_2$ (NCM811) and $\text{LiNi}_{0.5}\text{Co}_{0.2}\text{Mn}_{0.3}\text{O}_2$ (NCM523). Nevertheless, these cathodes have the severe capacity fade obstacle, especially for NCM811. Concerning the synthesis cost and energy density, the cathode is hard to achieve a revolutionary breakout like LiCoO_2 .

Electrode material	Structure	Cell voltage	Capacity voltage	Advantage	Disadvantage
LiCoO_2 (cathode)	Layered	4 V	140 mAh/g	High electronic and Li^+ ion conductivity; revolutionized the portable electronics market	Expensive and toxic Co; safety concerns; only 50% of the theoretical capacity can be utilized
LiMn_2O_4 (cathode)	Spinel	4 V	120 mAh/g	Inexpensive and environmentally benign Mn; high electronic and Li^+ ion conductivity; excellent rate capability; good safety	Severe capacity fade at elevated temperatures
LiFePO_4 (cathode)	olivine	3.5 V	160 mAh/g	Inexpensive and environmentally benign Fe; covalently bonded PO_4 groups lead to excellent safety	Low electronic and Li^+ ion conductivity; needs small particle size and carbon coating to realize high rate capability; high processing cost

TABLE 1.1 Advantages and disadvantages of the electrode materials [23]. Reproduced with permission from ACS Publications

1.1.2 Electrolytes of Lithium-ion Batteries

Considerable progress has been made for improving the performance of lithium-ion batteries, i.e., the large electrochemical window, the high energy density and the long lifespan, by designing new electrolytes. According to the working mechanism of lithium-ion batteries, there exist several basic requirements for a successful electrolyte [24–27]: (1) High ionic conductivity ($\sigma_+ > 10^{-4} \text{ S cm}^{-1}$) and low electronic conductivity ($\sigma_- < 10^{-10} \text{ S cm}^{-1}$). (2) Chemical stability with respect to electrodes, including the ability to form a passivating solid/electrolyte-interface (SEI) layer. (3) The stable electrode/electrolyte interface during the cycling, i.e., cracks, as well as the interface delamination. (4) High safety, low toxicity, and low cost.

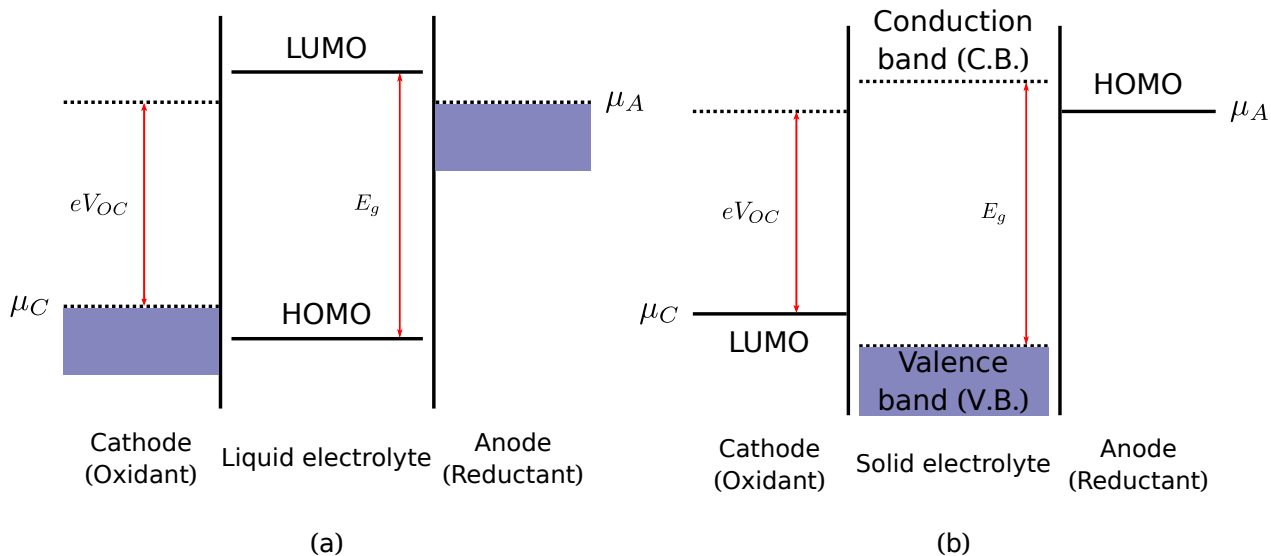


FIGURE 1.3 Energy diagrams of different battery systems with no electrode/electrolyte reaction: (a) liquid electrolytes and (b) solid electrolytes [24, 27, 28].

The most important criterion to identify the chemical stability of batteries is shown in Fig. 1.3. It depicts the energy diagram of a battery cell. The anode (reductant) and the cathode (oxidant) are electronic conductors, and the electrochemical potentials μ_A and μ_C refer to the Fermi energy. The “chemical window” is determined by the energy gap E_g between the lowest unoccupied molecular orbital (LUMO) or conduction band (CB) and the highest occupied molecular orbital (HOMO) or valance band (VB) of the electrolyte material. When μ_A is above LUMO, the electrolyte will be reduced unless a passivating SEI layer forms, thus the anode/electrolyte reaction and electron transfer is blocked. Similarly, if the electrochemical potential μ_C locates below HOMO, a cathode will oxidize the electrolyte until the reaction is blocked by a SEI layer [24–28]. For thermodynamic stability the electrode chemical potentials μ_A and μ_C should be located within the “chemical window” E_g . Therefore, the open-circuit voltage V_{oc} of a battery cell leads to

$$eV_{oc} = \mu_A - \mu_C \leq E_g \quad (1.1)$$

Note that when the electrolyte material has been determined, it is necessary to design electrodes with a high capacity and their μ_A and μ_C matching to the LUMO (CB) and HOMO (VB) of electrolytes.

To fulfil the above requirements, the carbonate organic liquid electrolytes have become dominant in portable consumer devices and electric vehicles. In general, the organic liquid electrolyte penetrates the cell and facilitates a rapid ion transport network between the active cathode and a carbon anode in the commercial lithium-ion battery. Moreover, the applied liquid electrolytes have an oxidation potential (HOMO) around 4.7 V and a reduction potential (LUMO) at 1.0 V.

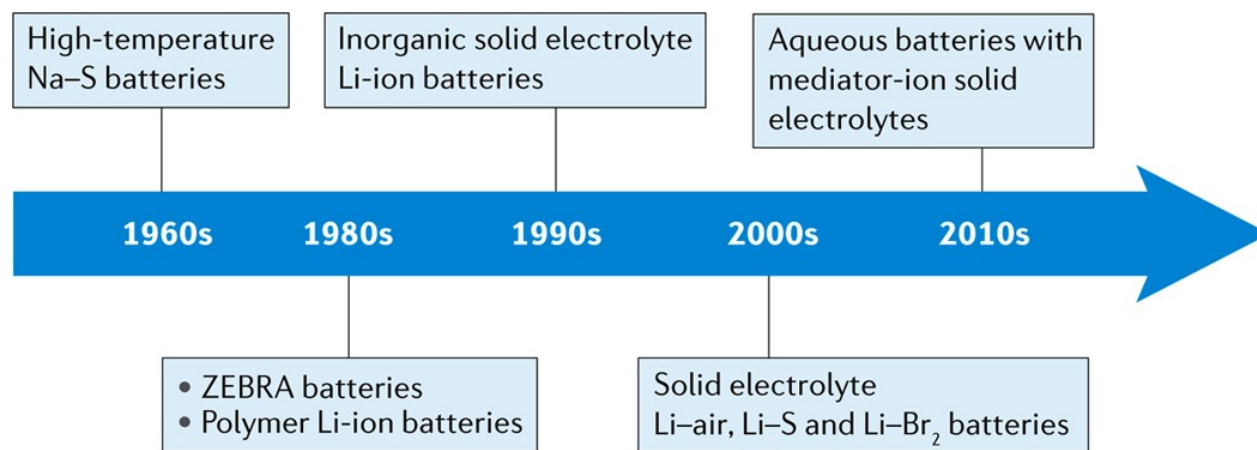
Nevertheless, the carbonate organic electrolytes have a relatively low flash point (30 °C) and can easily cause serious safety issues [24, 29, 30], e.g., thermal runaway, combustion or explosion,

and decomposition of the protective solid electrolyte interphase. Recently, lithium metal has been regarded as the ultimate anodic material because of its ultra-high theoretical specific capacity, i.e., 3860 mAh/g. It is tenfold higher than the currently used graphite anode, i.e., 370 mAh/g. In addition, lithium metal achieves an extremely low standard electrochemical redox potential compared with the standard hydrogen electrode, i.e., -3.04 V. Nevertheless, conventional liquid electrolytes are inadequate for the application in lithium metal batteries because of dendrite formation [31].

To address these issues, replacing liquid electrolytes with solid-state electrolytes has been reviewed as a safe choice (operation temperature: $-50\sim 200$ °C or higher) and is expected to achieve a higher energy density [16, 32–34] and a longer cycle life, e.g., solid-state micro batteries operate for more than 10000 cycles [35]. In addition, changing from liquid to solid-state may also be practical for next generation high energy density batteries [20, 36, 37], such as Li–S (2600 mAh/g) and Li–O₂ (>3500 Wh/kg) batteries [38]. As a result, all-solid-state batteries (ASSBs) have been constructed and extensively studied to overcome the obstacles caused by liquid electrolytes.

1.2 All-Solid-State Batteries

1.2.1 Types of Solid-State Electrolytes in ASSBs



Nature Reviews | [Materials](#)

FIGURE 1.4 A history outline of the development of solid-state electrolytes [33]. Reproduced with permission from Nature.

To date, a large family of solid-state electrolytes has been developed and is clarified in three different types [39–47], i.e., inorganic solid electrolytes, polymer and composite solid electrolytes,

and thin film solid electrolytes. Fig. 1.4 illustrates the development history of solid-state electrolytes. The mainly applied inorganic solid electrolytes include perovskite-type ($\text{Li}_{3x}\text{La}_{2/3-x}\text{TiO}_3$), NASICON-type generally with an $\text{AM}_2(\text{PO}_4)_3$ formula, garnet-type ($\text{A}_3\text{B}_2\text{Si}_3\text{O}_{12}$), in which A and B cations have eightfold and sixfold coordination, and sulfide-type ($\text{Li}_2\text{S}-\text{P}_2\text{S}_5$) materials [48]. The polymer electrolytes can be divided into two classes: dry solid polymer electrolytes and composite polymer electrolytes. Generally, the common polymer hosts are PEO, PAN, PMMA, PVC or PVDF, especially with PEO being the most extensively used [49]. The thin film solid electrolytes are fabricated by special vapour deposition techniques, such as pulsed laser deposition, radio frequency sputtering, as well as chemical vapour deposition [33]. Particularly, the LiPON-based thin film solid electrolyte is regarded as a standard electrolyte for thin film batteries, and this material is utilized to verify our numerical results in the dissertation.

1.2.2 Mechanism of Ionic Transport in Solids

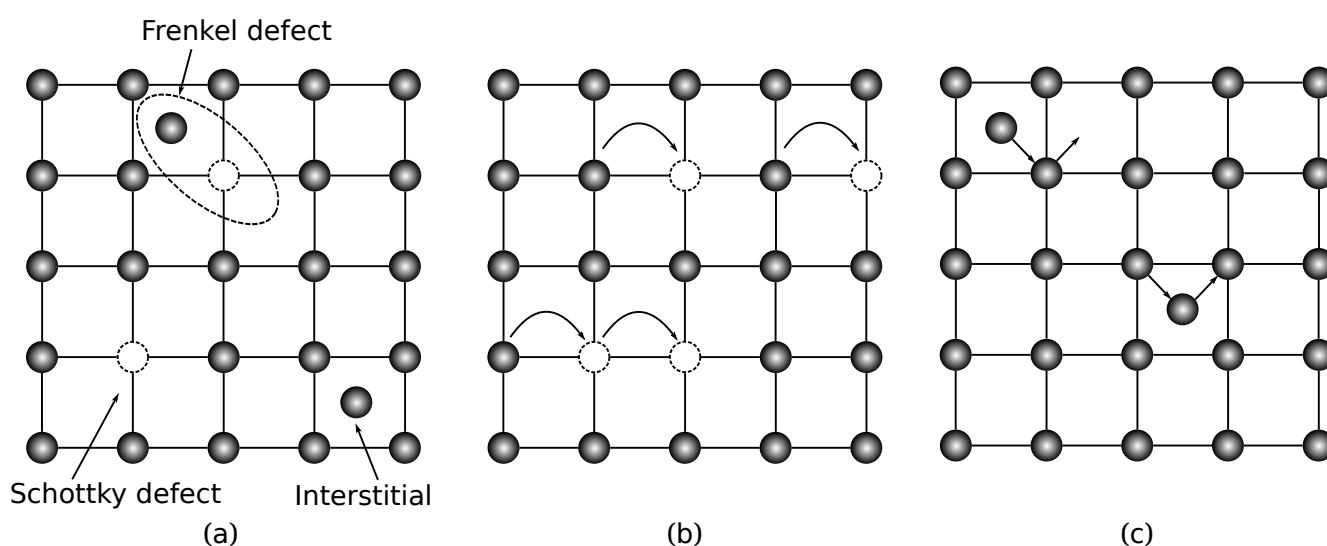


FIGURE 1.5 (a) Defects, (b) the hopping mechanism and (c) the interstitial mechanism of ions in solids.

In this section, we introduce briefly the lithium-ion transport mechanisms in solid materials, because it motivates one of the important novelties of the proposed model in this thesis. Crystalline solids are generally consisting of spatial arrangement of mobile species and coordination polyhedral which constructs the framework of materials. The unoccupied regular lattice sites (vacancies or defects) are randomly distributed in real crystals, thus, the properties of solid electrolytes differ from those of the carbonate organic liquid electrolytes. These defects compose of ionic vacancies in regular crystal lattices, or interstitial atoms or ions which can be intrinsic and stoichiometric, such as Frenkel defects and Schottky defects shown in Fig. 1.5a.

Current understanding of ionic transportation in solids is based on the classical diffusion model [50, 51], which can be achieved by hopping of the mobile ions through the vacancies as presented in Fig. 1.5b, thus it strongly relies on the concentration and distribution of defects in the framework of solids. At the current state, ionic diffusion mechanisms in crystalline solid materials generally consist of the simple vacancy mechanism, the divacancy mechanism, the interstitial mechanism shown in Fig. 1.5c, the interstitial-substitution exchange mechanism, and the collective mechanism [33, 52, 53]. Thereby, to achieve the high ionic conductivity, three criteria have to be fulfilled for materials with this structure [54, 55]. (1) The number of available defects for occupation in solids should be much larger than the mobile ions. (2) The hopping barrier energies for ions from one site to another should be low enough. (3) These defects have to be connected and to form a continuous diffusion pathway.

1.2.3 Challenges in ASSBs

Even though ASSBs show prominent advantages in comparison to batteries with the carbonate organic liquids, three main challenges have been identified recently [20]. ASSBs are expected to suppress the metallic lithium dendrites by virtue of their mechanical rigidity, initially. Nevertheless, investigations have demonstrated that metallic lithium can also penetrate into solids [56]. Thus, much progress has been made in understanding the fundamental mechanism of lithium transport through solid-state electrolytes. The second challenge is the interface stability during the cycling, especially the solid/solid interface. As shown in Fig. 1.3, the formation of a SEI layer or electron-conducting decomposition products have inhibited the performance of ASSBs. The third hurdle lies in the physical contact of active materials in solid-state composite electrodes. Unfortunately, the fundamental understandings of these problems are still underway, which constrain the development of ASSBs. Regarding these challenges, the solid/solid interface is assumed more crucial and is considered as the principal obstacle to developing successful solid-state batteries in comparison to the ionic conductivity [57].

To obtain a deeper understanding of the solid/solid interface, multi-physical models and surface experiments have been extensively applied by researchers. However, it should be noticed that the widely applied electrochemical models for ASSBs batteries are mostly taken from those for liquid electrolytes [58–62]. As illustrated in Fig. 1.5, lithium-ion migration relies on hopping through the vacancies in solids. Therefore, the vacancy effect has to be considered in the electrochemical model, especially in investigating the interface behaviour. The modelling and simulation work in the literature are dominantly devoted to the dynamic processes of batteries, e.g., the cell performance and the crack propagation under cycling. Certain critical issues, such as the interface behaviour at the intrinsic equilibrium state, the exchange current, and the knowledge of interface impedance are still insufficiently investigated for ASSBs.

1.3 Goal and Outline

The goal of this dissertation is to tackle the modelling issues related to solid electrolyte and ASSBs and to deepen the fundamental understanding of the solid/solid interface. The exchange current plays an important role in the reaction kinetics and is extensively applied in the electrochemical models for ASSBs. In addition, the exchange current is associated with material properties at the intrinsic equilibrium state and can be used to estimate the charge transfer resistance. To that end, an advanced modified Plank-Nernst-Poisson (MPNP) coupled with Frumkin-Butler-Volmer (FBV) model for ASSBs is presented in this work. Note that, this advanced model is derived from the fundamental thermodynamics in solids, and with considerations about lithium-ion vacancies and the electrical double layer (EDL) structure. On the basis of this model, the intrinsic equilibrium state of batteries can be well studied and the exchange current is calculated from material properties. In view of the advantage in exploring the interface behaviours, the MPNP-FBV model and the corresponding equivalent circuit model have been applied to calculate the space charge layer impedance including lithium-ion reaction at the interface. In order to demonstrate applicability, this general model is verified from the electrochemical perspective and the interface experiments. In particular, the novelties of this work include the following aspects:

- An advanced modified Plank-Nernst-Poisson (MPNP) coupled with Frumkin-Butler-Volmer (FBV) model is introduced for all-solid-state batteries (ASSBs), which takes the unoccupied regular lattice sites in solids into account.
- The concentration and the electrostatic potential distributions at the intrinsic equilibrium state are well explained. In addition, the correlation between the electrostatic potential drop and material properties is investigated.
- A new analytical space charge layer capacitance based on the MPNP model for ASSBs is proposed and shows more accuracy than the other results.
- A frequency-dependent space charge layer resistance is first introduced in the proposed equivalent circuit model and can well explain the tail in experiments.
- The MPNP-FBV has been applied to calculate the battery impedance with consideration of the reaction kinetics for the first time. Moreover, the interface impedance is quantified by material properties, i.e., the diffusivity and the free enthalpy difference.

The structure of this thesis is organized as followed: In Chap. 2, the fundamental thermodynamics equations and quantities of solids are proposed, e.g., the Gibbs free energy, the chemical potential, and the electrochemical potential. Based on these properties, the prevailing applied models for ASSBs are introduced, i.e., the standard Planck-Nernst-Poisson (PNP) model, the

Pseudo-Two-Dimensional (P2D) model, and the Simple Binary Diffusion (SBD) model. Furthermore, the assumptions, differences, and applicabilities of these models are addressed in detail. Thereafter, the different theories explaining the electrical double layer (EDL) structure and the reaction kinetics at the solid/solid interface are presented.

Here in Chap. 3, we first show the numerical methodology, the electrochemical model and the corresponding equivalent circuit model for the battery impedance calculation. Then, in order to quantify elements in the circuit model and to show the influence of material properties, we take a solid-state electrolyte as an example and discuss different cases, e.g., an ideally conducting electrolyte, an ideally blocking electrolyte, and a non-ideally blocking electrolyte. Due to the reaction kinetics, species accumulate or deplete at the interface and form the space charge layer. Consequently, the charge transfer resistance and the Warburg impedance caused by the concentration disturbance are discussed specifically. Later, a related benchmark test is given to verify the numerical solutions.

An advanced electrochemical (MPNP-FBV) model for ASSBs is proposed in Chap. 4. In comparison with the standard PNP-FBV model, the vacancy effect in solids has been included in this new model and the influence is studied in detail. Thereafter, the intrinsic equilibrium state, the exchange current and the charge transfer resistance are calculated from fundamental material properties. Note that the numerical results are confirmed both chemically and experimentally. Subsequently, different parameters and interface structures are studied to better understand the interface behaviours at the intrinsic equilibrium state.

As a further attempt, the MPNP model is applied to calculate the impedance of solid-state electrolytes in Chap. 5. Here, the space charge layer impedance and the corresponding equivalent circuit model are addressed. Based on the MPNP model, a new analytical solution for the space charge layer capacitance is provided and shows a more accurate and border applicability. Furthermore, a frequency-dependent space charge resistance has been introduced and can explain the experimental impedance tail at the low-frequency region well, for which the pure capacitor interface model fails. To show the applicability, this model is verified against the experimental impedance spectra of LiPON.

In Chap. 6, we employ the MPNP-FBV model and the corresponding equivalent circuit model to calculate the impedance of a half cell that includes lithium-ion reaction at the interface. Based on the free enthalpy difference of materials, the concentration distribution and the bulk electrostatic potential can be identified. Consequently, the analytical solutions of impedances and the correlation of material properties to the battery impedance are revealed. In addition, the impedance spectroscopies with different free enthalpies and interface structures are presented to verify the proposed circuit model. Thereafter, the charge transfer resistance is confirmed by experiments and demonstrates the applicability of the impedance models.

We conclude with a summary of this work and an outlook in Chap. 7.

2 Electrochemical Models of All-Solid-State Batteries

In order to estimate the performance of all-solid-state batteries (ASSBs) and to investigate the species concentration and the electrostatic potential distributions in materials, a set of electrochemical models have been proposed with different physical conditions. Based on applicabilities and simplifications, these extensively applied ASSBs models can be clarified into three types, i.e., the standard Planck-Nernst-Poisson (PNP) model [62], the Pseudo-Two-Dimensional (P2D) model [63, 64], and the Simple Binary Diffusion (SBD) model [59]. As a result, this chapter presents a specific introduction and derivation of the equations applied in these models and highlights the difference between them.

The Gibbs free energy, the chemical and electrochemical potentials are the essential parameters when deriving the electrochemical models, thereby the fundamental thermodynamics of solid materials have been presented in Sec. 2.1. Moreover, the influence of the unoccupied regular lattice sites (vacancies or defects) in solid materials is also addressed in this section. Sec. 2.2 presents the extensively applied electrochemical models for ASSBs and emphasizes the adopting assumption and applicability of these models. The electrical double layer (EDL) structure at the solid/solid interface is introduced in Sec. 2.3. Thereafter, Sec. 2.4 shows the reaction kinetics at the interface based on the energy level concept and presents a specific derivation of the Butler-Volmer (BV) equation.

2.1 Thermodynamics of Solid Materials

In solids, ion diffusion mainly relies on the concentration and distribution of the unoccupied regular lattice sites, e.g., Frenkel defects and Schottky defects, as depicted in Fig. 1.5a. Therefore, the number of defects in solids plays an important role in ionic transportation. According to the reference [65], the total free enthalpy G_{real} of solid materials yields

$$G_{real} = G_{perfect} + \Delta G, \quad (2.1)$$

where $G_{perfect}$ denotes the free enthalpy of perfect solids, and ΔG means the free enthalpy from the non-ideal reaction process. Moreover, ΔG consists of the bonding energy ΔG_{bdg} , the vibration energy ΔG_{vib} , and the configuration component ΔG_{cfg} . Hence, the quantity ΔG is given by

$$\Delta G = \Delta G_{bdg} + \Delta G_{vib} + \Delta G_{cfg}. \quad (2.2)$$

To follow the statistical thermodynamics in materials science, the configuration component free enthalpy ΔG_{cfg} is summarized to [65, 66]

$$k_b \ln \Omega = -\frac{G_{cfg}}{T}. \quad (2.3)$$

Ω denotes the number of microstates, T is the temperature, and k_b is the Boltzmann constant.

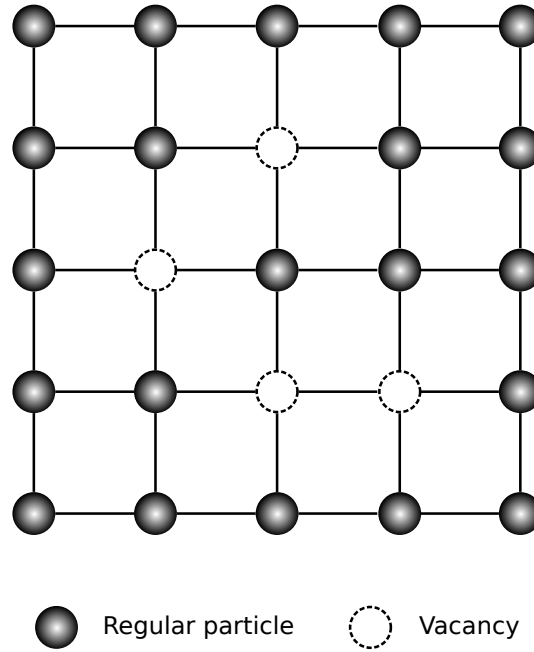


FIGURE 2.1 Schematic of lattice sites in solid materials

Fig. 2.1 shows the schematic of regular lattice sites in solid materials, N represents the total number of regular positions, and N_i means the occupied lattice sites. Thus, N_d denotes the number of unoccupied regular lattice sites (defects or vacancies) and is expressed as $N_d = N - N_i$. For large numbers, the Stirling approximation is applied and is defined as $\ln N = N \ln N - N$. Consequently, $\ln \Omega$ yields

$$\ln \Omega = \ln \frac{N!}{N_i!(N - N_i)!} = (N - N_i) \ln \frac{N}{N - N_i} + N_i \ln \frac{N}{N_i}. \quad (2.4)$$

Based on Eqs. (2.2) to (2.4), the total free enthalpy of real solids leads to

$$G_{real} = G_{perfect} + N_i (\Delta G_{bdg}^* + \Delta G_{vib}^*) - k_b T \ln \Omega. \quad (2.5)$$

ΔG_{bdg}^* and ΔG_{vib}^* are the formation free enthalpies of an occupied site, and the molar chemical potential μ_i^* of solid materials is defined as

$$\mu_i^* = N_A \frac{\partial G_{real}}{\partial N_i} = \mu_i^\ominus + RT \ln \frac{x_i}{1 - x_i}. \quad (2.6)$$

Eq. (2.6) corresponds to a Fermi-Dirac-like distribution, N_A is the Avogadro constant, and R is the gas constant. Moreover, $\mu_i^\ominus = N_A(\Delta G_{bdg}^* + \Delta G_{vib}^*)$ is called the standard chemical potential, and x_i is the dimensionless concentration of regular lattice sites and yields $x_i = N_i/N$.

When the number of defects is relatively small compared to the total regular sites, e.g., ideal solids or dilute solutions ($N_d \ll N$, $N_i \approx N$), the first term of the right-hand side in Eq. (2.4) can be ignored, and $\ln \Omega$ yields

$$\ln \Omega = N_i \ln \frac{N}{N_i}. \quad (2.7)$$

Thereby, the molar chemical potential is simplified as Eq. (2.8) and is the well known Boltzmann form

$$\mu_i^* = \mu_i^\ominus + RT \ln x_i. \quad (2.8)$$

It should be noted that Eq. (2.8) is merely an approximation, and an additive term RT is ignored. Comparing to Eq. (2.6), Eq. (2.8) is more familiar to researchers and has been widely applied in liquid electrolytes modelling [67]. Nevertheless, this formula obtains an obvious drawback and fails to accurately estimate the ionic migration in solid materials, particularly in the case where the vacancy effect cannot be ignored. The difference between these two equations and the vacancy effect will be shown in Chap. 4.

2.2 Electrochemical Models for ASSBs

The Gibbs free energy G_{real} and the chemical potential μ_i^* of solid materials are proposed in Sec. 2.1. Thereby, the extensively applied electrochemical models for ASSBs will be introduced in this section based on these material properties. In the electrochemical system, the electrostatic potential Φ has to be included and the electrochemical potential μ_i is defined as

$$\mu_i = \mu_i^* + z_i F \Phi, \quad (2.9)$$

where F is the Faraday constant, z_i is the valence of species. Under these circumstances, the species flux J_i is derived from the electrochemical potential μ_i [68] and is given by

$$J_i = -\frac{D_i}{RT} c_i \nabla \mu_i, \quad (2.10)$$

where D_i is the diffusivity of species and c_i is the species concentration. Thus, a material balance leads to the differential conservation law

$$\frac{\partial c_i}{\partial t} = -\nabla \cdot J_i. \quad (2.11)$$

Eqs. (2.9) to (2.11) are the fundamental equations of the electrochemistry, and three different models for ASSBs are derived based on these formulas.

2.2.1 Planck-Nernst-Poisson (PNP) Model

The standard Planck-Nernst-Poisson (PNP) model is composed of the Planck-Nernst equation and the Poisson equation, and is extensively applied in liquid electrolytes. Recently, the standard PNP model is also utilized to investigate ASSBs [62], particularly in the study of interface behaviours. The chemical potential in the standard PNP model is expressed by Eq. (2.8), thus the electrochemical potential and the flux are

$$\mu_i = \mu_i^\ominus + RT \ln x_i + z_i F \Phi, \quad (2.12)$$

$$J_i = -D_i \nabla c_i - z_i \frac{F D_i}{RT} c_i \nabla \Phi, \quad (2.13)$$

and a material balance for the component yields

$$\frac{\partial c_i}{\partial t} = D_i \nabla^2 c_i + z_i \frac{F D_i}{RT} \nabla \cdot (c_i \nabla \Phi). \quad (2.14)$$

Eq. (2.14) is the well known Planck-Nernst equation and becomes ubiquitous in battery modelling. It should be noted that the vacancy effect shown in Fig. 2.1 is overlooked in the Planck-Nernst equation.

The relationship between the electric charge density and the electrostatic potential is depicted by the Poisson equation and is given by

$$\nabla^2 \Phi = -\frac{F}{\varepsilon_i \varepsilon_0} \sum_i z_i c_i. \quad (2.15)$$

ε_0 and ε_i represent the vacuum and the relative dielectric permittivities of materials, respectively. Hence, the combination of Eqs. (2.14) and (2.15) are called the standard Planck-Nernst-Poisson (PNP) model. It can be observed that no other assumptions have been applied in this model except that the vacancies in solids are ignored. Consequently, the standard PNP model has been extensively applied in modelling low-concentration solid-state batteries or liquid electrolytes. Nevertheless, species will accumulate at the solid/solid interface and form the space charge layer due to the reaction kinetics. Under this circumstance, the vacancy effect cannot be overlooked any more. Therefore, the standard PNP model fails to be applied in high-concentration electrolytes or the space charge layer region.

2.2.2 Pseudo-Two-Dimensional (P2D) model

In addition to the standard PNP model, the Pseudo-Two-Dimensional (P2D) model [63, 64] is also widely applied for ASSBs when modelling the cell performance. The P2D model was originally

introduced by Doyle and Newman [69] to study conventional batteries, and is regarded as the most classical electrochemical model. It should be noted that the basic equations applied in the P2D model are the same as the standard PNP model, while a few additional hypotheses and transformations are adopted.

In lithium-ion batteries, the faradaic current density I_f in materials is associated with the species flux and is given by

$$I_f = F \sum_i z_i J_i. \quad (2.16)$$

Here, J_i follows Eq. (2.13), and Eq. (2.16) can be written as

$$I_f = -F \sum_i z_i D_i \nabla c_i - \frac{F^2}{RT} \sum_i D_i z_i^2 c_i \nabla \Phi. \quad (2.17)$$

When there is no concentration gradient in materials, i.e., $\nabla c_i = 0$, the term $-F \sum_i z_i D_i \nabla c_i$ can be eliminated and Eq. (2.17) is reduced to this form

$$I_f = -\sigma \nabla \Phi. \quad (2.18)$$

Where σ is called the conductivity and is defined as

$$\sigma = \frac{F^2}{RT} \sum_i D_i z_i^2 c_i. \quad (2.19)$$

Eq. (2.18) is a common expression of the Ohm's law and is also extensively applied in battery modelling. Nevertheless, we have to notice that Eq. (2.18) is valid only for materials in the absence of the concentration gradient. Under this circumstance, the current density $I_{f,+}$ caused by lithium-ions leads to

$$I_{f,+} = -\frac{F^2}{RT} D_+ z_+^2 c_+ \nabla \Phi. \quad (2.20)$$

Moreover, the fraction of the current density carried by species i is known as the transference number t_i , and lithium-ion transference number t_+ is given by

$$t_+ = \frac{I_{f,+}}{I_f} = \frac{D_+ z_+^2 c_+}{\sum_i D_i z_i^2 c_i}. \quad (2.21)$$

Thus, Eq. (2.20) can be written as

$$-\frac{F D_+}{RT} z_+ c_+ \nabla \Phi = \frac{t_+}{z_+ F} I_f, \quad (2.22)$$

and is applied with an underlying assumption that no concentration gradient exists within electrolytes.

With consideration of the concentration gradient, i.e., $\nabla c_i \neq 0$, the current density is not proportional to the electric field. Thereby, we substitute Eq. (2.22) into Eq. (2.13) and can derive the following equation

$$J_+ = -D_+ \nabla c_+ + \frac{t_+}{z_+ F} I_f, \quad (2.23)$$

and the mass conservation equation reduces to

$$\frac{\partial c_+}{\partial t} = D_+ \nabla^2 c_+ - \frac{\nabla \cdot t_+}{z_+ F} I_f. \quad (2.24)$$

Furthermore, the Ohm's law can be extended to Eq. (2.25) when the concentration gradient is included

$$I_f = -F \sum_i z_i D_i \nabla c_i - \sigma \nabla \Phi. \quad (2.25)$$

Thus, the electrostatic potential gradient yields

$$\nabla \Phi = -\frac{F}{\sigma} \sum_i z_i D_i \nabla c_i - \frac{I_f}{\sigma}. \quad (2.26)$$

Alternatively, Eq. (2.26) can also be written as

$$\nabla \Phi = -\frac{RT}{F} \sum_i \frac{t_i}{z_i} \nabla \ln c_i - \frac{I_f}{\sigma}. \quad (2.27)$$

Here, Eqs. (2.24) and (2.27) are the two fundamental equations within the P2D model. In comparison to the standard PNP model, the electrostatic potential Φ in the P2D model is associated with the charge/discharge current I_f , the conductivity σ , and the transference number t_i . Moreover, these parameters can be easily obtained from experimental results and other empirical formulae. Because of the advantage, the P2D model is widely applied in ASSBs modelling, especially in cases with the galvanostatic condition.

Even though the P2D model is popular, the underlying assumptions and the applicability are still need to be identified. It can be observed that the transference number t_i is a critical parameter in the P2D model and is associated with material properties. Nevertheless, this parameter is always given by the empirical formula in practical. Consequently, the P2D model fails to precisely estimate the concentration and the electrostatic potential distributions at the micro-scale. Furthermore, the material conductivity σ applied in Eq. (2.19) is calculated with the constant concentration assumption, i.e., $\nabla c_i = 0$. In the zone of the space charge layer, the concentration of lithium-ions changes rapidly and the conductivity can no longer be constant. Hence, we can conclude that the P2D model is not suitable to focus on the interface behaviours, especially in considering the space charge layer.

2.2.3 Simple Binary Diffusion (SBD) Model

The generally applied standard PNP model and the P2D model have been presented in the previous sections. However, the two models are complex and can only be solved with numerical methods. In order to extend the applicability of the electrochemical models, a simple binary diffusion (SBD) model for ASSBs was introduced by Danilov and Notten [59]. This model is applied with a

symmetric electrolyte assumption, which means the number of cations equals to the anions. Thus, the species concentration and the valence lead to

$$c = c_+ = c_- \quad z = z_+ = |z_-|. \quad (2.28)$$

The material balances of the species are given by

$$\frac{\partial c_+}{\partial t} = D_+ \nabla^2 c_+ + z_+ \frac{FD_+}{RT} \nabla \cdot (c_+ \nabla \Phi), \quad (2.29)$$

$$\frac{\partial c_-}{\partial t} = D_- \nabla^2 c_- + z_- \frac{FD_-}{RT} \nabla \cdot (c_- \nabla \Phi). \quad (2.30)$$

Subtraction gives

$$(D_+ - D_-) \nabla^2 c + (z_+ D_+ - z_- D_-) \frac{F}{RT} \nabla \cdot (c \nabla \Phi) = 0. \quad (2.31)$$

The term $\nabla \cdot (c \nabla \Phi)$ can be solved from Eq. (2.31), which reduces to

$$\nabla \cdot (c \nabla \Phi) = -\frac{RT(D_+ - D_-)}{F(z_+ D_+ - z_- D_-)} \nabla^2 c. \quad (2.32)$$

Thereby, the mass balance equation reduces to

$$\frac{\partial c}{\partial t} = \frac{z_+ D_+ D_- - z_- D_- D_+}{z_+ D_+ - z_- D_-} \nabla^2 c. \quad (2.33)$$

Eq. (2.33) is a common concept of the Fick's law, and the corresponding analytical solutions have been extensively studied. We take a further step and integrate Eq. (2.33), thus it yields

$$\int_0^{L_e} c \nabla \Phi = -\frac{RT(D_+ - D_-)}{F(z_+ D_+ - z_- D_-)} \int_0^{L_e} \nabla c. \quad (2.34)$$

The electrostatic potential Φ and the electric field $\nabla \Phi$ can be resolved analytically with appropriate boundary conditions. Eqs. (2.33) and (2.34) are the basic equations of the simple binary diffusion (SBD) model. As shown in the references [59, 61], the numerical results fit quite well with the experimental data, thus indicates the applicability of this model. Nevertheless, the SBD model has to fulfil the symmetric electrolyte assumption, i.e., $c_+ = c_-$ and $z_+ = -z_-$. Under this circumstance, the electrostatic potential gradient term can be replaced by Eq. (2.32), and the mass balance equation reduces to the simple Fick's law. Electrical neutrality is satisfied in the bulk of electrochemical systems except in the interface and surface regions, thereby this model also fails to study the space charge layer. It can be seen that the symmetric electrolyte assumption is stricter than that adopted in the P2D model, thus limiting the applicability of the SBD model.

2.3 The Electrical Double Layer Structure

The electrical double layer (EDL) theory is extensively used to study the solid/liquid interface behaviours, due to water molecules accumulation. Experimental observations [70] show that the concentration distribution in ASSBs is similar to the solid/solution interface. Thereby, the electrical double layer model has been employed to explain the solid/solid interface behaviours in this work.

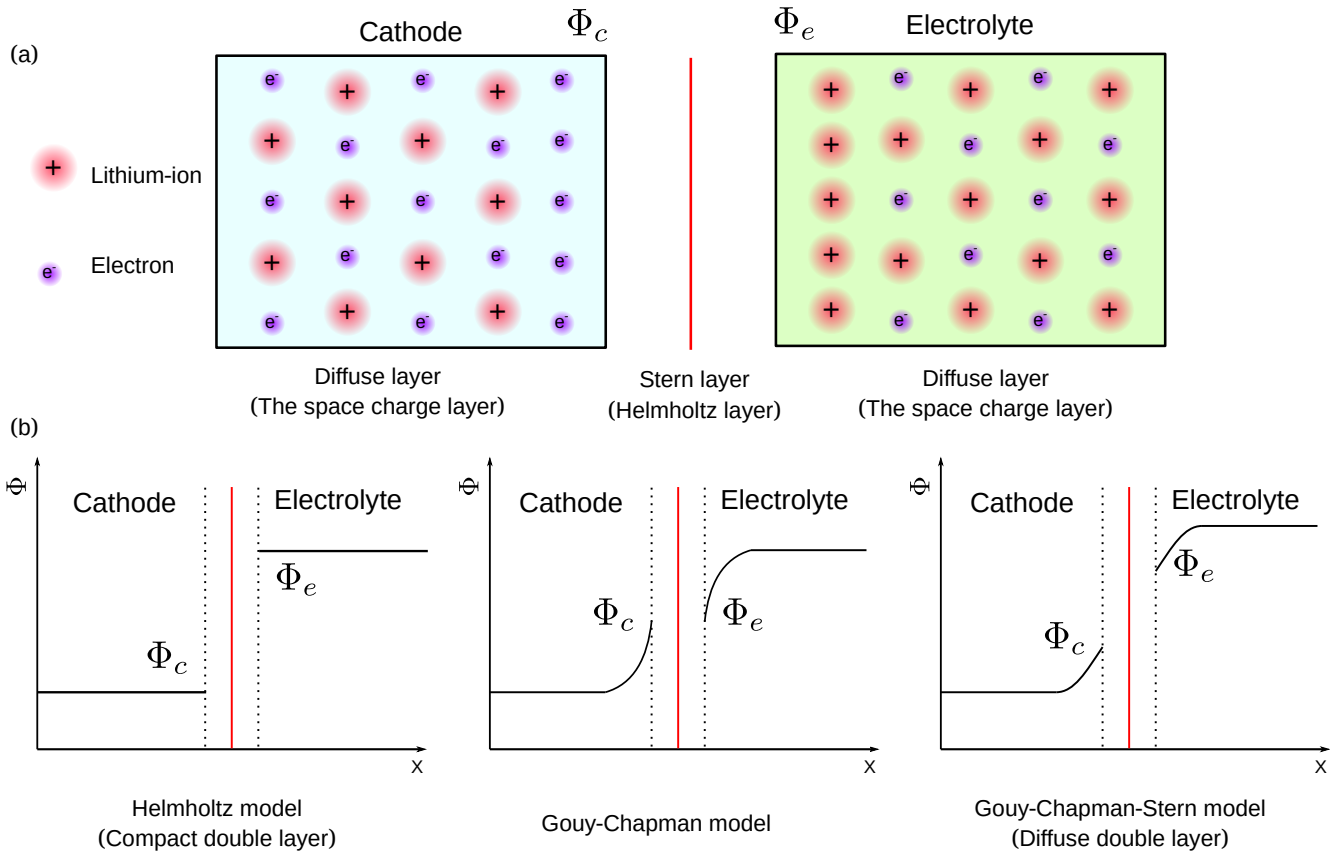


FIGURE 2.2 (a) The schematic of a cathode/solid-state electrolyte interface (b) the different electrical double layer (EDL) structures.

Fig. 2.2a sketches the solid/solid interface, which shows that positive excess charges accumulate in one phase and negative excess charges on the other side. As shown here, the electrical double layer is represented by the Stern layer (Helmholtz layer) and the diffuse layer. Note that the diffuse layer of excess charges in solids is also called the space charge layer [71]. Moreover, the overlapping plane between the Stern layer and the diffuse layer is the Helmholtz plane. For a description of the charges concentration and the electrostatic potential distribution through the EDL, there exist three different models as presented in Fig. 2.2b.

In the Helmholtz-layer model (the compact double layer model), the electrostatic potential Φ

merely drops in the Stern layer. This model is incomplete because it ignores the thermal motion of the charge species in the space charge layer. Another theory is the Gouy-Chapman model and assumes that the total electrostatic potential decreases only in the space charge layer. Hence, these models are two extreme cases for the EDL structure. By comparison, in the Gouy-Chapman-Stern model (the diffuse double layer model) [68], the electrostatic potential drops simultaneously in these two layers. In view of the advantage, the diffuse double layer model has been widely applied in the interface modelling with considering the double layer effect. The Stern layer is regarded as a pure capacitor in investigations, therefore, the electrostatic potential has to drop linearly in this region. Thereby, the electrostatic potential drop at the interface of these different models are shown below:

1) Helmholtz model

$$\nabla\Phi_c = \nabla\Phi_e = 0 \quad (2.35)$$

2) Gouy-Chapman model

$$\Phi_c = \Phi_e \quad (2.36)$$

3) Gouy-Chapman-Stern model

$$\Phi_c = \Phi_e - \vec{n} \cdot \lambda_s \nabla\Phi_c \quad (2.37)$$

Thereby, Φ_c and Φ_e are the electrostatic potentials at the Helmholtz plane in the cathode and the electrolyte, as shown in Fig. 2.2. Without the specific notation, the subscript “c” and “e” indicate the cathode and the electrolyte in this study, respectively. The thickness of the Stern layer is constant and independent of the nature of solids, i.e., $\lambda_s = H/2 = 0.3 \sim 0.5$ nm, where H is the diameter of lithium-ions [68, 71]. The thickness of the space charge layer is denoted by L_s and is of the order of 1 to 10 nm [72].

2.4 Reaction Kinetics at the Interface

In order to study the reaction kinetics at the interface, we consider a half cell which is composed of a cathode and a solid-state electrolyte at the intrinsic equilibrium state without any extrinsic perturbation, as depicted in Fig. 2.3a. Fig. 2.3b sketches the free enthalpy profile of lithium-ion reaction at the cathode/electrolyte interface. ΔG_i is the actual activation energy and G_i represents the free enthalpy of materials. Both of them are determined by the standard states and the concentration. Because of the free enthalpy difference between the cathode and the electrolyte, i.e., $\Delta G = G_c - G_e$, lithium-ion transfer occurs after these two materials come into contact, establishing the intrinsic electrochemical equilibrium and the exchange current.

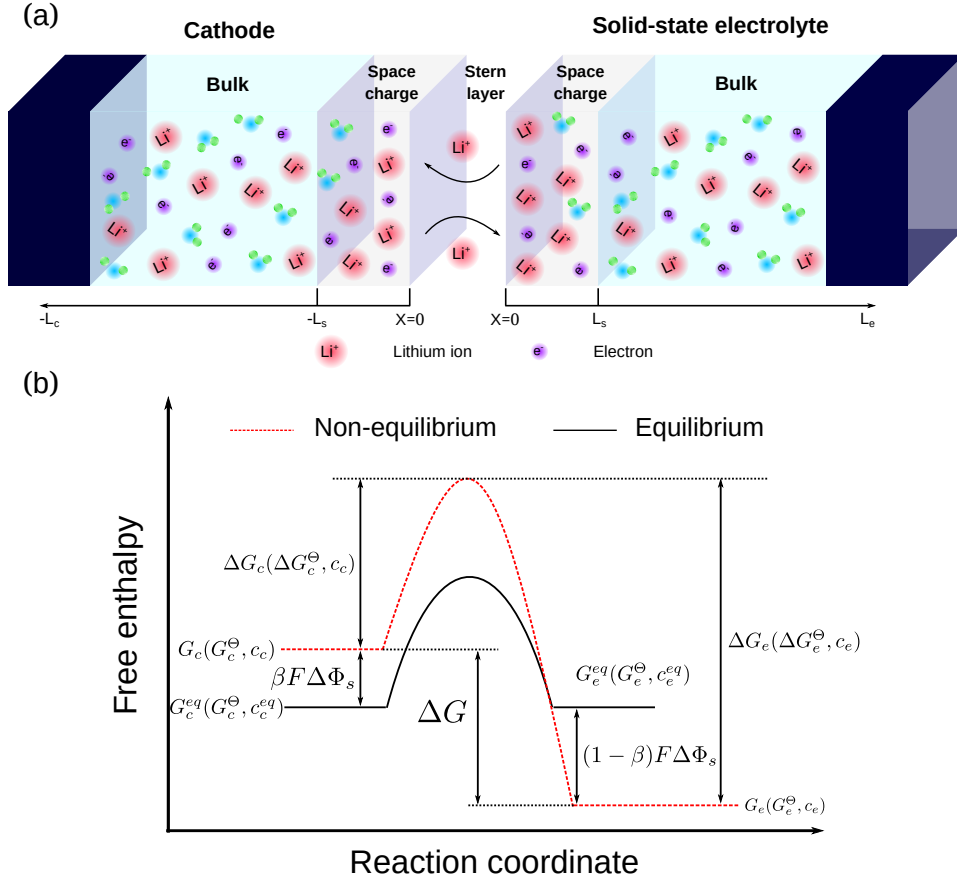


FIGURE 2.3 (a) Schematic of the electrical double layer (EDL) structure and (b) the charge transfer reaction at the cathode/electrolyte interface.

In lithium-ion battery modelling, the basic electrochemical reaction at the interface is represented by



where $\text{Li}_{(c)}$ represents intercalated lithium in the cathode and $\text{Li}_{(e)}^+$ denotes lithium-ions in the solid-state electrolyte, respectively. The charge transfer reaction at the interface is described by the Butler-Volmer (BV) equation [73] and the initial fluxes are given by Eq. (2.39),

$$\begin{aligned} J_c &= K_o \exp\left(-\frac{F\Delta G_c^\ominus}{RT}\right) c_c, \\ J_e &= K_r \exp\left(-\frac{F\Delta G_e^\ominus}{RT}\right) c_e. \end{aligned} \quad (2.39)$$

Thereby, c_i are the concentrations, β is called the symmetry factor and usually $\beta = 0.5$, K_o and K_r are the reaction rate coefficients depending on the temperature. ΔG_c^\ominus and ΔG_e^\ominus are the standard activation energies of materials, as shown in Fig. 2.3b.

Due to lithium-ion reaction at the interface, the concentrations change and an electrostatic potential gradient is built up as shown in Fig. 2.2b. Consequently, the electrostatic potential factor

has to be included in Eq. (2.39) during the reaction. The partial currents are expressed as

$$\begin{aligned} J_c &= K_o \exp\left(-\frac{F\Delta G_c^\ominus}{RT}\right) \exp\left[\frac{\beta F\Delta\Phi_s}{RT}\right] c_c, \\ J_e &= K_r \exp\left(-\frac{F\Delta G_e^\ominus}{RT}\right) \exp\left[-\frac{(1-\beta)F\Delta\Phi_s}{RT}\right] c_e, \end{aligned} \quad (2.40)$$

where $\Delta\Phi_s = \Phi_c - \Phi_e$ is the electrostatic potential drop across the Stern layer, which is shown in Fig. 2.2b. Eq. (2.40) is called the Frumkin-Butler-Volmer (FBV) equation, and the driving force of lithium-ion reaction is the electrostatic potential drop $\Delta\Phi_s$. As shown in the FBV equation, the electrostatic potential drop across the Stern layer $\Delta\Phi_s$ and the space charge layer (or called the diffuse layer) are taken into account separately [74].

The overall flux of lithium-ions is the difference between reduction and oxidation fluxes, and yields

$$J = K_o \exp\left(-\frac{F\Delta G_c^\ominus}{RT}\right) \exp\left[\frac{\beta F\Delta\Phi_s}{RT}\right] c_c - K_r \exp\left(-\frac{F\Delta G_e^\ominus}{RT}\right) \exp\left[-\frac{(1-\beta)F\Delta\Phi_s}{RT}\right] c_e. \quad (2.41)$$

By the change of $\Delta\Phi_s$ and c_i , the two partial fluxes will be numerically equal, i.e., $J_c = J_e$, and the system reaches the intrinsic equilibrium state. It is important to recognize that the intrinsic equilibrium state corresponds to a dynamic equilibrium and not to zero activity. Under this circumstance, the current at the intrinsic equilibrium state is called the exchange current and is expressed as $I_0 = FAJ_0 = FAJ_c = FAJ_e$. Where A is the cross section area and J_0 represents the magnitude of the partial flux. When the net flux equals zero, the equilibrium electrostatic potential difference and the flux are given as

$$\Delta\Phi_s^{eq} = \frac{RT}{F} \ln \frac{K_r}{K_o} + \frac{RT}{F} \ln \frac{c_e^{eq}}{c_c^{eq}} + \Delta G_c^\ominus - \Delta G_e^\ominus, \quad (2.42)$$

$$J_0 = \left[K_o \exp\left(-\frac{F\Delta G_c^\ominus}{RT}\right) \right]^{1-\beta} \left[K_r \exp\left(-\frac{F\Delta G_e^\ominus}{RT}\right) \right]^\beta (c_c^{eq})^{1-\beta} (c_e^{eq})^\beta. \quad (2.43)$$

The superscript “eq” denotes the intrinsic equilibrium state. When the external perturbation is applied, the electrostatic potential difference can be written as

$$\Delta\Phi_s = \Delta\Phi_s^{eq} + \eta, \quad (2.44)$$

where η is the overpotential. With the external perturbation, the actual reaction fluxes are given by

$$\begin{aligned} J_c &= K_o \exp\left(-\frac{F\Delta G_c^\ominus}{RT}\right) \exp\left[\frac{\beta F(\Delta\Phi_s^{eq} + \eta)}{RT}\right] c_c, \\ J_e &= K_r \exp\left(-\frac{F\Delta G_e^\ominus}{RT}\right) \exp\left[-\frac{(1-\beta)F(\Delta\Phi_s^{eq} + \eta)}{RT}\right] c_e. \end{aligned} \quad (2.45)$$

Combining with Eq. (2.43), the nett flux yields

$$J = J_0 \left\{ \frac{c_c}{c_c^{eq}} \exp \left[\frac{\beta F \eta}{RT} \right] - \frac{c_e}{c_e^{eq}} \exp \left[-\frac{(1-\beta) F \eta}{RT} \right] \right\}. \quad (2.46)$$

With the assumption $c_c/c_c^{eq} \approx 1$ and $c_e/c_e^{eq} \approx 1$, Eq. (2.46) can be simplified to a more familiar Butler-Volmer (BV) equation

$$I = I_0 \left\{ \exp \left[\frac{\beta F \eta}{RT} \right] - \exp \left[-\frac{(1-\beta) F \eta}{RT} \right] \right\}. \quad (2.47)$$

Eq.(2.47) is the fundamental equation in battery modelling, especially in the assessment of cell performance. It can be noted that the exchange current I_0 is a critical parameter that determines the reaction rate. Nevertheless, the exchange current is related to material properties and the intrinsic equilibrium state, and is hard to quantify. Consequently, a specific discussion of the exchange current calculation will be presented in the following chapters.

2.5 Summary

In this chapter, we start from the basic thermo-dynamics and then derive a series of fundamental equations for solid materials. The Gibbs free energy, the microstates, and the chemical potentials with and without vacancies of materials have been proposed in Sec. 2.1.

Based on the fundamental properties, three different electrochemical models for ASSBs have been introduced in Sec. 2.2. In comparison to the other two models, no hypothesis is adopted in the standard Planck-Nernst-Poisson (PNP) model and the equations are directly derived from thermodynamics. Subsequently, the widely applied Pseudo-Two-Dimensional (P2D) model and the underlying assumption are shown here. The P2D model is associated with the current and demonstrates obvious advantages in estimating the cell performance. Compared to the previous the PNP and P2D models, the simple binary diffusion (SBD) model is quite simple and can be solved analytically with the appropriate boundary conditions. It should be noted that the assumptions, e.g., the constant concentration and the electrical neutrality, limited the applicability of the P2D and SBD models, especially in the study of interface behaviours.

Sec. 2.3 presents the electrostatic potential distributions with the different electrical double layer (EDL) structures. There exists three different models, i.e., the Helmholtz model, the Gouy-Chapman model, and the Gouy-Chapman-Stern model. Owing to the advantage, the Gouy-Chapman-Stern model has been employed to study the solid/solid interface in our work. Thereafter, the reaction kinetics based on energy level concepts is shown in Sec. 2.4. To correlate the reaction kinetics with the EDL structure, the Frumkin-Butler-Volmer (FBV) equation is adopted. Therefore, the electrostatic potential drop at the interface can be split into two parts, i.e., the

Stern layer and the space charge layer. In addition, the exchange current I_0 , the overpotential η , and the more widely applied Butler-Volmer (BV) equation are also introduced in detail.

Note that the chemical potential in these electrochemical models is defined as $\tilde{\mu}_i = \mu_i^\ominus + RT \ln x_i$, and the vacancy effect in solids is not included. Therefore, a physical electrochemical model for ASSBs to investigate the interface behaviours is still indispensable. To tackle this obstacle, an advanced electrochemical model has been proposed in this work, and the chemical potential is given by $\tilde{\mu}_i = \mu_i^\ominus + RT \ln(x_i/1 - x_i)$ based on the conclusion in Sec. 2.1. More details about the model will be given in following chapters.

3 Impedance Models of All-Solid-State Batteries

Solid-state electrolytes have a relatively high interface impedance which is the bottleneck for the development of high-performance ASSBs in comparison to liquid electrolytes [48, 75–81]. Charges accumulate in the space charge layer and lead to a drastic electrostatic potential drop, thus the solution to battery design hinges the fundamental knowledge of the interface impedance. Consequently, research efforts have been focused on utilizing theoretical and numerical tools to clarify the microscopic origin of impedance. Electrochemical impedance spectroscopy (EIS) is an established technique for characterizing and measuring the battery impedance [82–87]. Nevertheless, the impedance spectroscopy is hard to analyse, e.g., the complex plane and the frequency signal, and is difficult to distinguish the contribution of each part. Therefore, the equivalent circuit model is proposed to assist in interpreting the impedance spectroscopy. By adjusting the experimental data, elements of the electrical circuit model can be quantified [88], and provide insight into impedance contributions.

The current state-of-the-art impedance modelling and simulation can be roughly classified into three categories, i.e., the electrochemical model [89], the equivalent circuit model [90, 91], and the density functional theory (DFT) calculation [92]. The DFT calculation shows an obvious advantage when explaining the interface impedance from material properties, e.g., the atomic structure [75] and the activation energy. Unfortunately, this method cannot calculate the interface impedance directly and fails to estimate the overall impedance of a battery as well. In comparison to the DFT calculation, the electrochemical model and the corresponding equivalent circuit model obtain the advantage in calculating the battery impedance and are widely applied. Both models and the method for calculating impedance are therefore presented in this chapter.

Electrochemical models are derived from the basic thermodynamics, e.g., the electrochemical potential, and the numerical results of such models provide spatial and temporal distributions of the concentration and electrostatic potential [93–95]. In comparison to the electrochemical model, the equivalent circuit model is more simple and is able to quantify the impedance of each part. To address these models, Sec. 3.1 provides an introduction to the methodology for calculating the battery impedance. The corresponding equivalent circuit models for solid-state electrolytes

are presented in Sec. 3.2 and provide theoretical quantification of the circuit components. The derivations of the charge transfer resistance and the Warburg impedance are shown in Sec. 3.3. Later, Sec. 3.4 and 3.5 present a benchmark test and a short conclusion are presented.

3.1 Methodology of Impedance Calculation

In electrochemical impedance spectroscopy (EIS) measurement, the widely adopted method is the application of a small perturbation potential or current to an electrochemical system and measuring the corresponding response. The response is the ratio of the perturbation potential to the current and is described as an impedance Z [96–99]. In this work, batteries operate with a pulse electric potential condition and the formula is given by

$$\Phi = \Phi_{dc} + \Phi_{ac}(\cos \omega t + j \sin \omega t). \quad (3.1)$$

Where Φ_{dc} is the potential with a direct current (dc) condition, Φ_{ac} is the alternating current (ac) potential, j is the imaginary number and equals to $\sqrt{-1}$, and ω is the frequency of the applied alternating current potential. According to the previous investigations [96, 97], the corresponding current also has the same type formula and is depicted by

$$I = I_{dc} + I_{ac} [\cos(\omega - \omega_0)t + j \sin(\omega - \omega_0)t]. \quad (3.2)$$

Here, I_{dc} corresponds to the steady-state current and is time independent, I_{ac} is the perturbation current, and ω_0 is the phase angle difference between the imposed electric potential and the measurement current in Eqs. (3.1) and (3.2). Note that the electrochemical impedance Z is defined as [95]

$$Z = \frac{\Phi_{ac}(\cos \omega t + j \sin \omega t)}{I_{ac} [\cos(\omega - \omega_0)t + j \sin(\omega - \omega_0)t]} = Z_{re} + j \cdot Z_{im}, \quad (3.3)$$

where Z_{re} and Z_{im} are the real and imaginary parts of the complex impedance, respectively. The total electrical current I of solid-state electrolytes consists of the faradaic current I_f and the maxwell displacement current I_d , which is expressed by $I = I_f + I_d$. The faradaic current is attributed to the species flux in the solid-state electrolyte and is given by

$$I_f = FA \sum_i z_i J_i. \quad (3.4)$$

A is geometrical surface area of the cell. The maxwell displacement current results from the frequency of electric field strength and is depicted by

$$I_d = -A\varepsilon_0\varepsilon_i \frac{\partial(\nabla\Phi)}{\partial t}. \quad (3.5)$$

3.2 Equivalent Circuit Model of Solid-State Electrolytes

Sec. 3.1 shows the numerical method for calculating the impedance of batteries, nevertheless, this methodology hardly distinguishes the impedance contribution of each part and consumes the computational resources. In comparison to the electrochemical model, the equivalent circuit model [100–104] is more simple and is able to quantify the impedance of each part. However, this model fails to explain the physical origin of battery impedance and different equivalent circuit models can produce the same result. As shown in [91, 105], two different equivalent circuit models are proposed to explain the impedance of thin film batteries, but lead to the same spectroscopy. Therefore, the electrochemical model and the corresponding equivalent circuit model are combined to analyse the battery impedance. Here, different equivalent circuit models and quantification of elements are presented in this section.

To reduce the influence factors, a metal/electrolyte/metal cell consisting of a solid-state electrolyte and a pair of electrodes is applied for the study. This cell configuration is the simplest situation and is extensively applied to measure the solid-state electrolyte impedance spectroscopy. Electron migration in electrolytes is always ignored in the electrochemical impedance models, nevertheless, electrons can move with relatively low velocity at room temperature as shown in references [106–108]. Therefore, contributions from electrons are taken into consideration in the proposed equivalent circuit model to maintain the generality. Note that elements related to ions are indicated by the subscript “+”, while electrons are denoted by “-”.

3.2.1 Ideally Conducting Electrolytes

Fig. 3.1a shows an ideally conducting solid-state electrolyte which means the fast interface reaction and no excess charges build up at the interface, i.e., $c_i^{in} = c_i^{bu}$. Here, the superscripts “in” and “bu” denote the interface and the bulk, respectively. Under this assumption, the corresponding equivalent circuit model is expressed as depicted in Fig. 3.1b, where $R_{e,+}^{bu}$ and $R_{e,-}^{bu}$ are the electrolyte ionic and electronic bulk resistances. C_e^{bu} is the bulk capacitance of the solid-state electrolyte, and n represents the number of transmission line elements and is defined as $n = L_e/x$. In addition, L_e denotes the electrolyte thickness and x is the element thickness [109, 110].

Referring to Chap. 2, the Planck-Nernst equation has been applied to explain the migration of species. Thereby, the conductivity of the component i in electrolytes is given by

$$\sigma_{e,i} = \frac{z_i^2 F^2 D_{e,i} c_{e,i}}{RT}. \quad (3.6)$$

Noted that the conductivity σ_i derivation can refer to Sec. 2.2.2. Thus, the electrolyte bulk resistance is expressed as [97]

$$R_{e,i}^{bu} = \int_0^{L_e} \frac{dx}{A\sigma_i} = \frac{RTL_e}{z_i^2 F^2 A D_{e,i} c_{e,i}^{bu}}. \quad (3.7)$$

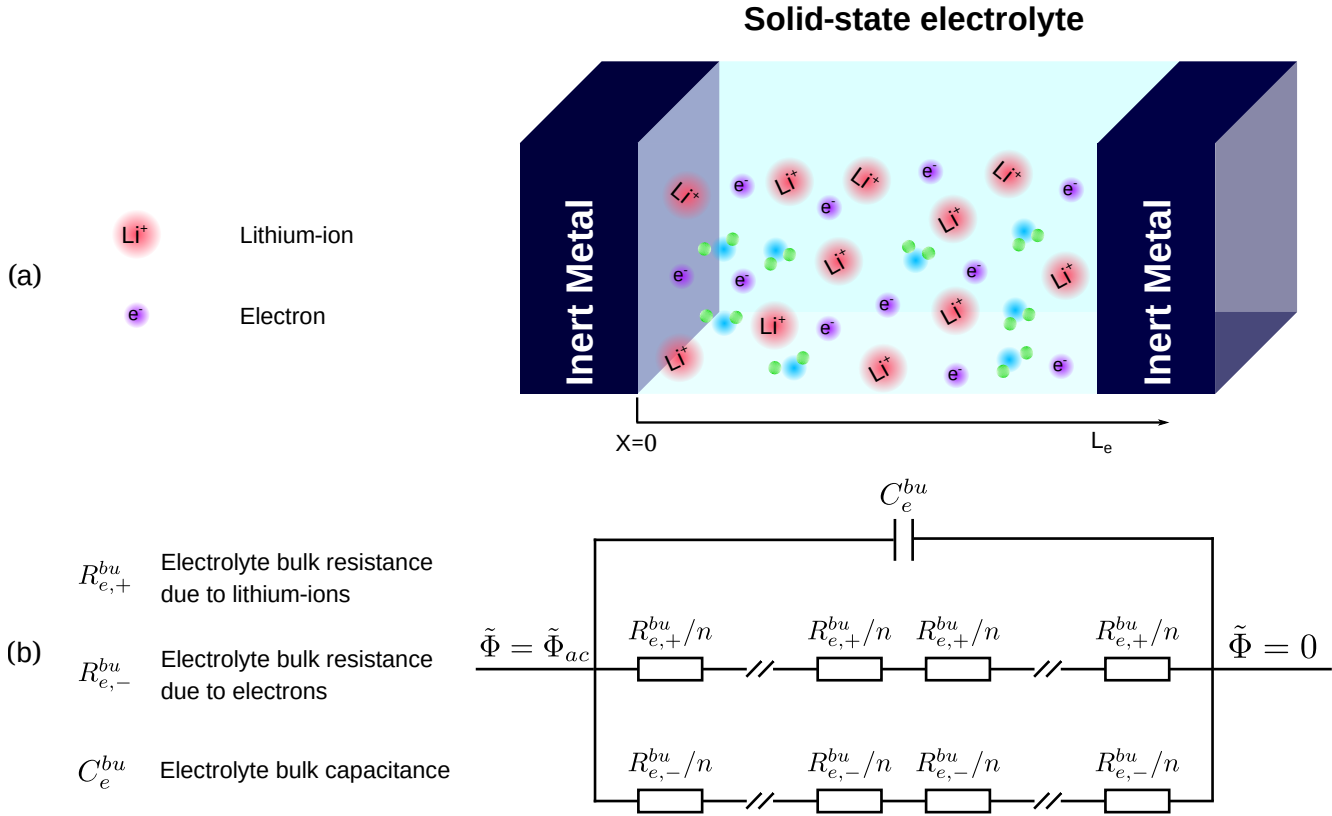


FIGURE 3.1 (a) The schematic of a metal/electrolyte/metal cell with an ideally conducting solid-state electrolyte and (b) the proposed equivalent circuit model.

It indicates that the bulk resistance is related to material properties, such as the thickness and the cross section area. The bulk capacitance of the solid-state electrolyte leads to

$$C_e^{bu} = A \frac{\varepsilon_0 \varepsilon_i}{L_e}. \quad (3.8)$$

In Eq (3.8), ε_0 and ε_i are the relative and vacuum permittivities of solid-state electrolytes, respectively. The ionic and electronic bulk resistances are in parallel with the bulk capacitance, thereby, the total impedance Z of the ideally conducting electrolyte can be obtained by Eq. (3.9), where $R_e^{bu} = R_{e,+}^{bu} R_{e,-}^{bu} / (R_{e,+}^{bu} + R_{e,-}^{bu})$ is the total bulk resistance

$$Z = \frac{1}{j\omega C_e^{bu} + 1/R_e^{bu}}. \quad (3.9)$$

Eqs. (3.7) to (3.9) are the basic equations of the proposed equivalent circuit model as depicted in Fig. 3.1b, and are widely applied to calculate the battery impedance. In order to study the influence of material properties on the ideally conducting electrolyte impedance and confirm the equivalent circuit model, the numerical calculated impedance spectroscopies are plotted here. Parameters are taken from the reference [111] and are shown in Tab. 3.1.

Parameter	Unit	Value	Description
L_e	nm	160	Thickness of the electrolyte
ε_0	F m^{-1}	8.854×10^{-12}	Vacuum permittivity
ε_i	–	78.5	Relative permittivity
F	C mol^{-1}	96 472.44	Faraday constant
T	K	298	Temperature
R	$\text{J mol}^{-1} \text{K}^{-1}$	8.314	Gas constant
$D_{e,+}$	$\text{m}^2 \text{s}^{-1}$	2×10^{-9}	Lithium-ion diffusion coefficient
$D_{e,-}$	$\text{m}^2 \text{s}^{-1}$	2×10^{-9}	Electron diffusion coefficient
$c_{e,+}$	mol m^{-3}	1	Lithium-ion concentration
$c_{e,-}$	mol m^{-3}	1	Electron concentration
z_+	–	1	Lithium-ion valence
z_-	–	–1	Electron valence
A	m^2	10^{-6}	Geometrical surface area

TABLE 3.1 Parameters taken from the reference [111].

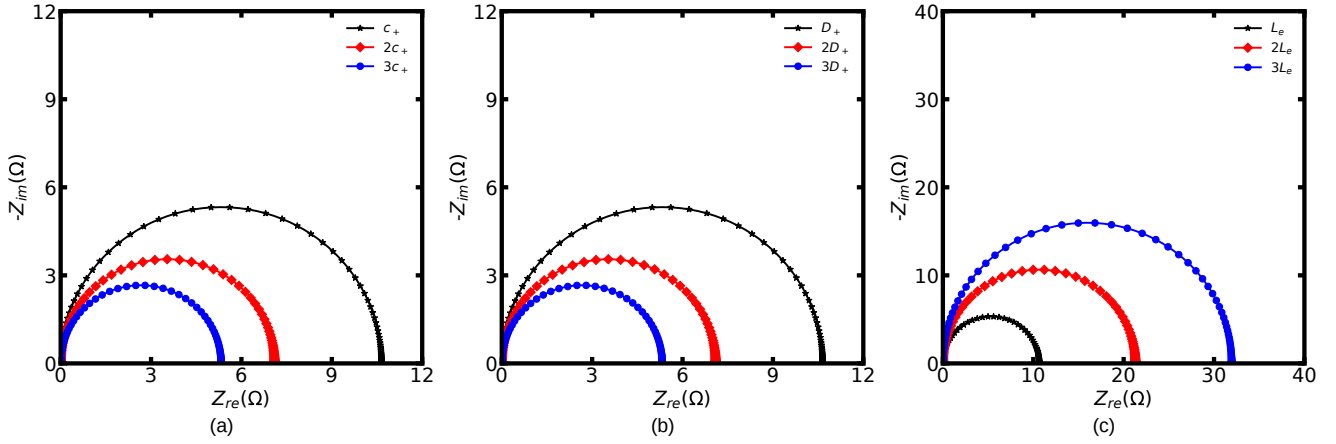


FIGURE 3.2 Nyquist plots of an ideally conducting solid-state electrolyte with different (a) concentrations, (b) diffusivities, and (c) thicknesses. Notice that the numerical results are calculated by Eq. (3.9), and the input parameters are from Tab. 3.1.

Fig. 3.2 shows the Nyquist plots of an ideally conducting solid-state electrolyte calculated by the equivalent circuit model, and each point in the impedance curves denotes a specific frequency. Results indicate that the ideally conducting electrolyte only shows a typical semicircle impedance spectroscopy, even with different material properties. Moreover, it can be read that the diameter of this semicircle is equal to the electrolyte bulk resistance. As a result, the semicircle is proportional

to the thickness and is inversely proportional to the diffusivity and the concentration.

3.2.2 Ideally Blocking Electrolytes

Sec. 3.2.1 presents the equivalent circuit model of an ideally conducting solid-state electrolyte, and shows the impedance results. Nevertheless, the influence of the space charge layer at the interface has not yet been discussed. Therefore, an ideally blocking electrolyte is presented here to discuss the impedance of the space charge layer. For the simplification, it is considered that the solid-state electrolyte is ideally blocking on the left side, i.e., $J_{e,+}(L) = J_{e,-}(L) = 0$, and the right side is assumed to be ideally conducting, i.e., $c_{e,+}(R) = c_{e,-}(R) = c$, as shown in Fig. 3.3a. This simplification corresponds to the case of an infinite solid-state electrolyte thickness and is reasonable when the space charge layer is much smaller than the electrolyte. It should be noted that the similar impedance analysis can be applied to the right-hand electrolyte interface if it is included.

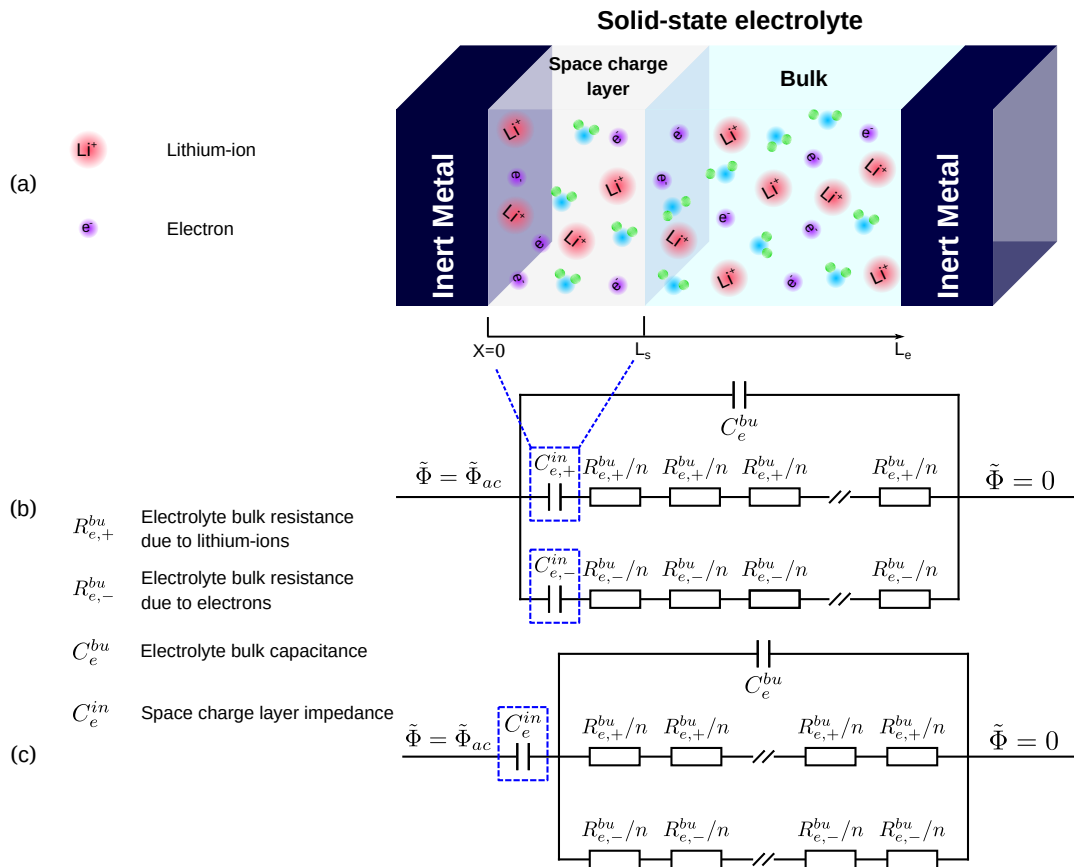


FIGURE 3.3 (a) The schematic of a metal/electrolyte/metal cell with an ideally blocking electrolyte and (b,c) the proposed equivalent circuit models.

Fig. 3.3a sketches an ideally blocking solid-state electrolyte, in comparison to Fig. 3.1a, charges accumulate at the metal/electrolyte interface with an external perturbation and the space charge

layer is built up. Figs. 3.3b and 3.3c are the two widely applied equivalent circuit models for the ideally blocking electrolyte. In present investigations, the space charge layer at the metal/electrolyte interface is regarded as an ideal capacitor [111, 112] and the impedance leads to $Z_e^{in} = 1/(j\omega C_e^{in})$. The capacitance C_e^{in} is associated with the charge density Q and the electrostatic potential Φ in the space charge layer, and is given by $C_e^{in} = -\partial Q/\partial\Phi$. According to the references [113–118], there exist different analytical solutions of the space charge layer capacitance based on the different electrochemical models. Here, we present three of them:

$$1) \quad C_e^{in} = A \frac{\varepsilon_0 \varepsilon_i}{\lambda_D} \quad (3.10)$$

$$2) \quad C_e^{in} = A \frac{4zFc\lambda_D}{\Phi} \sinh\left(\frac{zF\Phi}{2RT}\right) \quad (3.11)$$

$$3) \quad C_e^{in} = A \frac{\varepsilon_0 \varepsilon_i}{\lambda_D} \cosh\frac{zF\Phi}{2RT} \quad (3.12)$$

λ_D is the so-called Debye length and is expressed as

$$\lambda_D = \sqrt{\frac{RT\varepsilon_i\varepsilon_0}{F^2 \sum z_i^2 c}} \quad (3.13)$$

The equivalent circuit models of an ideally blocking electrolyte are shown in Figs. 3.3b and 3.3c, thereby the total impedances are given by Eqs. (3.14) and (3.15), respectively.

$$Z = \frac{1}{j\omega C_e^{bu} + \frac{1}{R_{e,+}^{bu} + 1/(j\omega C_{e,+}^{in})} + \frac{1}{R_{e,-}^{bu} + 1/(j\omega C_{e,-}^{in})}} \quad (3.14)$$

$$Z = \frac{1}{j\omega C_e^{bu} + 1/R_e^{bu}} + \frac{1}{j\omega C_e^{in}} \quad (3.15)$$

Fig. 3.4 shows the impedance results of an ideally blocking solid-state electrolyte with different material properties. It can be observed that a semicircle appears at the high-frequency range and a vertical tail is shown at low frequencies. In comparison to Fig. 3.2, the vertical tail is caused by the space charge layer capacitance shown in the equivalent circuit models. In the ideally blocking electrolyte, charges accumulate at the metal/electrolyte interface at low frequencies and leads to a large electrostatic potential drop. Therefore, the space charge layer is always regarded as a pure capacitor. Nevertheless, this assumption fails to explain some experimental observations that will be shown in Chap. 5, especially in the low-frequency region. Moreover, the analytical space charge layer capacitance of solid-state electrolytes is derived from the standard PNP model.

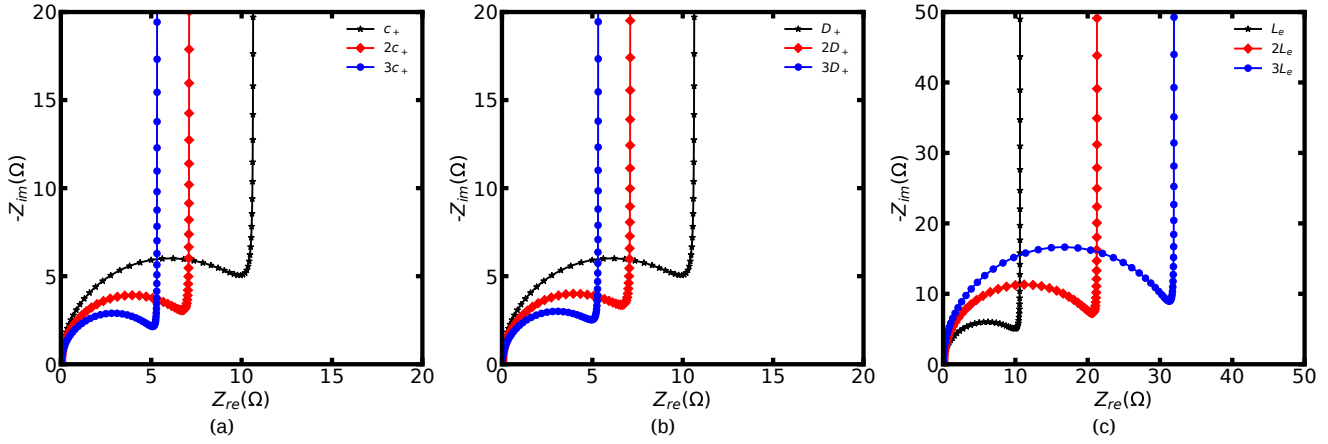


FIGURE 3.4 Nyquist plots of an ideally blocking solid-state electrolyte with different (a) concentrations, (b) diffusivities, and (c) thicknesses. Notice that numerical results are calculated by Eqs. (3.10) and (3.15), and input parameters are from Tab. 3.1.

As shown in Chap. 2, the PNP model fails to be applied in the high concentration ASSBs and the space charge layer region. Thus, the analytical space charge layer capacitance in solids based on the PNP model is questionable. To tackle these issues, a new space charge layer capacitance and more specific investigation on the space charge layer impedance will be discussed later.

3.2.3 Non-ideally Blocking Electrolytes

In previous sections, we present the impedance curves of solid-state electrolytes with two different cases and show the corresponding equivalent circuit models, i.e., ideally conducting and blocking. These conditions represent a rapid interface reaction and no reaction occurs, respectively. Thus, a more realistic situation for the solid-state electrolyte is discussed here, i.e., non-ideally blocking. Note that this case can also be applied in the impedance analysis with consideration of the grain boundary. Similar to Sec. 3.2.2, the condition is only applied on the left-hand side, and the right-hand side is ideally conducting.

Fig. 3.5a sketches the schematic of a non-ideally blocking solid-state electrolyte, and Figs. 3.5b and 3.5c are the corresponding equivalent circuit models with the limited reaction. Under this circumstance, the space charge layer is built up at the surface similar to the ideally blocking electrolyte, while the impedance becomes more complicated. According to the study, a constant resistance is included in the space charge layer with the limited reaction. Therefore, the space charge layer impedance Z_e^{in} can be expressed as

$$Z_e^{in} = \frac{1}{1/R_e^{in} + j\omega C_e^{in}}. \quad (3.16)$$

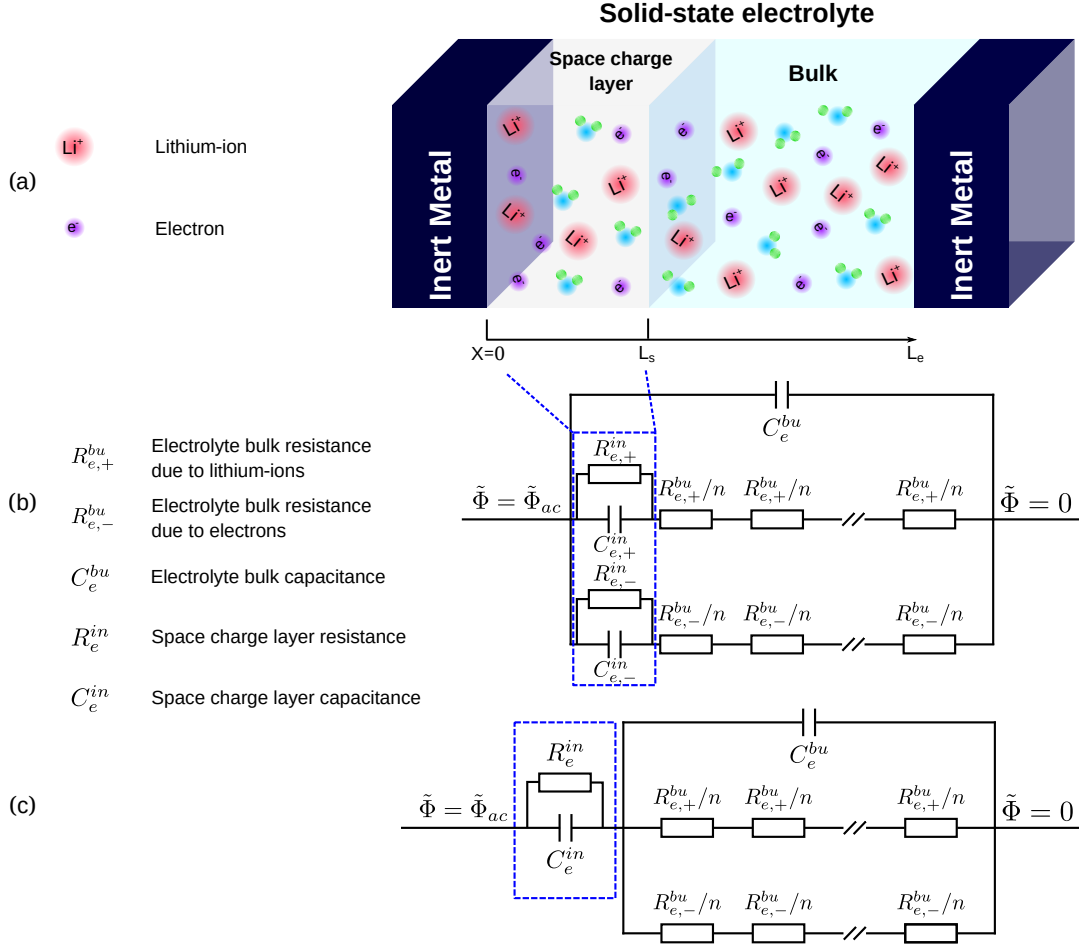


FIGURE 3.5 (a) The schematic of a metal/electrolyte/metal cell with a non-ideally blocking electrolyte and (b,c) the proposed equivalent circuit models.

Based on Figs. 3.5b and 3.5c, the total impedance of the non-ideally blocking electrolyte leads to Eqs. (3.17) and (3.18), respectively.

$$Z = \frac{1}{1/(Z_{e,+}^{in} + R_{e,+}^{bu}) + 1/(Z_{e,-}^{in} + R_{e,-}^{bu}) + j\omega C_e^{bu}}, \quad (3.17)$$

$$Z = \frac{1}{j\omega C_e^{bu} + 1/R_{e,+}^{bu} + 1/R_{e,-}^{bu}} + \frac{1}{j\omega C_e^{in} + 1/R_e^{in}}, \quad (3.18)$$

In order to investigate the influence of material properties on the non-ideally blocking electrolyte, the calculated impedance spectroscopies are shown in Fig. 3.5, in which $R_e^{in} = 10 \Omega$ is adopted.

Fig. 3.6 shows the Nyquist plots of solid-state electrolytes with considering limited lithium-ion reaction at the metal/electrolyte interface. In comparison to Figs. 3.2 and 3.4, it can be observed that two semicircles appears even with different material properties. Therefore, the second semicircle at the low-frequency region is caused by the space charge layer. It can be read that the diameter of the second semicircle is 10Ω and corresponds to the space charge layer resistance.

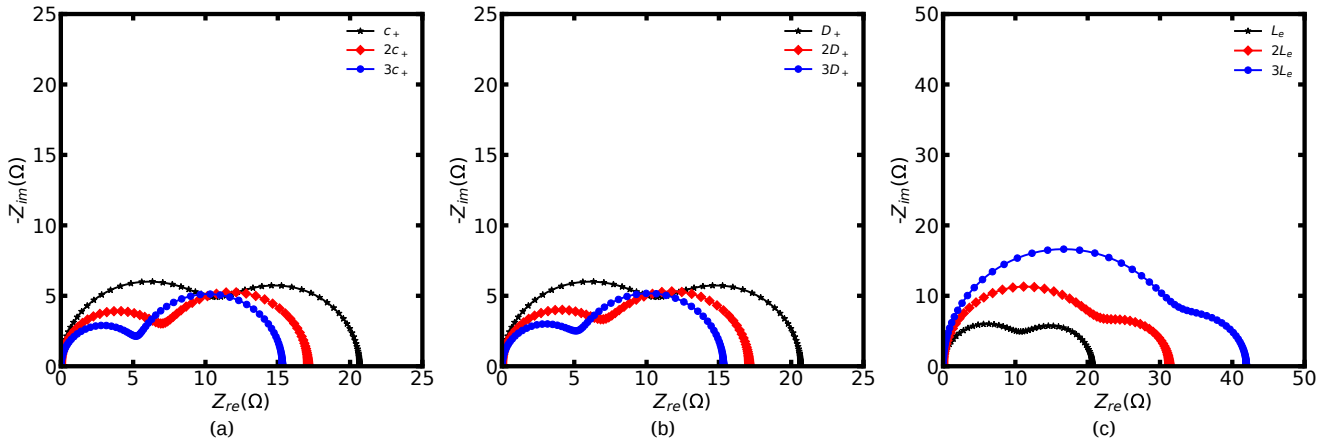


FIGURE 3.6 Nyquist plots of a non-ideally blocking solid-state electrolyte with different (a) concentrations, (b) diffusivities, and (c) thicknesses. Notice that numerical results are calculated by Eqs. (3.10) and (3.18), and input parameters are from Tab. 3.1.

Moreover, results show that material properties have no impact on the impedance spectroscopy caused by the space charge layer.

Based on the discussion, it can be concluded that the space charge layer plays an important role in the impedance spectroscopy. With the fast reaction, i.e., the ideally conducting electrolyte, lithium-ions cannot accumulate at the interface and form the space charge layer. Therefore, the impedance spectroscopy of solid-state electrolytes is a semicircle, as shown in Fig. 3.2. With the reaction rate decreasing, i.e., the non-ideally blocking electrolyte, lithium-ions accumulate at the interface and the space charge layer is built up. Under this circumstance, the space charge layer resistance caused by the reaction is also taken into consideration. Consequently, two semicircles appear in Fig. 3.5 and the second one is associated with the space charge layer. When the reaction rate continuously decreases, i.e., the ideally blocking electrolyte, the space charge layer will build up at the interface due to the applied perturbation potential. The space charge layer resistance can be ignored and only the space charge layer capacitance is included under this condition. Thus, the impedance curve is a vertical line at low frequencies, as depicted in Fig. 3.5c.

3.3 Equivalent Circuit Models of ASSBs

Sec. 3.2 introduces the widely applied equivalent circuit models of solid-state electrolytes and discuss the impedance plots with different cases. Nevertheless, lithium-ion reaction at the interface is not coupled in these equivalent circuit models. Moreover, the quantification of the charge transfer resistance has not been presented. To solve these problems, a half cell consisting of a cathode and a solid-state electrolyte is employed in this section to show the derivation of the

charge transfer resistance. Notice that we only present the equivalent circuit model for the solid-state electrolyte, and it can also be used to estimate the cathode impedance if needed.

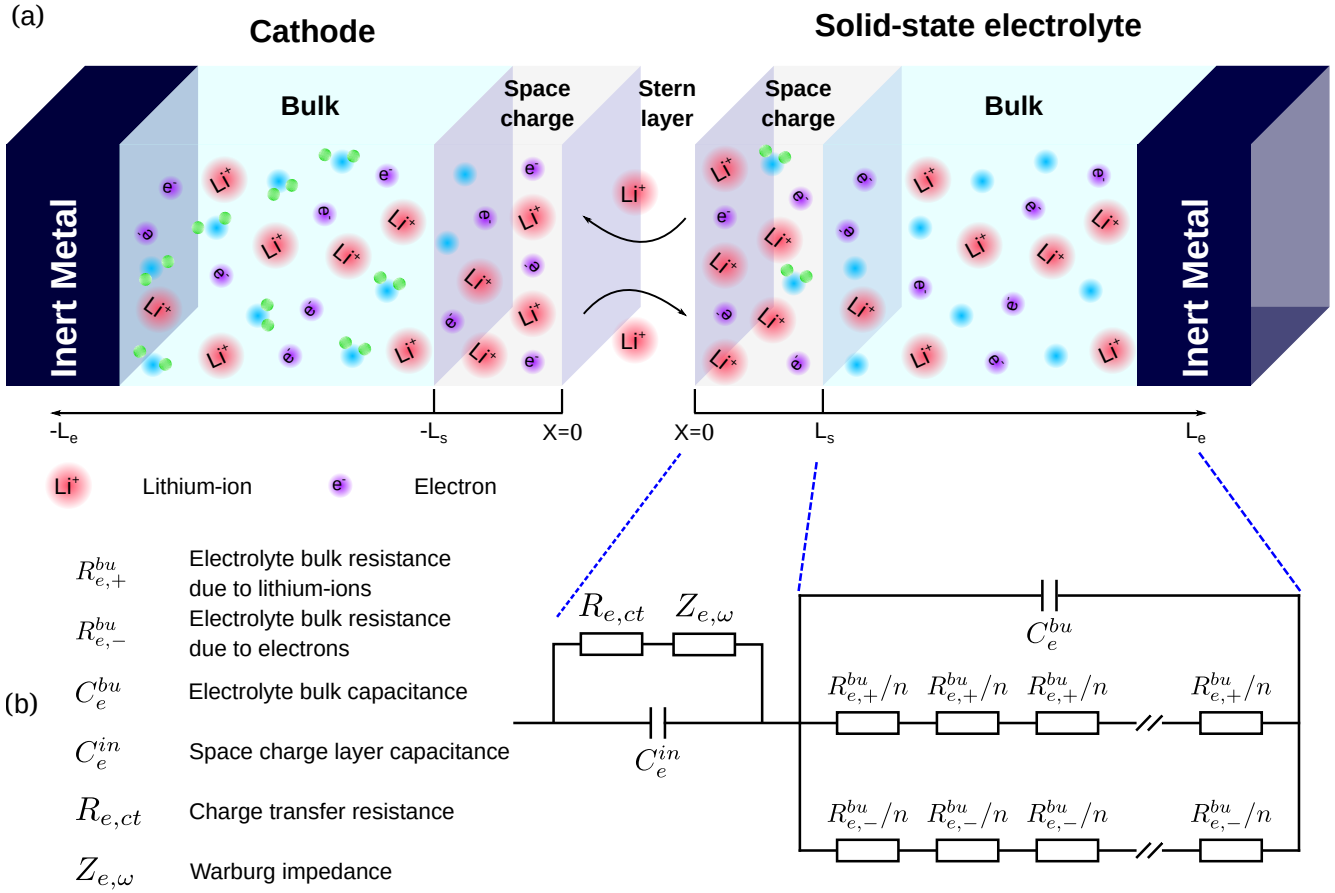


FIGURE 3.7 (a) The schematic of a cathode/electrolyte half cell with the space charge layer at the interface and (b) the proposed equivalent circuit model for electrolyte [68].

Fig. 3.7 shows the schematic of a half cell and the corresponding equivalent circuit model only for the solid-state electrolyte. Lithium-ion reaction happens at the metal/electrolyte interface, thus the space charge layer is built up, as shown in Fig. 3.7a. In addition to the space charge layer capacitance and the charge transfer resistance, the Warburg impedance Z_ω caused by the diffusion-limited process is also included, as shown in Fig. 3.7b. According to Sec. 2.4, lithium-ion reaction at the interface and the current are given by



$$I = I_0 \left\{ \frac{c_c}{c_c^{eq}} \exp \left[\frac{\beta F \eta}{RT} \right] - \frac{c_e}{c_e^{eq}} \exp \left[-\frac{(1-\beta) F \eta}{RT} \right] \right\}. \quad (3.20)$$

η is the overpotential and $\eta = \Delta\Phi_s - \Delta\Phi_s^{eq}$, I_0 is the exchange current and is related to the free enthalpy difference. By assuming a sufficiently small overpotential $\eta \rightarrow 0$, thus small deviations of

the concentrations form their initial value and the exponents are close to zero. We can linearize the exponential functions $e^x|_{x=0} \approx x$, and obtain

$$I \approx I_0 \left[\frac{F\eta}{RT} + \ln \left(\frac{c_c}{c_c^{eq}} \right) - \ln \left(\frac{c_e}{c_e^{eq}} \right) \right]. \quad (3.21)$$

Thereafter, we linearize the natural logarithms using $\ln(x)|_{x=1} \approx x - 1$, and Eq. (3.21) leads to

$$I \approx I_0 \left[\frac{F\eta}{RT} + \frac{c_c - c_c^{eq}}{c_c^{eq}} - \frac{c_e - c_e^{eq}}{c_e^{eq}} \right]. \quad (3.22)$$

The impedance at the cathode/electrolyte interface is defined as

$$Z = \frac{\eta}{I} = \frac{RT}{FI_0} - \frac{RT}{FI} \frac{c_c - c_c^{eq}}{c_c^{eq}} + \frac{RT}{FI} \frac{c_e - c_e^{eq}}{c_e^{eq}}. \quad (3.23)$$

Thus, the charge transfer resistance shown in Fig. 3.7b yields

$$R_{ct} = \frac{RT}{FI_0}. \quad (3.24)$$

The impedance caused by concentration diffusion in the electrolyte is given by

$$Z_e^d = \frac{RT}{FI} \frac{c_e - c_e^{eq}}{c_e^{eq}}. \quad (3.25)$$

similarly, the impedance in the cathode leads to

$$Z_c^d = -\frac{RT}{FI} \frac{c_c - c_c^{eq}}{c_c^{eq}}. \quad (3.26)$$

Eqs. (3.25) and (3.26) are commonly referred to the Warburg impedance [119], which are related to the diffusional (or mass transfer) impedance of electrochemical systems. Moreover, it should be noted that η , I and c are frequency-dependent. According to different boundary conditions, the Warburg impedance can be clarified into three forms, i.e., the Semi-Infinite Warburg (SIW) impedance, the Finite-Length Warburg (FLW) impedance, and the Finite-Space Warburg (FSW) impedance. To give a specific discussion about the Warburg impedance, the simple diffusion equation is applied for the ion material balance in the system [120, 121]

$$\frac{\partial c}{\partial t} = D\nabla^2 c. \quad (3.27)$$

In the presence of a perturbation, the concentration can be given by

$$c = c_{dc} + c_{ac}(e^{j\omega t}). \quad (3.28)$$

Where c_{dc} corresponds to the concentration at the steady state and is not time dependent, and c_{ac} is the amplitude of time-dependence concentration. By using Eq. (3.28), the diffusion equation

can be reduced to Eq. (3.29) in frequency-space domain through the Fourier transformation [120, 122]

$$j\omega c_{ac} = D\nabla^2 c_{ac}. \quad (3.29)$$

The analytical solutions of Eq.(3.29) for particular situations have already been derived , and the general form of results are given here:

- 1) The Semi-Infinite Warburg (SIW) impedance [123, 124]

$$x = 0, D\nabla c_{ac} = \vec{n} \cdot \frac{I_{ac}}{F} \quad x \rightarrow \infty, c_{ac} \rightarrow 0$$

$$Z_{SIW} = \frac{B}{\sqrt{j \cdot a(\omega)}}. \quad (3.30)$$

- 2) The Finite-Length Warburgs (FLW) impedance [109, 119]

$$x = 0, D\nabla c_{ac} = \vec{n} \cdot \frac{I_{ac}}{F} \quad x = L_e, c_{ac} = 0$$

$$Z_{FLW}(\omega) = B \frac{\tanh \sqrt{j \cdot a(\omega)}}{\sqrt{j \cdot b(\omega)}}. \quad (3.31)$$

- 3) The Finite-Space Warburg (FSW) impedance [109, 119, 125]

$$x = 0, D\nabla c_{ac} = \vec{n} \cdot \frac{I_{ac}}{F} \quad x = L_e, \nabla c_{ac} = 0$$

$$Z_{FSW}(\omega) = B \frac{\coth \sqrt{j \cdot a(\omega)}}{\sqrt{j \cdot b(\omega)}}. \quad (3.32)$$

In Eqs. (3.30) to (3.32), L_e is the thickness, B is a coefficient, j is the imaginary number, $a(\omega)$ and $b(\omega)$ are dimensionless quantities proportional to ω . Thus, we plot a graphical comparison of these different Warburg impedances in Fig. 3.8. Fig. 3.8a is the Nyquist plot of the Semi-Infinite Warburg impedance, and the curve is a straight line with a 45° slop. This behaviour has been widely observed in the impedance spectroscopy. It is evident that as the frequency increases, the magnitude of the Warburg impedance decrease. At the high-frequency region, the rapid reversals of the reaction direction at the electrode surface, change in concentration are no longer propagated into the electrolyte and electrode, and the overpotential associated with diffusion therefore vanishes [68]. The Finite-Length Warburg impedance plot shows the evident difference in comparison to Fig. 3.8a, the 45° straight line only appears at the high-frequency side and a semi-circular arc at its low-frequency side, that is, has a half tear-drop shape [109], as shown in Fig. 3.8b. Fig. 3.8c depicts the Nyquist plot of the Finite-Space Warburg impedance, and is

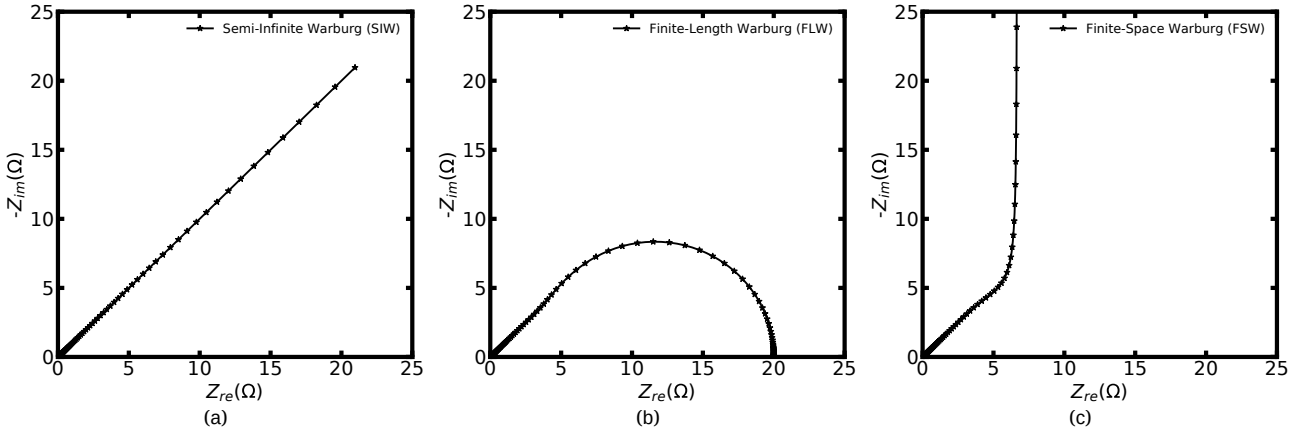


FIGURE 3.8 (a) The Semi-Infinite Warburg impedance calculated by Eq. (3.30), (b) the Finite-Length Warburg impedance calculated by Eq. (3.31) and (c) the Finite-Space Warburg impedance calculated by Eq. (3.32). Note that the coefficient is $Z = 20 \Omega$ and functions $a(\omega) = b(\omega) = \omega$ are adopted in the calculation.

similar to the Finite-Length Warburg impedance at high frequencies while showing a vertical line at its low-frequency side.

To continue the discussion, we take a further step and present the calculated impedance spectroscopy based on the equivalent circuit model for electrolytes in the half cell. According to Fig. 3.7b, the electrolyte impedance equation leads to

$$Z = \frac{1}{j\omega C_e^{bu} + 1/R_e^{bu}} + \frac{1}{j\omega C_e^{in} + 1/(R_{e,ct} + Z_{e,\omega})} \quad (3.33)$$

Thereby, the Nyquist plots of electrolytes with considering the different Warburg impedances are presented in Fig. 3.9, in which $R_{e,ct} = 10 \Omega$ is adopted.

As shown in Fig. 3.9, the Nyquist plots can be divided into three parts, e.g. the first semicircle ($0 \leq Z_{re} \leq 10 \Omega$), the second semicircle ($10 \leq Z_{re} \leq 20 \Omega$), and the tail ($20 \Omega \leq Z_{re}$). The first semicircle is caused by the first term at the right-hand side in Eq. (3.33), which represents the electrolyte bulk impedance. The charge transfer resistance $R_{e,ct}$ and the space charge layer capacitance C_e^{in} lead to the second semicircle, thus this part is determined by the exchange current and the charge density at the interface. Eventually, the tail represents the diffusion-limited Warburg impedance in the space charge layer. It should be noted that this circuit model merely shows the electrolyte impedance, shown in Fig. 3.7, and is just one of the extensively applied frameworks for battery circuit model. Moreover, the similar model of the electrode can be included later if needed.

Besides these Warburg impedances, Maier also proposed another formula to explain the diffusional impedance and is given as [126, 127]

$$Z_w = -\frac{2RT\lambda_D}{z_i^2 F^2 A D_i C_i^{bu}} \frac{2\theta}{1+\theta} \quad (-1 \leq \theta \leq 1). \quad (3.34)$$

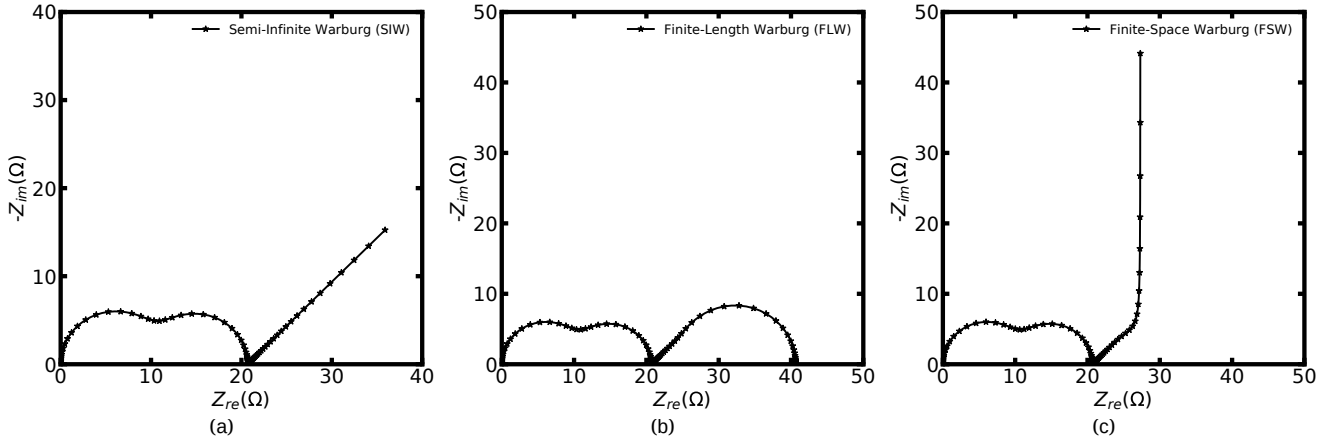


FIGURE 3.9 (a) The total electrolyte impedance with the Semi-Infinite Warburg impedance by Eq. (3.30), (b) with the Finite-Length Warburg impedance by Eq. (3.31), and (c) with the Finite-Space Warburg impedance by Eq. (3.32).

Where θ is called the “degree of influence” and denotes the influence of the neighbouring phase on the space charge layer. It can be observed that θ depends on the frequency and is difficult to identify, therefore this equation is barely applied in calculating the battery impedance.

3.4 Impedance Calculation Benchmark

To verify the methodology for calculating the impedance of electrochemical models, the corresponding benchmark results are presented in this section. The example is taken from the reference [111], where the standard PNP model is applied with one dimensional geometry. The initial concentrations are $c_{e,+} = c_{e,-} = 1 \text{ mol m}^{-3}$, the identical diffusion coefficients are $D_{e,+} = D_{e,-} = 2 \times 10^{-8}, 2 \times 10^{-9}, 2 \times 10^{-10} \text{ m}^2 \text{ s}^{-1}$, and the frequency range is $10 < \omega < 10^7 \text{ Hz}$. The ideally blocking electrolyte is considered, therefore, the boundary conditions are given by $J_{e,+}(L) = J_{e,-}(L) = 0$ on the left-hand side, and $c_{e,+}(R) = c_{e,-}(R) = c$ on the right-hand side, respectively. The time independent potential $\Phi_{dc} = 0.1 \text{ V}$, and the amplitude of the potential oscillation is $\Phi_{dc} = 0.001 \text{ V}$. In addition, the Stern layer has been ignored when solving the standard PNP model. More parameters of the electrolyte are given in Tab. 3.1.

Fig. 3.10 shows the specific capacitance from the impedance simulation as a function of frequency ω . It can be seen that the calculated results agree very well with the reference and confirms the numerical calculation. Moreover, the numerical result at low frequencies represents the space charge layer capacitance. Results show that the space charge layer capacitance is a constant, even with different diffusion coefficients. This conclusion is also drawn from the analytical solutions, as depicted in Eqs. (3.10) to (3.12).

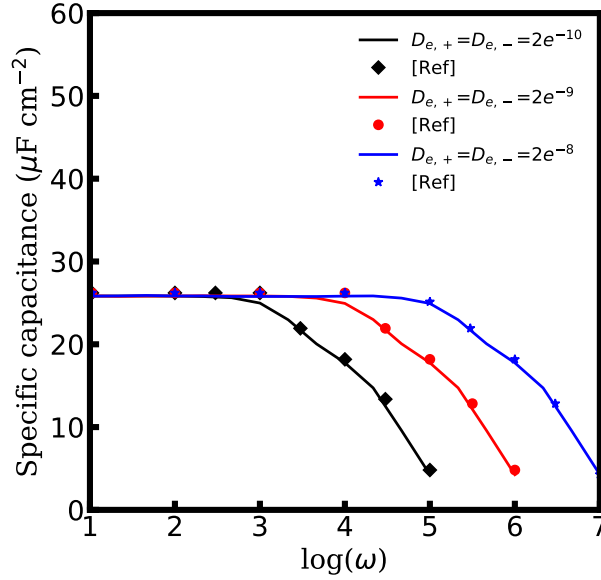


FIGURE 3.10 Specific capacitance as a function of frequency.

3.5 Summary

The electrochemical model, the numerical methodology and the corresponding equivalent circuit models for calculating the impedance of ASSBs have been proposed in this chapter. For simplification, the solid-state electrolyte is employed to quantify elements in the equivalent circuit model. In addition, the concentration and the electrostatic potential distributions are modelled by the standard PNP model. Based on the electrochemical model, the analytical solutions of the electrolyte bulk resistance R_i^{bu} , the bulk capacitance C_i^{bu} , and the space charge layer capacitance C_i^{in} are proposed. Note that all the solutions are associated with material properties. To show the influence of material properties on the electrolyte impedance spectroscopy, three different cases are discussed here, i.e., ideally conducting, ideally blocking, and non-ideally blocking. Results show that the impedance spectroscopy of the ideally conducting electrolyte is a semi-circle, and the diameter is equal to the electrolyte bulk resistance. Thereafter, the space charge layer impedance is discussed with the different equivalent circuit models. The space charge layer is assumed as a pure capacitor in the ideally blocking electrolyte, thus, a vertical line appears at low frequencies. For the non-ideally blocking electrolyte, the space charge layer resistance is included and the impedance spectroscopy obtains another semicircle. Thereafter, we take a further step and investigate the impedance of a half cell. Lithium-ion reaction at the interface has been taken into account, and the derivation of the charge transfer resistance is presented in detail. It is recognized that a diffusion-limited process can lead to the Warburg impedances with different boundary conditions, e.g., the Semi-Infinite Warburg, the Finite-Length Warburg, and the Finite-Space Warburg. Thus, a graphical comparison of Warburg impedance is also shown in this work, and we can observe the difference between these patterns. To verify the numerical

methodology of the impedance calculation, a benchmark test is shown in Sec. 3.4. The ideally blocking electrolyte and the standard PNP model are applied, and the numerical results agree very well with the reference. Therefore, it indicates the numerical calculation and the methodology are accurate.

4 Interface Equilibrium of ASSBs

Noted that this chapter is based on the publication “Y. Liu, Y.-B. Ma, W. Jaegermann, R. Hausbrand, and B.-X. Xu, *Journal of Power Sources* 454, 227892 (2020)”.

As shown in Chap. 2, the widely applied electrochemical models for ASSBs ignore the vacancy effect in solids. Consequently, these models fail to investigate the interface behaviours or highly concentrated electrolytes. Therefore, a physical model for ASSBs is still indispensable. Moreover, current studies of battery modelling concentrate on the dynamic process, e.g., the charging and discharging process. The intrinsic equilibrium state and the exchange current caused by the free enthalpy difference of materials are never addressed before. However, the exchange current is a crucial parameter for the evaluation of the interface impedance and is also extensively used in the electrochemical models.

Thereby, in this chapter, we first introduce an advanced electrochemical model for ASSBs, which takes the electrical double layer structure and the vacancy effect into consideration. Thereafter, the intrinsic equilibrium state of battery is revealed and the exchange current is numerically calculated for the first time on the basis of the proposed electrochemical model. The numerical results are verified from the chemical perspective and the interface experimental results. Consequently, it can provide better identification of the origin of the high interface impedance in ASSBs. The structure of this chapter is organized as followed: In Sec. 4.1, the advanced electrochemical model for ASSBs, and the set of boundary and interface conditions are presented. A benchmark test for the model is also shown in this section. The role of the vacancy effect in solid materials is addressed in Sec. 4.2. Secs. 4.3 to 4.5 present the intrinsic equilibrium state of a half cell and study the influence of concentrations, diffusion coefficients and interface structures. Sec. 4.6 gives a short summary and prospects.

4.1 Electrochemical Model

Different binding energies (energy levels) of materials [128–130] result in initially different activation energies for lithium-ions transfer from the electrode to the electrolyte and vice versa, which are compensated by changes in the electrostatic potentials and by the concentration changes upon the formation of the intrinsic equilibrium state. However, this phenomenon is

hardly addressed by the commonly used electrochemical models, e.g., the PNP model and the P2D model. For the purpose of investigating the intrinsic equilibrium state of ASSBs, an advanced electrochemical model is proposed in this section. The vacancy effect for lithium-ions hopping in solids is taken into account, and no assumptions are required in this model. To correlate the reaction kinetics with the electrical double layer (EDL) structure at the interface, the Frumkin-Butler-Volmer (FBV) equation has been employed. In addition, the influence of the available lattice sites for the reaction is also included.

4.1.1 Governing Equations

Referring to Sec. 1.2.2, ionic transportation mainly relies on the number of vacancies in crystalline solid materials. Therefore, the chemical potential is expressed as $\mu_i^* = \mu_i^\ominus + RT \ln x_i - RT \ln(1 - x_i)$ in this work. The electrochemical potential and the flux lead to

$$\mu_i = \mu_i^\ominus + RT \ln \frac{x_i}{1 - x_i} + z_i F \Phi, \quad (4.1)$$

$$J_i = -\frac{D_i}{1 - \tilde{c}_i} \nabla c_i - z_i \frac{F D_i}{RT} c_i \nabla \Phi. \quad (4.2)$$

A material balance for the species in solids yields

$$\frac{\partial c_i}{\partial t} = \frac{D_i}{1 - \tilde{c}_i} \nabla^2 c_i + z_i \frac{F D_i}{RT} \nabla \cdot (c_i \nabla \Phi). \quad (4.3)$$

In comparison to the standard Planck-Nernst equation, Eq. (4.3) is called the modified Planck-Nernst equation. \tilde{c}_i refers to the dimensionless concentration and the new term $1 - \tilde{c}_i$ represents the dimensionless vacancies in solids. More details about the vacancy effect will be provided in the following sections.

In most work of ASSBs modelling, electrons are assumed immobile in the electrolyte [62, 131, 132]. However, electrons can move with low velocity in electrolytes due to the electric field in real materials. To take the influence of electrons into consideration, Eq. (4.3) has been employed for estimating electrons migration. Note that in the following context, lithium-ions are indicated by the subscript “+”, while electrons are denoted by “-”, respectively. The species migration in the electrode is always described by the Fick’s law, and this simplification is reasonable in the bulk because electrons move faster than lithium-ions and the electrical neutrality condition is satisfied. However, the hypothesis cannot be applied at the interface. Consequently, the migration of electrons and the electric field in the electrode are taken into account in our model, and the transportation equation is also described by modified Planck-Nernst equation. The electrostatic potential is given by the Poisson equation and is expressed as

$$\nabla^2 \Phi = -\frac{F}{\varepsilon_i \varepsilon_0} \sum_i z_i c_i, \quad (4.4)$$

In summary, Eqs. (4.3) and (4.4) are called the modified Planck-Nernst-Poisson (MPNP) model, and more details about the electrochemical potential can refer to Chap. 2.

4.1.2 The Reaction Kinetics with Vacancies

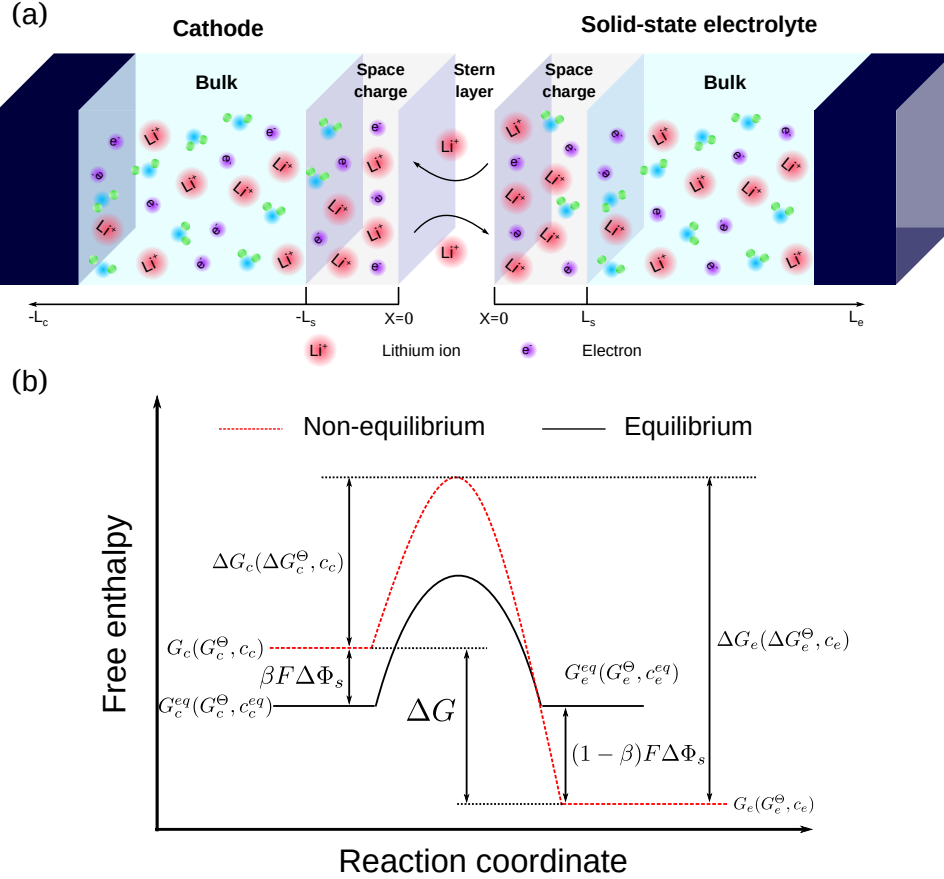
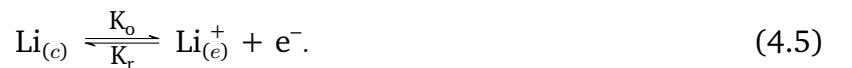
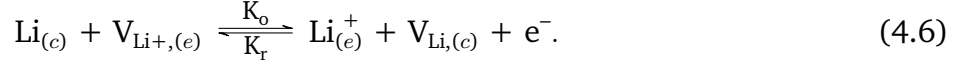


FIGURE 4.1 (a) Schematic of the electrical double layer (EDL) structure and (b) the free enthalpy profile of lithium-ion reaction at the electrode/electrolyte interface.

To study the intrinsic equilibrium state of ASSBs, a half cell consisting of a cathode and a solid-state electrolyte is applied for simplification, as shown in Fig. 4.1a. To confirm its consistency with the experimental results published in the references. [90, 133, 134], LiCoO_2 is considered as the cathode material [135, 136], and LiPON is regarded as the solid-state electrolyte. The free enthalpy difference is set to $\Delta G = 0.3 \text{ eV}$ in our work, and this value is consistent with the expected value of the ionic contribution to the cell voltage as deduced from differences in (electronic) work functions between LiCoO_2 and LiPON. The electrochemical reaction at the cathode/electrolyte interface is represented by



Nevertheless, the available vacancies at the interface for hopping ions are ignored in this formula, and the new reaction in our model yields



$\text{V}_{\text{Li}, (c)}$ and $\text{V}_{\text{Li}+, (e)}$ are the unoccupied regular lattice sites (vacancies or defects) in the cathode and the solid-state electrolyte, respectively. In contrast to previous works, we include the interface vacancy effect by assuming a limited amount of unoccupied regular lattice sites, which will result in a more realistic charge transfer reaction at the interface. Thus, the new Frumkin-Butler-Volmer (FBV) interface condition is applied, and the initial fluxes are given by

$$\begin{aligned} J_c &= K_o \exp\left(-\frac{F\Delta G^\ominus}{RT}\right) c_c c_{v,e} \\ J_e &= K_r \exp\left(-\frac{F\Delta G^\ominus}{RT}\right) c_e c_{v,c} \end{aligned} \quad (4.7)$$

$c_{v,e}$ and $c_{v,c}$ are the vacancy concentrations and are defined as $c_{v,e} = c_{max} - c_e$, $c_{v,c} = c_{max} - c_c$, where c_{max} is the maximum lithium-ion concentration of materials. The subscripts ‘‘c’’ and ‘‘e’’ denote the cathode and the electrolyte, respectively. After the electrostatic potential difference $\Delta\Phi_s$ is built up, the partial fluxes lead to

$$\begin{aligned} J_c &= K_o \exp\left(-\frac{F\Delta G^\ominus}{RT}\right) \exp\left[\frac{\beta F\Delta\Phi_s}{RT}\right] c_c [c_{max} - c_e] \\ J_e &= K_r \exp\left(-\frac{F\Delta G^\ominus}{RT}\right) \exp\left[-\frac{(1-\beta)F\Delta\Phi_s}{RT}\right] c_e [c_{max} - c_c] \end{aligned} \quad (4.8)$$

Consequently, Eqs. (4.3), (4.4) and (4.8) compose the framework of the MPNP-FBV model. The electrostatic potential difference and the flux at the intrinsic equilibrium state yield

$$\Delta\Phi_s^{eq} = \frac{RT}{F} \ln \frac{K'_r}{K'_o} + \frac{RT}{F} \ln \frac{c_e^{eq}}{c_c^{eq}} + \frac{RT}{F} \ln \frac{c_{max} - c_c^{eq}}{c_{max} - c_e^{eq}}, \quad (4.9)$$

$$J_0 = (K'_o)^{1-\beta} (K'_r)^\beta (c_c^{eq})^{1-\beta} (c_{max} - c_e^{eq})^{1-\beta} (c_e^{eq})^\beta (c_{max} - c_c^{eq})^\beta, \quad (4.10)$$

where K'_r and K'_o are given by

$$K'_o = K_o \exp\left(-\frac{F\Delta G^\ominus}{RT}\right) \quad K'_r = K_r \exp\left(-\frac{F\Delta G^\ominus}{RT}\right). \quad (4.11)$$

4.1.3 Boundary Conditions

Concerning the calculation of the intrinsic equilibrium state, the half cell is totally blocking without any external perturbation, thus the fluxes of species are given by $J_c(L) = J_e(R) = 0$. It is assumed that the left-hand side of the half cell is grounded and the right-hand side is open circuit,

thereby the boundary conditions of the electrostatic potentials at sides are defined as $\Phi_e(L) = 0$ and $\nabla\Phi_e(R) = 0$, respectively. Moreover, to improve the convergence of numerical calculation, we rescale all variables appropriately. The dimensionless parameters are given as following

$$\tilde{L} = \frac{L}{L_0} \quad \tilde{t} = \frac{t}{t_0} \quad \tilde{c} = \frac{c}{c_{max}} \quad \tilde{\Phi} = \frac{F}{RT}\Phi \quad \tilde{D} = D\frac{t_0}{L_0^2}. \quad (4.12)$$

Moreover, two simplified assumptions are adopted in the MPNP-FBV model: (i) lithium-ions reaction only occurs at the interface; (ii) electrons are mobile in the bulk but cannot traverse the interface. For simplicity and saving computation cost, one dimensional geometry of the half cell is considered.

4.1.4 Benchmark

To verify the numerical solution of the MOOSE framework and the boundary conditions, we firstly simulated the example presented in Rossi's work [137], where the PNP-FBV model was applied with the fixed negative species in the non-blocking electrolyte. The electrolyte thickness $L_e = 175 \mu\text{m}$ and the width of the Stern layer equals to the diffuse layer (or called the space charge layer in solids), where $\lambda_s = 0.03L_e$. The concentration of lithium-ions in the electrode is assumed to be constant during the dynamic process and the value is $c = 1200 \text{ mol m}^{-3}$. The electrochemical cell operates under the potentiostatic condition and the dimensionless voltage is $\tilde{\Phi} = 2.696$. The time evolution of the concentration and the flux profiles in the electrolyte have been plotted in Fig. 4.2. The plot shows that our results coincide well with the reference and indicates the numerical solutions are correct.

4.2 Vacancy Effect in ASSBs

The chemical potentials with and without the vacancies in solids have been clearly shown in Sec. 2.1 from the basic thermodynamic derivation, nevertheless, the specific influence on ASSBs modelling are not shown yet [57, 58]. Therefore, the role of the vacancy effect in solids is investigated in this section. Depending on the position, the vacancies are classified as bulk vacancies and interface vacancies within our work. Here, we compare the intrinsic equilibrium state between the MPNP model and the PNP model with the same boundary conditions to show the influence of bulk vacancies. To concentrate on the bulk vacancy effect, the FBV interface condition without considering the vacancies [74, 131] is applied for comparison purpose, as shown in Eq. (4.13),

$$J = K'_o \exp\left[\frac{\beta F \Delta\Phi_s}{RT}\right] c_c - K'_r \exp\left[-\frac{(1-\beta)F \Delta\Phi_s}{RT}\right] c_e. \quad (4.13)$$

Parameter	Unit	Value	Description
L_e	nm	50	Thickness of the electrolyte (LiPON) ^a
L_c	nm	50	Thickness of the cathode (LiCoO ₂) ^a
λ_s	nm	0.3	Thickness of the Stern layer ^b
$D_{c,+}$	m ² s ⁻¹	10 ⁻¹³	Diffusivity of lithium ions in the cathode ^a
$D_{c,-}$	m ² s ⁻¹	10 ⁻¹¹	Diffusivity of electrons in the cathode ^a
$D_{e,+}$	m ² s ⁻¹	10 ⁻¹³	Diffusivity of lithium ions in the electrolyte ^b
$D_{e,-}$	m ² s ⁻¹	10 ⁻¹⁵	Diffusivity of electrons in the electrolyte ^a
ΔG_c^\ominus	eV	0.5	Activation energy barrier (LiCoO ₂) ^b
ΔG_e^\ominus	eV	0.8	Activation energy barrier (LiPON) ^b
ε_0	F m ⁻¹	8.85 × 10 ⁻¹²	Vacuum permittivity
ε_e	-	80	Relative permittivity in the electrolyte ^a
ε_c	-	80	Relative permittivity in the cathode ^a
c_{max}	mol m ⁻³	10 ⁴	Maximum lithium ions concentration ^a
c_e	mol m ⁻³	5 × 10 ³	Initial concentration in the electrolyte ^a
c_c	mol m ⁻³	5 × 10 ³	Initial concentration in the cathode ^a
β	-	0.5	Symmetry factor ^b
F	C mol ⁻¹	96 485	Faraday constant
T	K	298.15	Temperature
R	J mol ⁻¹ K ⁻¹	8.314	Gas constant
z_+	-	1	Lithium ion valence
z_-	-	-1	Electron valence
K_o	m ⁴ mol ⁻¹ s ⁻¹	0.1	Oxidation reaction rate ^a
K_r	m ⁴ mol ⁻¹ s ⁻¹	0.1	Reduction reaction rate ^a
A	m ²	10 ⁻⁴	Geometrical surface ^a

TABLE 4.1 ^aDesigned parameters and ^bparameters are taken from Landstorfer, Okubo and Mei separately et al. [94, 130, 131]

Thereafter, we employ the MPNP model with the different FBV interface conditions, i.e., with and without the interface vacancies, and discuss the influence of the vacancy effect on lithium-ion reaction. The thickness of the Stern layer is $\lambda_s = 0.3$ nm and other material parameters are shown in Tab. 4.1. Because the concentration and the electrostatic potential change rapidly near the interface region, enlarged results at the interface are plotted.

The concentration and the electrostatic potential distributions at the intrinsic equilibrium with these two models are shown in Fig. 4.3. It can be observed that Figs. 4.3a and 4.3b show the shortcoming of the standard PNP model when investigating the interface behaviours in solids.

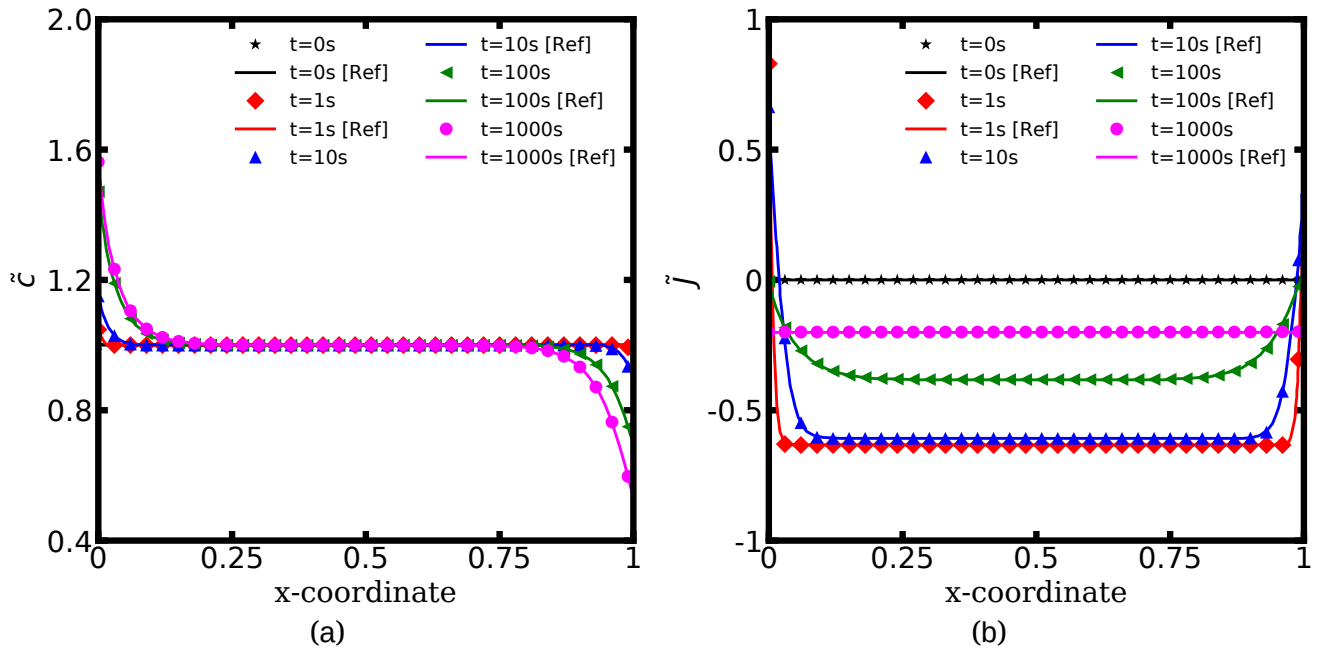


FIGURE 4.2 Potentiostatic condition with the voltage $\tilde{\Phi} = 2.696$ (a) dimensionless concentration \tilde{c} and (b) flux \tilde{J} profiles in the electrolyte.

The numerical concentration of lithium-ions and electrons at the cathode/electrolyte interface can be read as $\tilde{c}_i \approx 6$, which exceeds the maximum value $\tilde{c}_i = 1$ in the real material. The underlying reason of this phenomenon is the vacancy effect in solids. Lithium-ions migration is determined simultaneously by the diffusion coefficient and the available lattice sites in solids. However, the vacancy limitation has been ignored in the standard PNP model and the migration rate is much higher than the reality. Consequently, lithium-ions easily exceed the maximum concentration near the interface region. In contrast, lithium-ions could transfer in solids only when the bulk vacancy sites are available in the MPNP model, so the concentration is well constrained as expected. From the discussion, it can be concluded that the MPNP model is more physical than the standard PNP model in exploring the interface behaviours of ASSBs or the high-concentration region.

Fig. 4.3 shows the concentration profiles of the MPNP model with the different interface conditions. In the legend, the “WO/ c_v ” represents the FBV interface condition without the vacancy effect, as shown in Eq. (4.13). Instead, the “W/ c_v ” indicates that the vacancy effect has been included in the reaction, as given in Eq. (4.8). When the vacancy effect has been included in the interface reaction, less lithium-ions and electrons accumulate at the cathode/electrolyte interface. Results show that the vacancies at the interface constrain the amount of lithium-ions, which participate in the charge transfer reaction. As shown in Fig. 4.3f, it can be observed that the interface vacancies play an important role in the electrostatic potential distribution at the intrinsic equilibrium state. Moreover, the total electrostatic potential drops of these two cases are

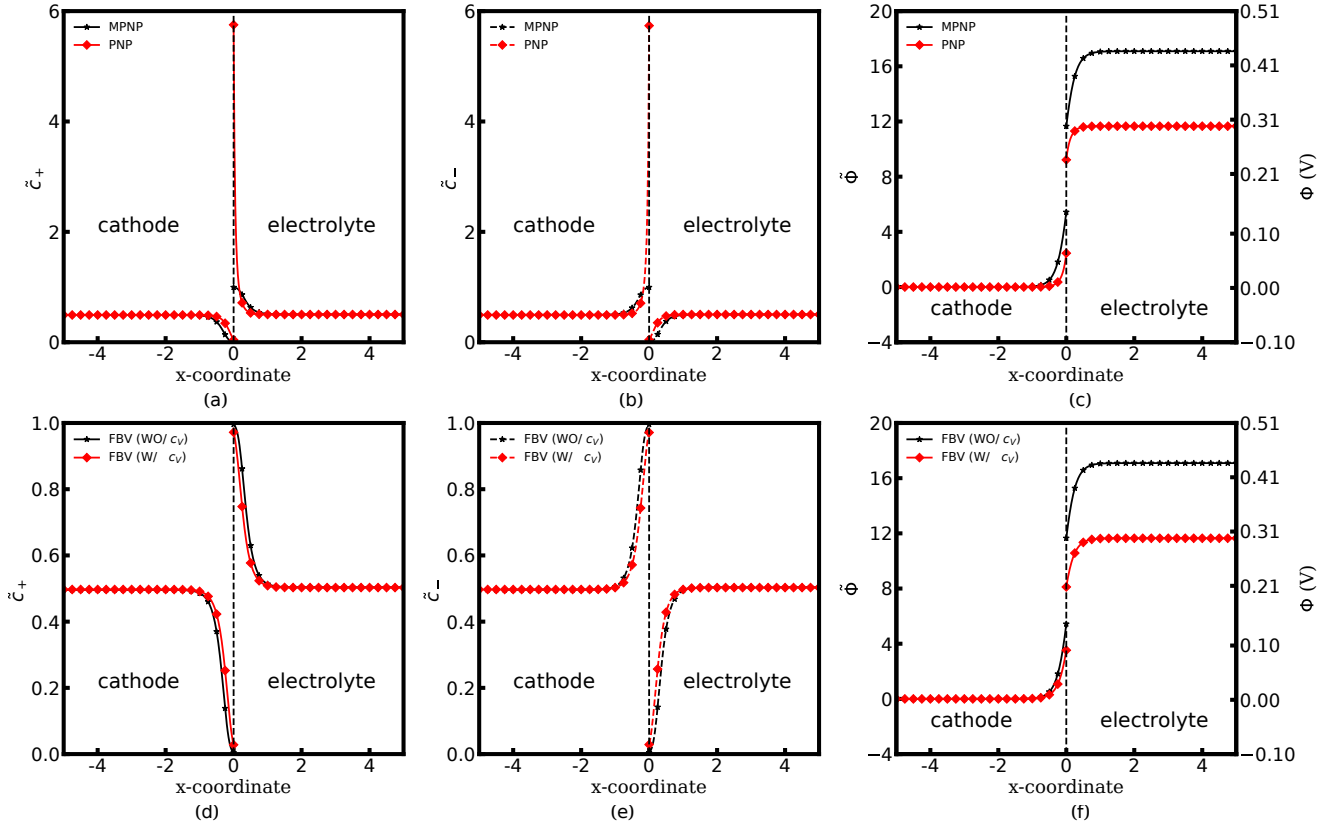


FIGURE 4.3 (a, d), (b, e) Concentration of lithium-ions \tilde{c}_+ and electrons \tilde{c}_- , and (c, f) electrochemical potential $\tilde{\Phi}$ profiles at the equilibrium state with different models and interface conditions.

$\Delta\Phi_{total} = \Phi_c - \Phi_e = -0.3$ and -0.44 V, respectively. From the chemical perspective, the value of the total electrostatic potential drop $|\Delta\Phi_{total}|$ is expected to be equal to the free enthalpy difference $\Delta G = G_c - G_e$ between the cathode and the electrolyte, i.e., $|\Delta\Phi_{total}| = \Delta G$. The molar free enthalpy G_i is determined by the standard free enthalpy and concentration, therefore, is described by

$$G_i = G_i^\ominus + RT \ln \frac{x_i}{1 - x_i} + z_i F \Phi \quad (4.14)$$

Before two materials contact with each other, the electrostatic potential equals zero, i.e., $\Phi = 0$, and can be ignored in Eq. (4.14). Hence, the actual free enthalpy difference yields

$$\Delta G = G_c^\ominus + RT \ln \frac{\tilde{c}_c}{1 - \tilde{c}_c} - G_e^\ominus - RT \ln \frac{\tilde{c}_e}{1 - \tilde{c}_e} \quad (4.15)$$

As shown in Fig. 4.1, the standard activation energy difference is numerically equals to the standard free enthalpy difference and is given by $\Delta G_e^\ominus - \Delta G_c^\ominus = G_c^\ominus - G_e^\ominus$. Additionally, the initial concentrations of the cathode and the solid-state electrolyte are $\tilde{c}_c = \tilde{c}_e = 0.5$, as shown in Tab. 4.1. Thus, the actual free enthalpy difference is $\Delta G = 0.3$ eV and the total electrostatic potential drop is $\Delta\Phi_{total} = -0.3$ V. Fig. 4.3c shows that when the vacancy effect has been ignored

in solids, the electrostatic potential drop is numerically equals to the free enthalpy difference, i.e., $|\Delta\Phi_{total}| = \Delta G$. Nevertheless, the concentration distribution in the space charge layer is unphysical within the PNP-FBV model, as shown in Figs. 4.3a and 4.3b. To compare Figs. 4.3c and 4.3f, it can be concluded that the advanced MPNP-FBV model which considers the vacancy sites effect both in the bulk and at the interface is more physical and rational from the chemical point of view.

4.3 Intrinsic Equilibrium State

In this section, the advanced MPNP-FBV model is applied to investigate the intrinsic equilibrium state of ASSBs. To check its consistency with the interface experimental results [90, 133, 134, 138], the LiCoO₂/LiPON thin film battery is considered. LiPON is an amorphous solid electrolyte without clearly defined lithium-ion sites, which should not affect the results significantly, however. The initial dimensionless concentrations of LiCoO₂ and LiPON are $\tilde{c}_c = \tilde{c}_e = 0.5$, and the thickness of Stern layer $\lambda_s = 0.3$ nm as well. The standard free enthalpy difference in our simulation is $\Delta G = 0.3$ eV and this input parameter is deduced from the difference in electronic work functions between LiCoO₂ and LiPON [90, 133, 138].

Figs. 4.4a and 4.4b show lithium-ions and electrons accumulate near the interface region with different time steps. Thus, the space charge layer is built up and the length is approximately 1 nm. This phenomenon has also been observed in the LiCoO₂/LiPON interface experiments [90]. The inserted graphs in Figs. 4.4a and 4.4b are the equilibrium concentrations near two boundaries. The concentrations of electrons and lithium-ions in the cathode and the electrolyte bulk are $\tilde{c}_c \approx 0.497$ and $\tilde{c}_e \approx 0.503$, respectively. Results show that no charge separation and the electrostatic potential gradient in the bulk. As depicted in Fig. 4.4c, the electrostatic potential difference at $x = 0$ is the electrostatic potential drop across the Stern layer, which is the driving force $\Delta\Phi_s = \Phi_c - \Phi_e$ in Eq. (4.8). The driving force compensates the free enthalpy difference and alters the overall kinetic flux, so $\Delta\Phi_s$ increases with time steps until the system reaches the intrinsic equilibrium state and the total electrostatic potential drop is $\Delta\Phi_{total} = -0.3$ V. In the previous investigations [90, 133], the electrostatic potential gradient at the LiCoO₂/LiPON interface is measured using x-ray photoelectron spectroscopy and the value is -0.3 V. Lithium-ions transfer to the electrolyte during the charge transfer reaction, the cathode shows a negative polarity, while the electrolyte with a positive polarization.

The comparable electrochemical potential profiles at different time steps are shown in Fig. 4.4e. In the MPNP-FBV model, the dimensionless electrochemical potential $\tilde{\mu}_i$ for the component i is given by Eq. (4.1). The standard activation energies of LiCoO₂ and LiPON are assumed to be $\Delta G_c^\ominus = 0.5$ eV and $\Delta G_e^\ominus = 0.8$ eV in Tab. 4.1. Before the cathode and the electrolyte get into contact with each other, the dimensionless initial concentrations are $\tilde{c}_c = \tilde{c}_e = 0.5$ and the

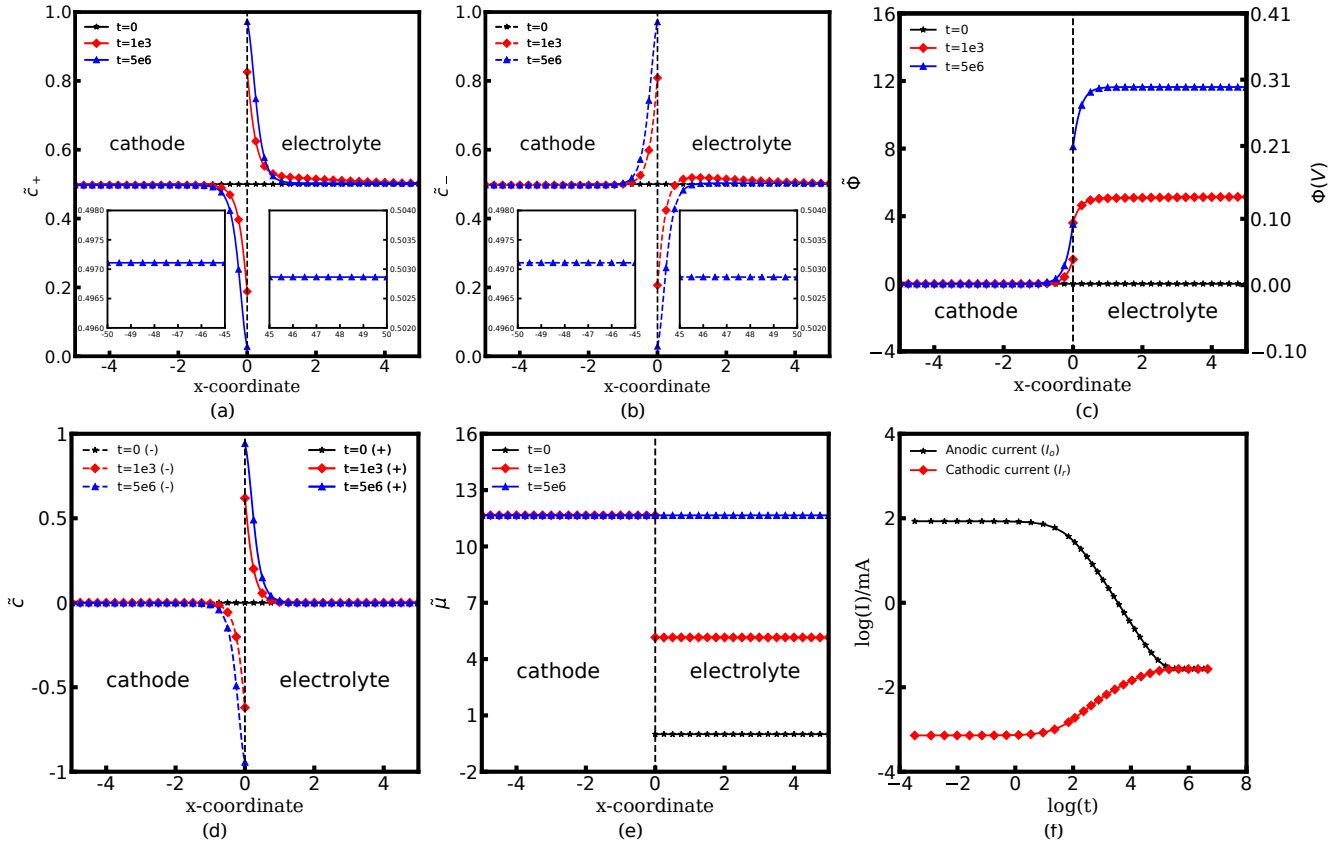


FIGURE 4.4 (a), (b) Concentration of lithium-ions \tilde{c}_+ and electrons \tilde{c}_- , (c) electrostatic potential $\tilde{\Phi}$, (d) charge density \tilde{c} , (e) electrochemical potential $\tilde{\mu}$ profiles at the equilibrium state with different initial $\tilde{\Phi}$.

electrostatic potentials are $\Phi_c = \Phi_e = 0$. Assuming the standard molar free enthalpy of the electrolyte is the reference state, i.e., $G_e^\ominus = 0$ eV, which indicates the standard free enthalpy of the cathode is $G_c^\ominus = 0.3$ eV. The dimensionless electrochemical potential is defined as $\tilde{\mu}_i = \mu_i/RT$, so $\tilde{\mu}_c = 11.68$ and $\tilde{\mu}_e = 0$ at the initial state in Fig. 4.4e. During the reaction, lithium-ions move from the cathode to the neighbouring electrolyte, which increases the electrostatic potential difference $\Delta\Phi$. Due to the concentration and the electrostatic potential variation in the cathode and the electrolyte, the system reaches the intrinsic equilibrium state $\tilde{\mu}_c = \tilde{\mu}_e$ eventually. Fig. 4.4f shows the time evolution of the reaction current, and it represents lithium-ion flux at the interface. The anodic current is denoted by I_c and the cathodic current is expressed as I_e , respectively. The anodic current is larger than the cathodic current at the beginning of the charge transfer reaction, and this is caused by the activation energy difference $\Delta G_c < \Delta G_e$. The net current shows that more lithium-ions transfer to the electrolyte due to the reaction and this is consistent with the concentration distribution in Fig. 4.4a. Finally, the anodic current I_c equals to the cathodic current I_e , and the net current is $I_0 = I_c - I_e = 0$. The magnitude of this current is called the exchange current and is widely applied in battery modelling. The exchange current is a given value in

widely applied electrochemical models, and the chosen values are uncertain. Therefore, our work takes a further step and calculates the exchange current from more fundamental material and interface properties, e.g., the two free enthalpies and their difference. Moreover, the numerical results at the equilibrium state are verified by the experimental data [90], indicating that the calculated the exchange current is physical.

4.4 Influence of Initial Concentrations

In this section, we will study the intrinsic equilibrium state of ASSBs with the different interface structures, e.g., the Gouy-Champan-Stern model (the diffuse double layer model) and the Helmholtz model (the compact double layer model), as depicted in Fig. 2.2. Therefore, the electrostatic potential, the exchange current and the charge transfer resistance are discussed with the different EDL structures. To have more specific research about the interface reaction, the cathode with different concentrations are discussed. While the initial concentration in solid-state electrolyte is fixed at $\tilde{c}_e = 0.5$, the initial concentration \tilde{c}_c in the cathode varies from 0.1 to 0.9, where 0.1 and 0.9 represent theoretical state of charge (SOC) 10 % and 90 %, respectively.

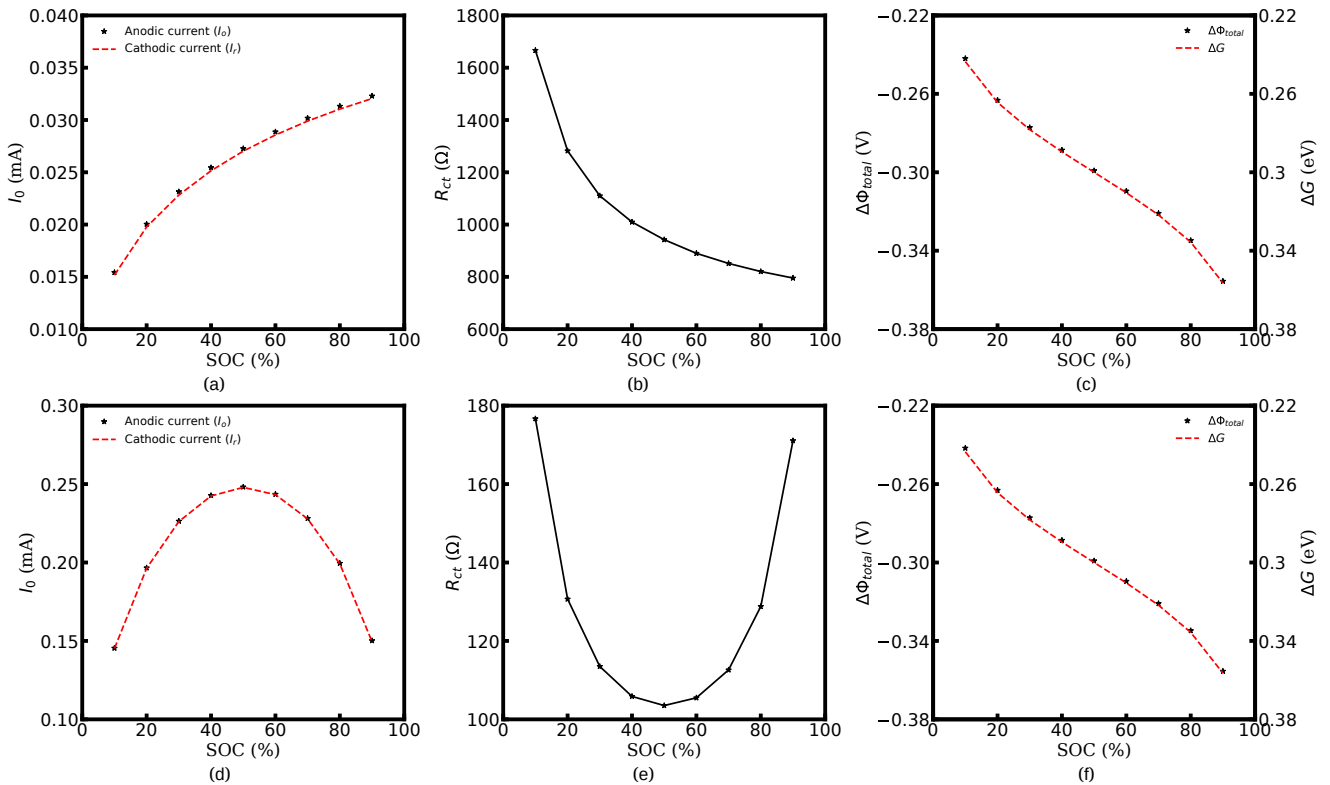


FIGURE 4.5 (a), (d) Exchange current I_0 , (b), (e) charge transfer resistance R_{ct} and (c), (f) total electrostatic potential drop $\Delta\Phi$ at equilibrium state with different initial concentrations in cathode

Fig. 4.5 shows the exchange current I_0 , the charge transfer resistance R_{ct} , and the total electrostatic potential drop $\Delta\Phi_{total}$ with different initial concentrations in the cathode. It can be concluded that the total potential drop $\Delta\Phi_{total}$ is determined by the concentration and is consistent with Eq. (4.15), while the I_0 and R_{ct} are affected by the interface structure. Comparing Fig. 4.5a and Fig. 4.5d, the exchange current value is much smaller when the diffuse double layer has been considered. Without the space charge layer, the exchange current increases with the low SOC and decreases with the high SOC, the maximum current is $I_0 \approx 0.25$ mA at 50 % SOC, as shown in Fig. 4.5d. When the electrostatic potential drops in the diffuse layer, the exchange current increases with the cathode concentration increasing and is $I_0 \approx 0.027$ mA at 50 % SOC, as depicted in Fig. 4.5a. The charge transfer resistance R_{ct} is inversely proportional to the exchange current and is expressed as $R_{ct} = RT/FI_0$. From Fig. 4.5b, it can be observed that the charge transfer resistance R_{ct} is one order of magnitude larger compared to Fig. 4.5e. Results indicate that the interface with the diffuse double layer has a great unfavourable effect on the battery impedance. According to the experimental results [139], the charge transfer resistance of the LiCoO₂/LiPON interface is also around 1000 Ω . Furthermore, Fig. 4.5b shows that the charge transfer resistance decreases with lithium-ion concentration increasing and this phenomenon is also observed by Shalini and Ardani [140, 141]. The trend of the measurement charge transfer resistance curve is similar to our numerical results. This conclusion also indicates that the presence of a diffuse double layer structure at the solid-solid interface.

The total electrostatic potential drop $\Delta\Phi_{total}$ and the free enthalpy difference of materials ΔG are presented in Figs. 4.5c and 4.5f. It can be observed that these two figures are identical and the total electrostatic potential drop is coherent with the free enthalpy difference at different SOC states. The free enthalpy difference ΔG between the cathode and the electrolyte is presented by Eq. (4.15), and is equal to the absolute value of the total electrostatic potential drop $\Delta\Phi_{total}$ at the equilibrium state. Moreover, the variation of $\Delta\Phi_{total}^\dagger - \Delta\Phi_{total}^\ddagger$ is also related to the concentration change, which \dagger and \ddagger represent the former and later states

$$\Delta\Phi_{total}^\dagger - \Delta\Phi_{total}^\ddagger = \frac{RT}{F} \ln \frac{\tilde{c}_{Li,(c)}^\ddagger \left[1 - \tilde{c}_{Li,(c)}^\dagger \right]}{\tilde{c}_{Li,(c)}^\dagger \left[1 - \tilde{c}_{Li,(c)}^\ddagger \right]}. \quad (4.16)$$

In Figs. 4.5c and 4.5f, the total electrostatic potential drops are $\Delta\Phi_{total}^\dagger = -0.243$ V when the SOC is 10 % and $\Delta\Phi_{total}^\ddagger = -0.356$ V after the SOC increases to 90 %. The total electrostatic potential drop change is -0.113 V and equals to the value calculated from Eq. (4.16). The electrochemical potential change coincides well with the reference [142].

Moreover, the space charge layer thickness is associated with the Debye length and is given by

$$\lambda_D = \sqrt{\frac{RT\varepsilon_i\varepsilon_0}{F^2 \sum z_i^2 c_i}}, \quad (4.17)$$

It can be concluded that the thickness of the space charge layer increases with the concentration decreasing. To clarify this phenomenon, the initial concentrations in both the cathode and the electrolyte are changed and are given by $\tilde{c}_c = \tilde{c}_e = 0.05, 0.1, 0.5$, respectively. The thickness of the Stern layer remains the same $\lambda_s = 0.3$ nm in all cases.

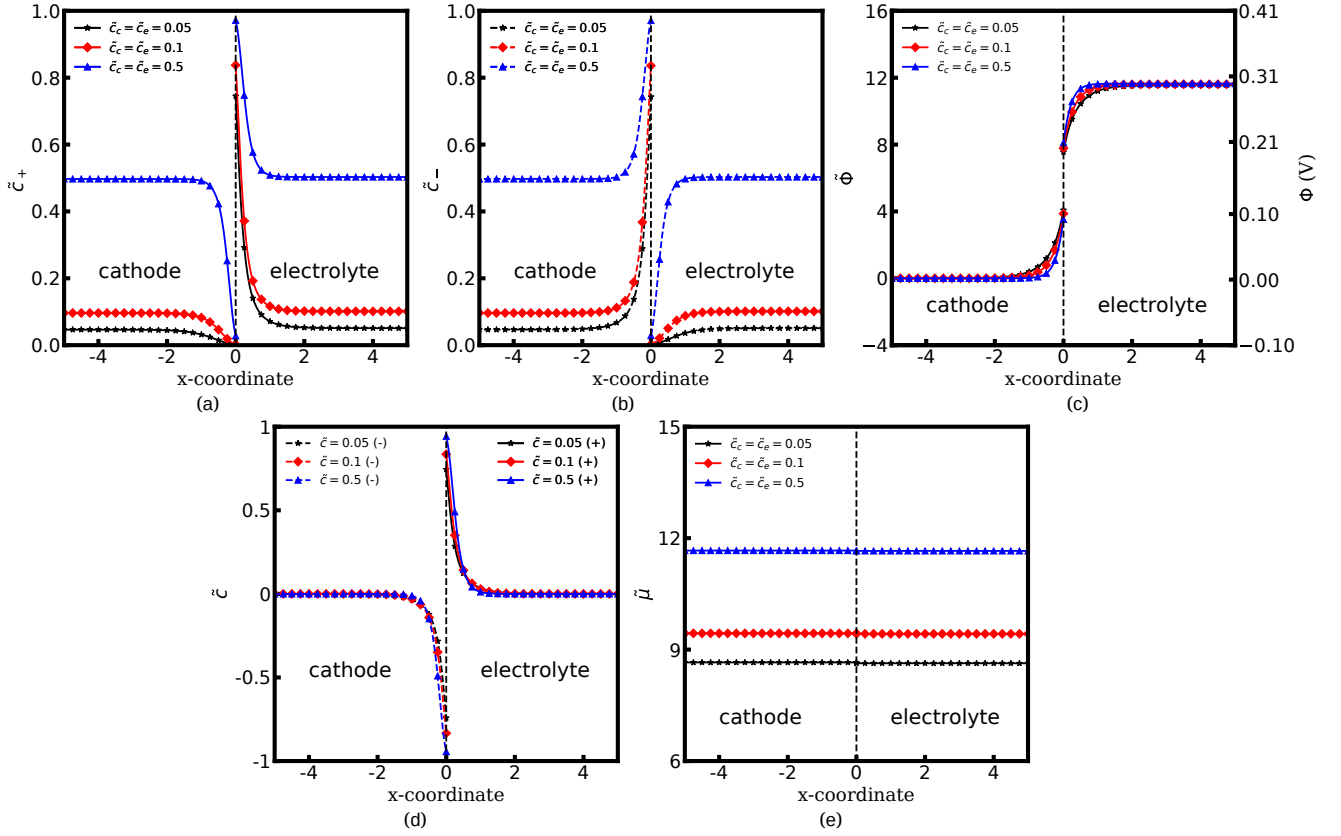


FIGURE 4.6 (a), (b) Concentration of lithium-ions \tilde{c}_+ and electrons \tilde{c}_- , (c) electrostatic potential $\tilde{\Phi}$, (d) charge density \tilde{c} , (e) electrochemical potential $\tilde{\mu}$ profiles at the equilibrium state with different initial concentration

Fig. 4.6 illustrates the intrinsic equilibrium state with the different initial concentrations in the cathode and the electrolyte. As shown in Fig. 4.6c, the total electrostatic potential drop $\Delta\Phi_{total}$ remains a constant value when the initial concentration changes. This phenomenon can be explained by Eq. (4.15), the free enthalpy difference ΔG is determined by the cathode and the electrolyte concentrations simultaneously. Recalling Eq. (4.17), the Debye length is associated with material properties and is inversely proportional to the initial concentration. This phenomenon can also be observed in Fig. 4.6c, and the thickness of the space charge layer with a lower initial concentration is larger than that in the case with a higher concentration. Fig. 4.6d presents the charge density at the equilibrium state with the different concentrations in the half cell, and it can be seen that the charges maintain electrical neutrality. From these results, we can conclude that the MPNP-FBV model is physical and is able to analyse the interface behaviours at

the intrinsic equilibrium state with considering the reaction.

4.5 Influence of Diffusivity

Electron migration in the electrolyte plays an major role in the cell performance and this factor has been extensively discussed in battery modelling. To investigate the influence of electrons on the intrinsic equilibrium state of ASSBs, the electrolyte with different electronic conductivities are discussed in this section. In practical, the migration of electrons in the electrolyte is more important than that in the cathode. Therefore, electrolytes with mobile, i.e., $D_{e,-} = 10^{-15} \text{ m}^2 \text{ s}^{-1}$, and immobile electrons, i.e., $D_{e,-} = 0$, have been discussed here. Other parameters are given in Tab. 4.1.

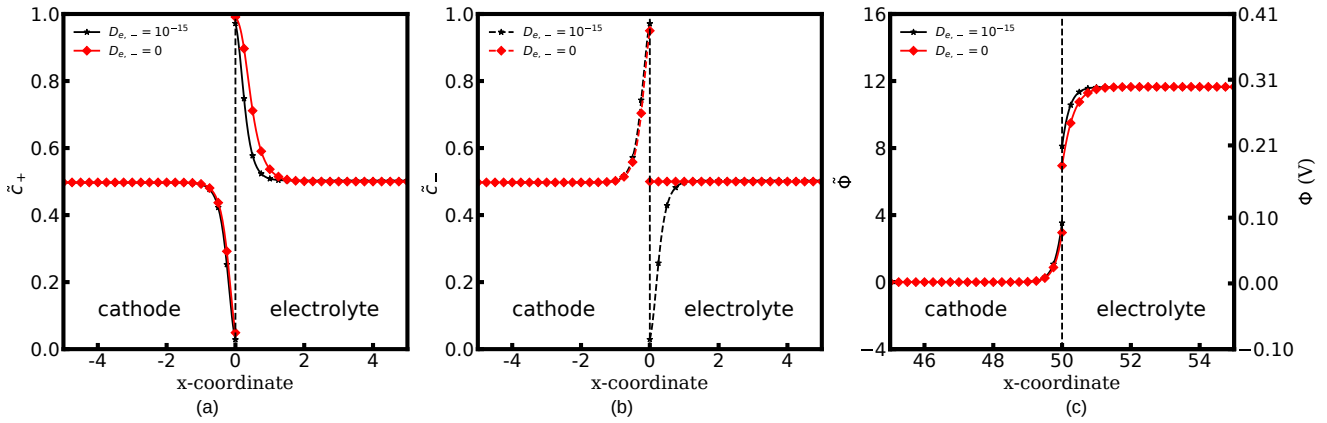


FIGURE 4.7 (a), Concentration of lithium ions \tilde{c}_+ , (b) electrons \tilde{c}_- , (c) electrostatic potential $\tilde{\Phi}$ profiles at the equilibrium state with different diffusivities in the electrolyte

Figs. 4.7a to 4.7c show the species concentration and the electrostatic potential distributions at the intrinsic equilibrium state with mobile and immobile electrons in the solid-state electrolyte. It can be observed that immobile electrons have a great influence on the concentration distribution. When electrons are immobile, more lithium ions accumulate in the space charge layer as shown in Figs. 4.7a. Moreover, Figs. 4.7c shows that the electrostatic potential distribution profiles are different, while the total electrostatic potential drop in these two cases are the same and is $\Delta\Phi_{total} = -0.3 \text{ V}$. Results show that the diffusivity of electron plays an important role in the charge density in the space charge layer, therefore, affects the exchange current and the charge transfer resistance. Nevertheless, the total electrostatic potential drop $\Delta\Phi_{total}$ is not influenced by this factor.

4.6 Summary

In this chapter, we propose an advanced MPNP-FBV model for ASSBs and study the interface behaviours at the intrinsic equilibrium state in detail. In the MPNP-FBV model, the vacancies at the interface and in the bulk have been taken into consideration. Moreover, the migration of electrons and the electrical double layer structure are fully incorporated into lithium-ion reaction at the cathode/electrolyte interface. Verified by the chemical perspective and the interface experimental results, this advanced MPNP-FBV model is able to explain the intrinsic equilibrium state of ASSBs. Consequently, the exchange current, the concentration and the electrostatic potential distributions in the space charge layer can be calculated based on the MPNP-FBV model.

Numerical results demonstrate that the vacancy effect has a great influence on lithium-ions distribution in the space charge layer and the total electrostatic potential drop at the intrinsic equilibrium state. Furthermore, the concentration and the electrostatic potential distributions at the interface are extensively affected by the different EDL structures. Lithium-ions and electrons build up at the interface show the obvious double layer effect over time going when the diffuse double layer model is applied. Nevertheless, with the compact double layer model, there is no formation of the space charge layer at the interface. Therefore, the EDL structure plays an important role in the exchange current and the charge transfer resistance. The exchange current of ASSBs with the space charge layer is much smaller than that without the space charge layer, while the charge transfer resistance is larger. Although the distribution of the electrostatic potential changes with the different EDL structures, the total potential drop is identical and is equal to the free enthalpy difference between the two materials. Thereafter, the exchange current and the total electrostatic potential drop at the equilibrium state have been studied with the different concentrations and diffusivities.

This work shows that the exchange current, the charge transfer resistance and the space charge layer of ASSBs can be calculated and investigated by the MPNP-FBV model. Moreover, this model is also extended to calculate the interface impedance of batteries based on material properties, as shown in Chap. 6.

5 Impedance of Solid-State Electrolytes: Influence of the Contacted Space Charge Layer

Noted that this chapter is based on the publication “Y. Liu, Y. Bai, W. Jaegermann, R. Hausbrand, and B.-X. Xu, *ACS Applied Materials & Interfaces*, 13, 5895–5906 (2021)”.

The advanced electrochemical MPNP-FBV model for ASSBs has been presented in Chap. 4, and the concentration and the electrostatic potential distributions at the interface are well estimated. From the numerical results, it can be observed that the accumulation of charges or exhaustion leads to a drastic decrease of the electrostatic potential in the space charge layer. Therefore, the solid/solid interface always obtains a high interface impedance in comparison to the liquid/solid interface, and this is an inevitable bottleneck for the development of ASSBs [75]. Currently, the explanation of the space charge layer impedance is still controversy [57, 78–81].

As shown in Chap. 3, the space charge layer is regarded as a pure capacitor. Nevertheless, this assumption fails to explain the experimental impedance spectroscopy tail at low frequencies [105, 107]. The capacitance is determined by the charge density Q and the electric field E , and is defined as $C = -\partial Q/\partial\Phi$. In practical, an electrostatic disturbance potential has been employed for the measurement of battery impedance. Therefore, the charge density in the space charge layer is frequency-dependent and an additional impedance is expected to be associated with this effect. Nevertheless, less attention has been devoted to investigate this factor in the space charge layer. To shed light on this obstacle, we take the example of an ideally blocking solid-state electrolyte and propose a new equivalent circuit model to strength the understanding of the space charge layer impedance in this work.

Due to the advantage in particular in the study of interface behaviours, the MPNP model presented in Chap. 4 has been employed here to investigate the space charge layer impedance. Based on the MPNP model, a more accurate analytical solution for the space charge layer capacitance is proposed. Thereafter, we take a further step and propose a new frequency-dependent space charge layer resistance for the first time. Elements in the corresponding equivalent circuit model are well interpreted and closely related to material properties. The structure of this chapter is

organized as follows: In Sec. 5.1, the impedance models and the set of equations are introduced. Secs. 5.2 and 5.3 describes the corresponding physical results such as the analytical space charge layer capacitance, the space charge layer resistance and the chemical capacitance. Here, we introduce the equivalent circuit model and the comparison of numerical and experimental results. A summary of our work and an outlook are shown in Sec. 5.4.

5.1 Solid-State Electrolytes Impedance Modelling

In this work, we study a metal/electrolyte/metal cell consisting of a solid-state electrolyte and a pair of electrodes, as shown in Fig. 5.1. In order to verify our impedance model and the numerical results with the experimental data [105, 107], the amorphous material LiPON is considered as the solid-state electrolyte with a thickness L_e and the electrochemically inert metal Pt is chosen as the electrode. With an external disturbance, charges accumulate at the metal/electrolyte interface and form the space charge layer as shown in Fig. 5.1a [89, 90, 92]. Moreover, the Stern layer near to the space charge layer is ignored in order to reduce the influence factors and simplify the consideration.

5.1.1 Equivalent Circuit Model

Fig. 5.1b illustrates the proposed equivalent circuit model for the metal/electrolyte/metal cell configuration, each element of which will be directly correlated to the solid-state electrolyte material properties. According to the investigations [106, 108, 143], electrons can move with a relative low velocity in solid-state electrolytes at room temperature, thus, the contributions of electrons are also included in the corresponding equivalent circuit model to maintain the generality. Elements related to lithium-ions are indicated by the subscript “+”, while electrons are denoted by “-”. The quantities R_e^{bu} and C_e^{bu} refer to solid-state electrolytes bulk resistance and dielectric capacitance contributed by ions and electrons, respectively.

The charge accumulation at the metal/electrolyte interface contributes to the space charge layer impedance Z_e^{in} , thus the impedance is proportional to the charge density Q . Note that the superscript “in” denotes the interface, and “bu” indicates the bulk, respectively. To simplify the discussion, we consider only the space charge layer impedance $Z_e^{in}(L)$ at the left-hand side, while the right-hand space charge layer impedance is $Z_e^{in}(R) = 0$ and has been ignored [94, 111], as depicted in Fig. 5.1a. It should be pointed out that “(L)” indicates the left-hand side, and “(R)” is the right-hand side, respectively. This simplification corresponds to the case of an infinite solid-state electrolyte thickness and is reasonable when the space charge layer is much smaller than the electrolyte ($L_s \ll L_e$). Note that a similar impedance analysis can be applied to the right-hand electrolyte interface if it is included. From a thermodynamic point of

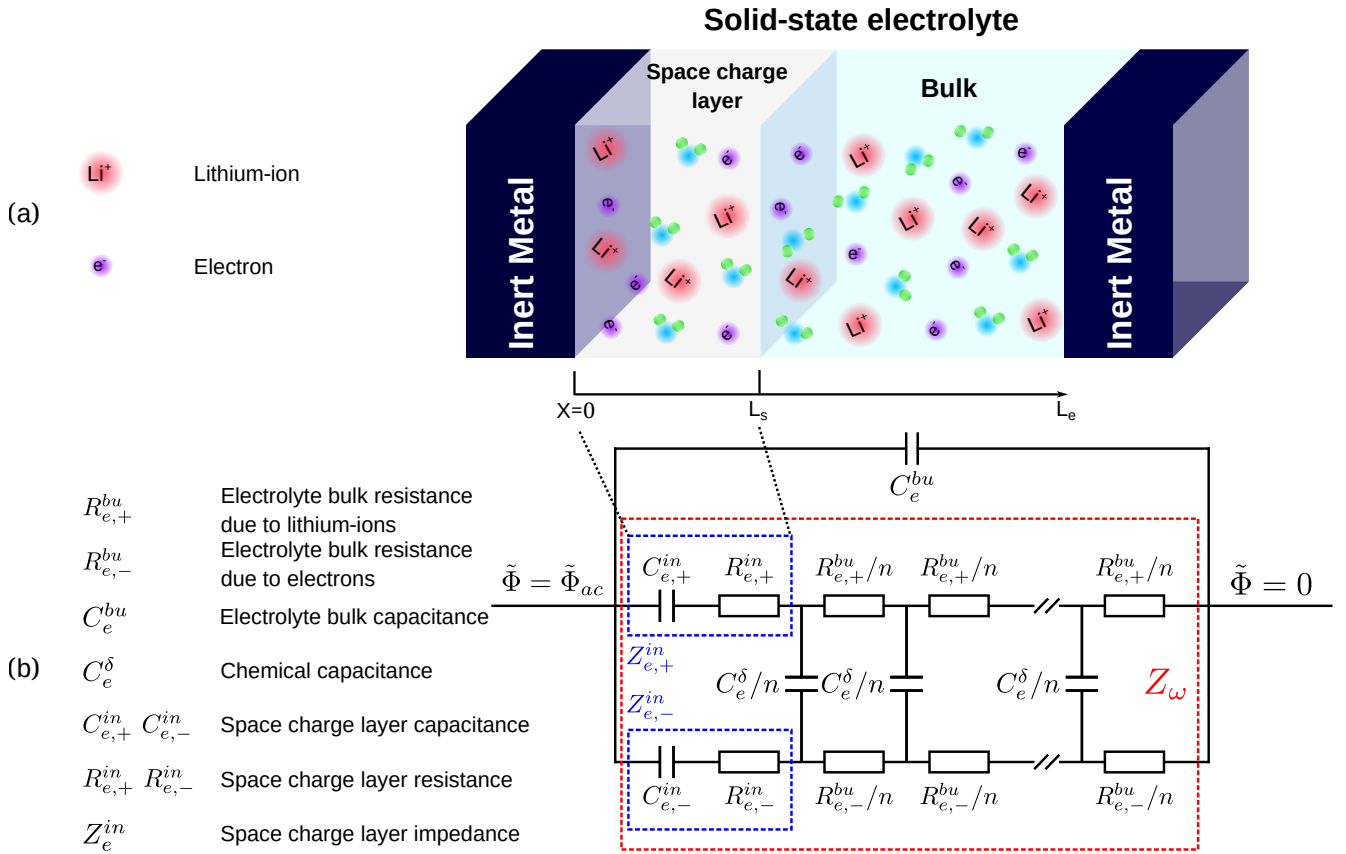


FIGURE 5.1 (a) The schematic of a metal/electrolyte/metal cell with the space charge layer at the interface, and (b) the proposed equivalent circuit model.

view, the chemical capacitor C_e^δ is purely non-electrostatic and is defined as second derivative of the Gibbs free energy with respect to the number of species. Thus, C_e^δ is given by the changes of the component chemical potential μ_i^* due to the concentration c_i variations [109, 113]. In solid-state electrolytes, the stoichiometry effect varies significantly when the density of vacancies are included. Moreover, the C_e^δ is proportional to the material volume and can be very large compared to the electrolyte bulk capacitance C_e^{bu} . The chemical capacitance C_e^δ line can be omitted at high frequencies, thus, the transmission line Z_ω is simplified by the ionic line $R_{e,+}^{bu}$ in parallel with the electronic $R_{e,-}^{bu}$ line in some equivalent circuit models. Nevertheless, the chemical capacitance C_e^δ cannot be ignored at low frequencies. The space charge layer impedance Z_i is simply assumed as an ideal capacitor [105, 111, 112], nevertheless, Macdonald [144] pointed out that the space charge layer impedance Z_e^{in} follows the relation $Z_e^{in} = (j\omega C_e^{in})^{-1} + R_e^{in}$. It should be noted that the space charge layer impedance Z_e^{in} is proportional to the charge density, and the capacitor C_e^{in} and the resistance R_e^{in} are frequency-dependent. The results of capacitor and resistance can only be resolved numerically and fail to correlate with material properties. Thereby, researchers prone to calculate the values at the equilibrium state and simplify the explanation.

We can note that this simplification ignores the frequency perturbation, thus it fails to explain the experimental spectroscopies, as presented in [105, 107]. Therefore, in this work, we propose the new frequency-dependent space charge layer resistance and hope to solve this problem.

5.1.2 Electrochemical Model

Referring to Chap. 3, the concentration distribution in the space charge layer of solid-state electrolytes has a large impact on the impedance spectroscopy. Therefore, the precise prediction of the charge accumulation in the space charge layer is particularly crucial and deserves a careful discussion. Due to the benefit of studying the space charge layer, the MPNP model is applied in our work and the equations are expressed as.

$$\frac{\partial c_i}{\partial t} = -\nabla \cdot J_i \quad J_i = -\frac{D_i}{1 - \tilde{c}_i} \nabla c_i - z_i \frac{FD_i}{RT} c_i \nabla \Phi, \quad (5.1)$$

$$\nabla^2 \Phi = -\frac{F}{\varepsilon_0 \varepsilon_i} (z_+ c_+ + z_- c_- - z \rho). \quad (5.2)$$

The symbol ρ denotes the immobile charge, z_i is the valence of the species i , and z is equal to $z = |z_i|$. As illustrated in Fig. 6.1a, the solid-state electrolyte operates with a pulse electric potential condition and formulates $\Phi = \Phi_{dc} + \Phi_{ac}(\cos \omega t + j \sin \omega t)$, where Φ_{dc} and Φ_{ac} denote the direct current (dc) and the alternating current (ac) potentials, respectively. The resulting current should have the same type structure and is expressed as $I = I_{dc} + I_{ac}[\cos(\omega - \omega_0)t + j \sin(\omega - \omega_0)t]$, where ω_0 is the phase angle difference. Therefore, the impedance Z is expressed as [94, 95]

$$Z = \frac{\Phi_{ac}(\cos \omega t + j \sin \omega t)}{I_{ac}[\cos(\omega - \omega_0)t + j \sin(\omega - \omega_0)t]} = Z_{re} + j \cdot Z_{im}, \quad (5.3)$$

Z_{re} and Z_{im} are the real and imaginary parts of the complete impedance of batteries, respectively. Note that the numerical methodology for the impedance calculation can refer to Chap. 3.

To simplify the discussion and ensure the impedance simulation more mathematically tractable, several assumptions and boundary conditions follow the literature and are applied [94, 111]. (1) The metal/electrolyte/metal cell is considered as one-dimensional domain and operated with an alternating current (ac) potential perturbation in the frequency range. (2) The electrostatic potential drop and the species migration in the inert metal are ignored, thus the boundary conditions for the solid-state electrolyte are $\Phi_e(L) = \Phi_{dc} + \Phi_{ac}(\cos \omega t + j \sin \omega t)$ and $\Phi_e(R) = 0$. (3) Lithium-ions and electrons in the solid-state electrolyte are completely blocked at the left-hand side. Therefore, the boundary conditions of the species concentrations are $J_{e,+}(L) = 0$ and $J_{e,-}(L) = 0$. (4) The behaviours at the right-hand side of the solid-state electrolyte is regarded as infinite length behaviours, no charge separation and space charge layer formation at the right-hand side and the concentrations are $c_{e,+}(R) = c$ and $c_{e,+}(L) = c$. (5) No lithium-ion intercalation happens and no contact resistance occurs at the metal/electrolyte interface.

5.2 Impedance Simulation of Solid-State Electrolytes

The simulated electrochemical impedance spectroscopy and the corresponding material properties quantification are presented in this section. In Sec. 5.2.1, the analytical space charge layer capacitance caused by the charge accumulation is proposed. Then, the space charge layer impedance compositions and the corresponding equivalent circuit model are discussed in detail. Similar to Chap. 4, the numerical simulation has been performed with the finite element method in the MOOSE framework [145]. All the parameters applied in the impedance simulation are derived from the experimental research of LiPON thin film [146, 147] and are shown in Tab. 5.1.

Parameter	Unit	Value	Description
L_e	nm	100	Thickness of the electrolyte
$D_{e,+}$	$\text{m}^2 \text{s}^{-1}$	10^{-14}	Diffusivity of Lithium ions in the electrolyte
$D_{e,-}$	$\text{m}^2 \text{s}^{-1}$	10^{-16}	Diffusivity of electrons in the electrolyte
ε_0	F m^{-1}	8.85×10^{-12}	Vacuum permittivity
ε_i	–	20	Relative permittivity
E_a	eV	0.5	Hopping energy in LiPON
σ_0	S m^{-1}	1.59×10^7	Pre-exponential factor
$\sigma_{e,+}$	S m^{-1}	1.88×10^{-4}	Ionic conductivity at 298.15 K
c_{max}	mol m^{-3}	10^4	Maximum concentration
$c_{e,+}$	mol m^{-3}	5×10^3	Initial mobile Lithium ions in the electrolyte
$c_{e,-}$	mol m^{-3}	5×10^3	Initial mobile electrons in the electrolyte
F	C mol^{-1}	96 485	Faraday constant
T	K	298.15	Temperature
R	$\text{J mol}^{-1} \text{K}^{-1}$	8.314	Gas constant
z_+	--	1	Lithium ion valence
z_-	--	-1	Electron valence
A	m^2	4×10^{-6}	Geometrical surface area

TABLE 5.1 The solid-state electrolyte parameters

5.2.1 Analytical Capacitance of the Space Charge Layer

The space charge layer capacitance C_e^{in} is a critical factor in the interface impedance analysis, thus researchers hope to derive an analytical solution of the capacitance and to correlate with material properties. Different analytical solutions of the space charge layer capacitance have been presented in Sec. 3.2.2, however, these predicted values are derived from the standard PNP model

and shows a discrepancy with solid materials. Thus, an accurate theoretical space charge layer capacitance based on the MPNP model is introduced in this section. In the standard PNP model, the concentration distribution in the space charge layer at the equilibrium state is related to the electrostatic potential by the Boltzmann distribution [72] and is given by

$$c_{e,i} = c_{e,i}^{bu} \exp\left(\frac{-z_i F \Phi_e^{bu}}{RT}\right), \quad (5.4)$$

where $c_{e,i}^{bu}$ is the bulk concentration of species i ($i = +$ or $-$) in electrolytes. Due to a limited amount of vacancies in the space charge layer, Eq. (5.4) fails to describe the concentration distribution in solid electrolytes and the new formula is expressed by the modified Boltzmann distribution

$$c_{e,i} = \frac{c_{e,i}^{bu} e^{-z_i F \Phi_e^{bu}/RT}}{1 + \tilde{c}_{e,i}^{bu} (e^{-z_i F \Phi_e^{bu}/RT} - 1)}, \quad (5.5)$$

and $\tilde{c}_{e,i}^{bu}$ is the dimensionless concentration. For general consideration, the total concentrations of mobile lithium-ions and electrons are not necessarily the same in solid-state electrolytes. The Poisson equation is given in the following with ρ being the charge of immobile species $\rho = c_{e,+} - c_{e,-}$ and z_i the valence, and $z = |z_i|$:

$$\begin{aligned} \nabla^2 \Phi &= -\frac{F}{\varepsilon_0 \varepsilon_i} (z_+ c_{e,+} + z_- c_{e,-} - z \rho) \\ &= -\frac{F}{\varepsilon_0 \varepsilon_i} \left[\frac{c_{e,+}^{bu} e^{-z F \Phi_e^{bu}/RT}}{1 + \tilde{c}_{e,+}^{bu} (e^{-z F \Phi_e^{bu}/RT} - 1)} - \frac{c_{e,-}^{bu} e^{z F \Phi_e^{bu}/RT}}{1 + \tilde{c}_{e,-}^{bu} (e^{z F \Phi_e^{bu}/RT} - 1)} - z \rho \right], \end{aligned} \quad (5.6)$$

and boundary conditions yield

$$\Phi_e(L) = \Phi_{dc} \quad \Phi_e(R) = 0 \quad \nabla \Phi_e(R) = 0. \quad (5.7)$$

This equation can be resolved and gives the electric field E

$$E = \sqrt{\frac{2RT c_{max}}{\varepsilon_0 \varepsilon_i} \left\{ \ln [1 + \tilde{c}_{e,+}^{bu} (e^{-z F \Phi_e^{bu}/RT} - 1)] + \ln [1 + \tilde{c}_{e,-}^{bu} (e^{z F \Phi_e^{bu}/RT} - 1)] \right\} + \frac{2F \Phi_e^{bu} \tilde{\rho} c_{max}}{\varepsilon_0 \varepsilon_i}}. \quad (5.8)$$

In Eq. (5.8), c_{max} is the maximum concentration of charges in the material. The analytical space charge layer capacitance C_e^{in} is defined by the charge density Q and the electrostatic potential Φ , and yields

$$C_e^{in} = -\frac{\partial Q}{\partial \Phi} = -\frac{\partial(-AE\varepsilon_0\varepsilon_i)}{\partial \Phi} = A\varepsilon_0\varepsilon_i \frac{\partial E}{\partial \Phi}. \quad (5.9)$$

Finally, we derive the analytical space charge layer capacitance of the solid-state electrolyte, which is expressed as

$$C_e^{in} = A \frac{F c_{max} \left[\frac{-z \tilde{c}_{e,+}^{bu} e^{-zF\Phi_e^{bu}/RT}}{1 + \tilde{c}_{e,+}^{bu} (e^{-zF\Phi_e^{bu}/RT} - 1)} + \frac{z \tilde{c}_{e,-}^{bu} e^{zF\Phi_e^{bu}/RT}}{1 + \tilde{c}_{e,-}^{bu} (e^{zF\Phi_e^{bu}/RT} - 1)} \right] + F \tilde{\rho} c_{max}}{\sqrt{\frac{2RT c_{max}}{\varepsilon_0 \varepsilon_i} \left\{ \ln [1 + \tilde{c}_{e,+}^{bu} (e^{-zF\Phi_e^{bu}/RT} - 1)] + \ln [1 + \tilde{c}_{e,-}^{bu} (e^{zF\Phi_e^{bu}/RT} - 1)] \right\} + \frac{2F\Phi_e^{bu} \tilde{\rho} c_{max}}{\varepsilon_0 \varepsilon_i}}} \quad (5.10)$$

To verify analytical solutions, we compare them with the numerical results calculated from the MPNP model. Different initial concentrations are considered in the solid-state electrolyte, in which mobile lithium-ions are $\tilde{c}_{e,+} = 0.5$ and electrons are $\tilde{c}_{e,-} = 0.1$ and 0.5 , respectively. The boundary conditions fulfil our assumptions and are expressed by $\tilde{J}_{e,+}(L) = \tilde{J}_{e,-}(L) = 0$ and $\tilde{c}_{e,+}(R) = 0.5$, $\tilde{c}_{e,-}(R) = 0.1, 0.5$. The metal/electrolyte/metal cell operates with the potentiostatic condition and the given values are $\tilde{\Phi}_e(L) = 0.01$ and $\tilde{\Phi}_e(L) = 0$. Other parameters applied in the simulation are given in the Tab. 5.1.

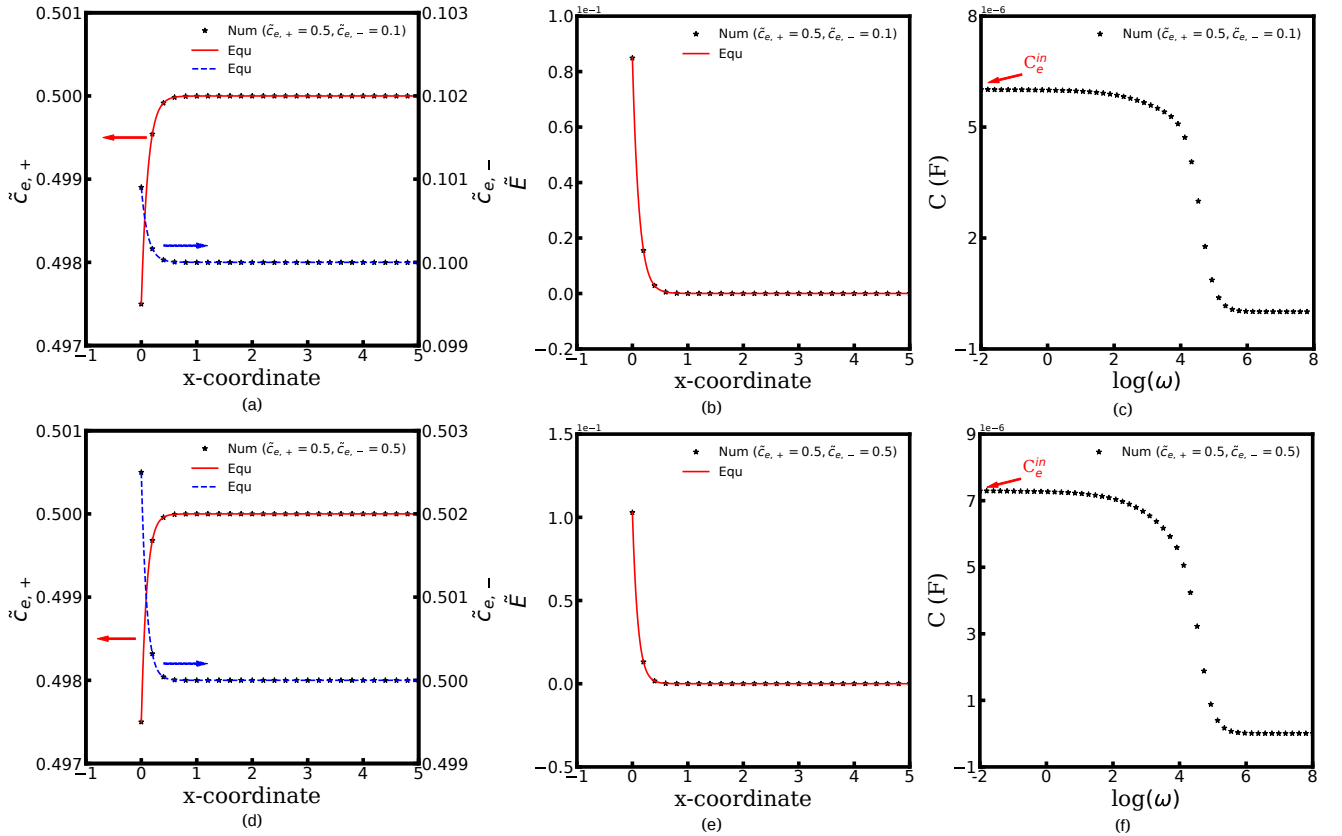


FIGURE 5.2 (a, d) Equilibrium concentration of lithium-ions $\tilde{c}_{e,+}$ and electrons $\tilde{c}_{e,-}$, (b, e) the electric field \tilde{E} at the metal/electrolyte interface. (c, f) Specific capacitance C as a function of frequencies. The upper figures are $\tilde{c}_{e,+} = 0.5$ and $\tilde{c}_{e,-} = 0.1$, and the lower figures denote $\tilde{c}_{e,+} = 0.5$ and $\tilde{c}_{e,-} = 0.5$.

Fig. 5.2 plots the equilibrium state with two different initial concentrations in the solid-state electrolyte. In the legend, “Num” represents the numerical calculated results from the MPNP model, and “Equ” indicates the derived analytical results, which are given by Eqs. (5.5) and (5.8). Note that the analytical and numerical results coincide well with each other as shown in Figs. 5.2 and indicate that the analytical solutions are correct. Moreover, we followed the method presented in Wang’s work [111] and show the specific capacitance as a function of frequencies in Figs. 5.2c and 5.2f. In the citation, the specific capacitance is calculated by $C_e^{in} = -1/(\omega Z_{im})$ and the value at the lowest frequency marked by the arrow in Figs. 5.2c and 5.2f should equal to the space charge layer capacitance C_e^{in} . According to Eq. (5.10), the estimated space charge layer capacitances can be read $C_e^{in} = 6.02 \times 10^{-6}, 7.29 \times 10^{-6}$ F, when the electron initial concentrations are $\tilde{c}_{e,-} = 0.1$ and 0.5, respectively. It is evident that the numerical result is equal to the analytical space charge layer capacitance C_e^{in} predicted by Eq. (5.10) for different concentrations. This confirms that our analytical space charge layer capacitance based on the MPNP model is accurate and can apply in any situations, e.g., immobile electrons ($D_{e,-} = 0$) or unequal mobile species concentrations ($\tilde{c}_{e,+} \neq \tilde{c}_{e,-}$).

As presented in Sec. 3.2.2, the space charge layer capacitance $C_e^{in,*}$ is also assumed to be associated with the Debye length λ_D and is given by

$$\lambda_D = \sqrt{\frac{RT\varepsilon_i\varepsilon_0}{F^2 \sum z_i^2 c_i}} \quad C_e^{in,*} = A \frac{\varepsilon_i\varepsilon_0}{\lambda_D}, \quad (5.11)$$

where the superscript “*” just shows the difference between Eqs. (5.10) and (5.11). However, we have to notice that Eq. (5.11) holds merely when the interface charge density is zero, i.e., $\tilde{c}_{e,+} - \tilde{c}_{e,-} = 0$ [71]. As shown in Figs. 5.2a and 5.2d, the charge separation happens in the space charge layer and Eq. (5.11) is somehow not suitable to calculate the interface capacitance anymore. Moreover, the comprehensive comparison between these two capacitances C_e^{in} and $C_e^{in,*}$ will be shown in the following section.

5.2.2 Impedance Analysis of Ideally Blocking Solid-State Electrolytes

We introduce the analytical space charge layer capacitance C_e^{in} based on the MPNP model in Sec. 5.2.1. However, the space charge layer resistance R_e^{in} due to the charge accumulation or depletion is not discussed yet. Thus, a particular discussion about the space charge layer impedance Z_e^{in} is presented here. The corresponding equivalent circuit model for the metal/electrolyte/metal cell and the material properties quantification for elements are given in Fig. 5.1b. In order to reduce the influence factors and simplify the consideration, the boundary conditions of the solid-state electrolyte are given by $J_{e,+}(L) = J_{e,-}(L) = 0$ on the left-hand side, and $\tilde{c}_{e,+}(R) = \tilde{c}_{e,+}$, $\tilde{c}_{e,-}(R) = \tilde{c}_{e,-}$ on the right-hand side, respectively. No charge accumulation and the space charge layer formation at the right interface, thus, $Z_{e,+}^{in}(R) = Z_{e,-}^{in}(R) = 0$ as illustrated in Fig. 5.1.

According to the previous section, the conductivity $\sigma_{e,i}$, the electrolyte bulk resistance $R_{e,i}^{bu}$ of the species i , and the bulk capacitance $C_{e,i}^{bu}$ can be expressed by

$$\sigma_{e,i} = \frac{z_i^2 F^2 D_{e,i} C_{e,i}^{bu}}{RT} \quad R_{e,i}^{bu} = \int_0^{L_e} \frac{dx}{A\sigma_i} = \frac{RTL_e}{z_i^2 F^2 AD_{e,i} C_{e,i}^{bu}} \quad C_{e,i}^{bu} = A \frac{\varepsilon_0 \varepsilon_i}{L_e}.$$

The total space charge layer capacitance C_e^{in} is given by Eq. (5.10) and the specific capacitance $C_{e,i}^{bu}$ of species i is proportional to the charge density and is depicted by

$$C_{e,+}^{in} = \frac{\tilde{c}_{e,+}^{bu}}{\tilde{c}_{e,+}^{bu} + \tilde{c}_{e,-}^{bu}} C_e^{in} \quad C_{e,-}^{in} = \frac{\tilde{c}_{e,-}^{bu}}{\tilde{c}_{e,+}^{bu} + \tilde{c}_{e,-}^{bu}} C_e^{in}. \quad (5.12)$$

According to the work by Maier [127, 148–150], the conductivity σ_i in the space charge layer is taken as an independent parameter. The space charge layer resistance R_e^{in} is merely caused by deviation from the bulk contribution and the result for this term is expressed as

$$R_{e,i}^{in} = \frac{RT}{z_i^2 F^2 AD_{e,i}} \int_0^{L_s} \frac{dx}{\tilde{c}_{e,i}^{in}} \quad \text{or} \quad R_{e,i}^{in} = -\frac{2RT\lambda_D}{z_i^2 F^2 AD_{e,i} C_{e,i}^{bu}} \frac{2\theta}{1+\theta}. \quad (5.13)$$

Where L_s is the length of the space charge layer, $D_{e,i}$ denotes the diffusivity, and θ is called the degree of influence. It can be concluded that the resistance relies on the concentration in the space charge layer and the diffusivity. For simplicity, the space charge layer resistance is calculated when the electrochemical cell is at the equilibrium state. Unfortunately, the charge density in the space charge layer depends on the frequency during the EIS measurement. In addition, Klerk [81] pointed out that the diffusivity in the space charge layer is strongly dependent on the concentration and differs from the diffusivity in the bulk. The diffusivity for the solid-state electrolyte and reaches the maximum value when the half regular lattices sites are occupied. Consequently, Eq. 5.13 is hard to explain the perturbation effect as shown in the literature. In order to solve this issue, we introduce a new frequency-dependent space charge layer impedance for the first time. The resistance is associated with the electrolyte resistance R_e^{bu} and the perturbation frequency ω , and is given by

$$R_e^{in} = \frac{R_{e,+}^{bu} R_{e,-}^{bu}}{R_{e,+}^{bu} + R_{e,-}^{bu}} \frac{1}{\omega^\alpha} \quad (5.14)$$

in which α is a coefficient representing the interface blocking level. More exactly, $\alpha = 1$ when the solid-state electrolyte is ideally blocking for lithium-ions. The total space charge layer impedance is the summary of these two parts:

$$Z_e^{in} = R_e^{in} + 1/(j\omega C_e^{in}) \quad (5.15)$$

In the transmission line shown in Fig. 5.1b, C_e^δ is called the chemical capacitance and is determined by the chemical potential μ_i^* of species i [65]. In the MPNP model, the vacancy effect in solid-state

electrolytes is included and the molar chemical potential is given by $\mu_i^* = \mu_i^\ominus + RT \ln \tilde{c}_i - RT \ln(1 - \tilde{c}_i)$. Thus, the chemical capacitance $C_{e,i}^\delta$ of species i is

$$C_{e,i}^\delta = (Fz)^2 AL_e c_{max} \left(\frac{\partial \mu_i^*}{\partial \tilde{c}_i} \right)^{-1}. \quad (5.16)$$

The electrolyte holds local electroneutrality in the homogeneous region, thus, ionic and electronic chemical capacitors are connected in series [113]. The total chemical capacitance C_e^δ is the summary of two species and is depicted by

$$C_e^\delta = \frac{1}{\sum(1/C_{e,i}^\delta)} = \frac{c_{max}(Fz)^2 AL_e}{RT} \left[\frac{1}{\tilde{c}_{e,+}^{bu}(1 - \tilde{c}_{e,+}^{bu})} + \frac{1}{\tilde{c}_{e,-}^{bu}(1 - \tilde{c}_{e,-}^{bu})} \right]. \quad (5.17)$$

According to the boundary conditions and all the above impedances, the transmission impedance Z_w in the red rectangular in Fig. 5.1b and the total impedance of the solid-state electrolyte are presented by

$$Z_w = \frac{R_{e,+}^{bu} R_{e,-}^{bu}}{R_w} + \frac{[(R_{e,+}^{bu})^2 Z_{e,+}^{in}(L) + (R_{e,-}^{bu})^2 Z_{e,-}^{in}(L)] \tanh \left[\sqrt{j\omega C_e^\delta R_w} \right] + Z_{e,+}^{in}(L) Z_{e,-}^{in}(L) R_w \sqrt{j\omega C_e^\delta R_w}}{R_w \left[R_w \tanh \left[\sqrt{j\omega C_e^\delta R_w} \right] + \sqrt{j\omega C_e^\delta R_w} [Z_{e,+}^{in}(L) + Z_{e,-}^{in}(L)] \right]}, \quad (5.18)$$

$$Z = \frac{1}{j\omega C_e^{bu} + 1/Z_w}, \quad (5.19)$$

and $R_w = R_{e,+}^{bu} + R_{e,-}^{bu}$ in Eq. (5.18).

To verify our equivalent circuit model of the metal/electrolyte/metal cell, the contrasted electrochemical impedance spectroscopy with different diffusivities are presented with the MPNP model. The applied frequency ω of the perturbation potential is from 10^{-2} to 10^8 Hz, and 50 samples of the corresponding current are recorded. The amplitude of the perturbation potential is $\tilde{\Phi}_{ac} = 0.01$ and without the direct signal $\tilde{\Phi}_{dc} = 0$. The initial dimensionless concentrations of mobile Lithium ions and electrons in the solid-state electrolyte are $\tilde{c}_{e,+} = \tilde{c}_{e,-} = 0.5$ and the diffusivities are $D_{e,+} = 10^{-14}$ and $D_{e,-} = 10^{-16} \text{m}^2 \text{s}^{-1}$, respectively.

Figs. 5.3 and 5.4 are the electrochemical impedance spectroscopies of the metal/electrolyte/metal cell and each point depicted in the curve corresponds to the specific frequency. The blue line “Equ WO/ R_e^{in} ” represents the space charge layer without the frequency-dependent resistance, which is given by $Z_e^{in} = 1/(j\omega C_e^{in})$. The red line “Equ W/ R_e^{in} ” indicates that the frequency-dependent resistance is included in the space charge layer as shown in Eq. (5.15). The green line “Equ W/ $C_e^{in,*}$ ” shows the results calculated from the commonly applied space charge layer capacitance $C_e^{in,*}$ as depicted in Eq. (5.11). It can be observed that the numerical results of the equivalent circuit model fit the MPNP model well, while still differences exist in some parts.

Fig. 5.3a is the Nyquist plot of the solid-state electrolyte and exhibits a typical curve of the ideally blocking electrolyte, which has a characteristic semicircle at the high-frequency zone and

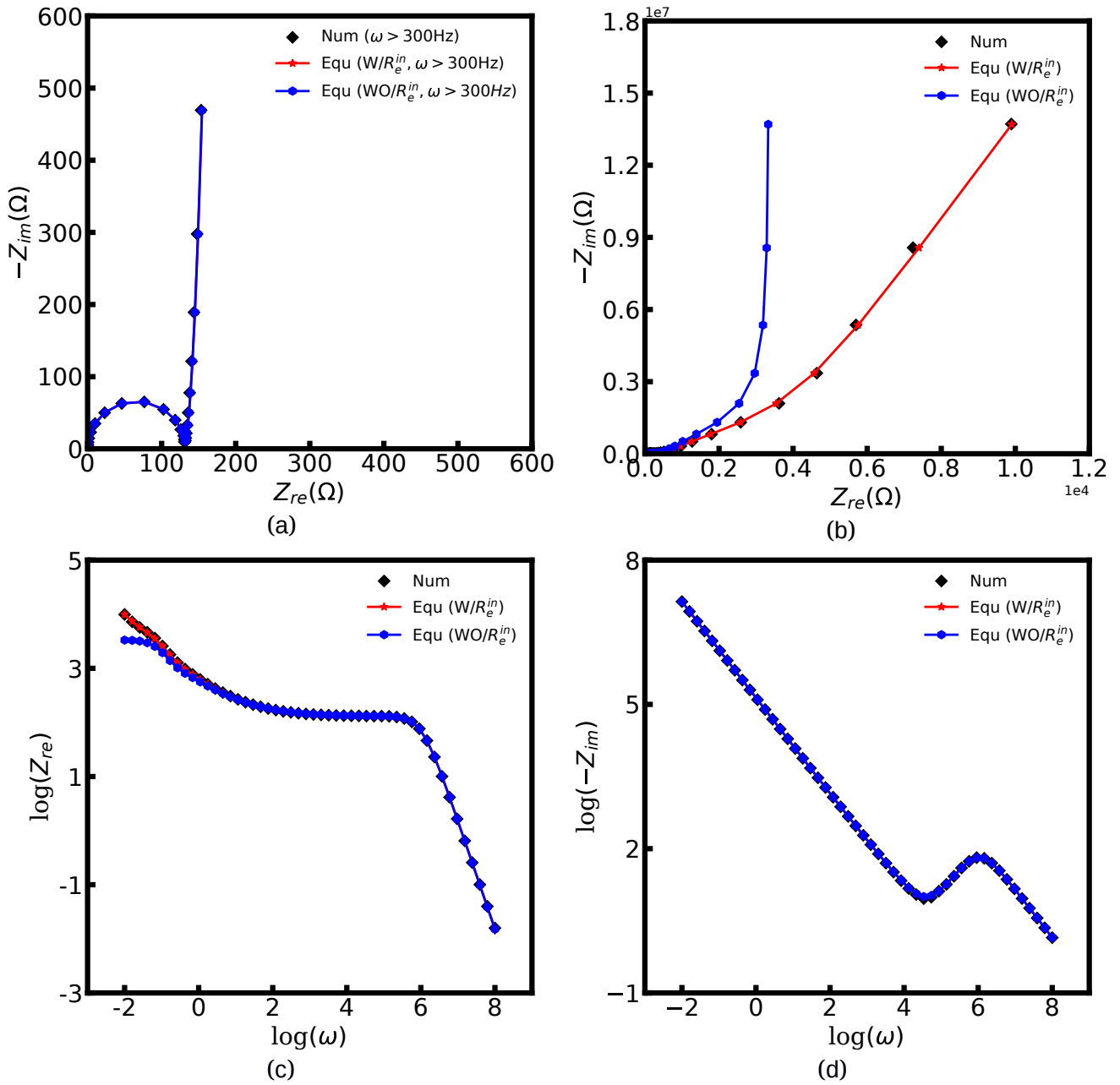


FIGURE 5.3 Nyquist plots of the solid-state electrolyte with and without the space charge layer resistance: (a) $300\text{ Hz} < \omega$, (b) $10^{-2} < \omega < 10^8\text{ Hz}$, (c, d) the corresponding real and imaginary Bode plots.

a tail at low frequencies. The semicircle represents that the solid-state electrolyte bulk capacitor C_e^{bu} is in parallel with the bulk resistance R_e^{bu} . The tail is caused by the space charge layer at the metal/electrolyte interface, and the influence is still under discussion [57, 81]. In some investigations, the space charge layer is merely regarded as a pure ideal capacitor [105] or the constant space charge layer resistance has been taken into consideration. However, as shown in the literatures [127, 144], the charge density and the space charge layer impedance are

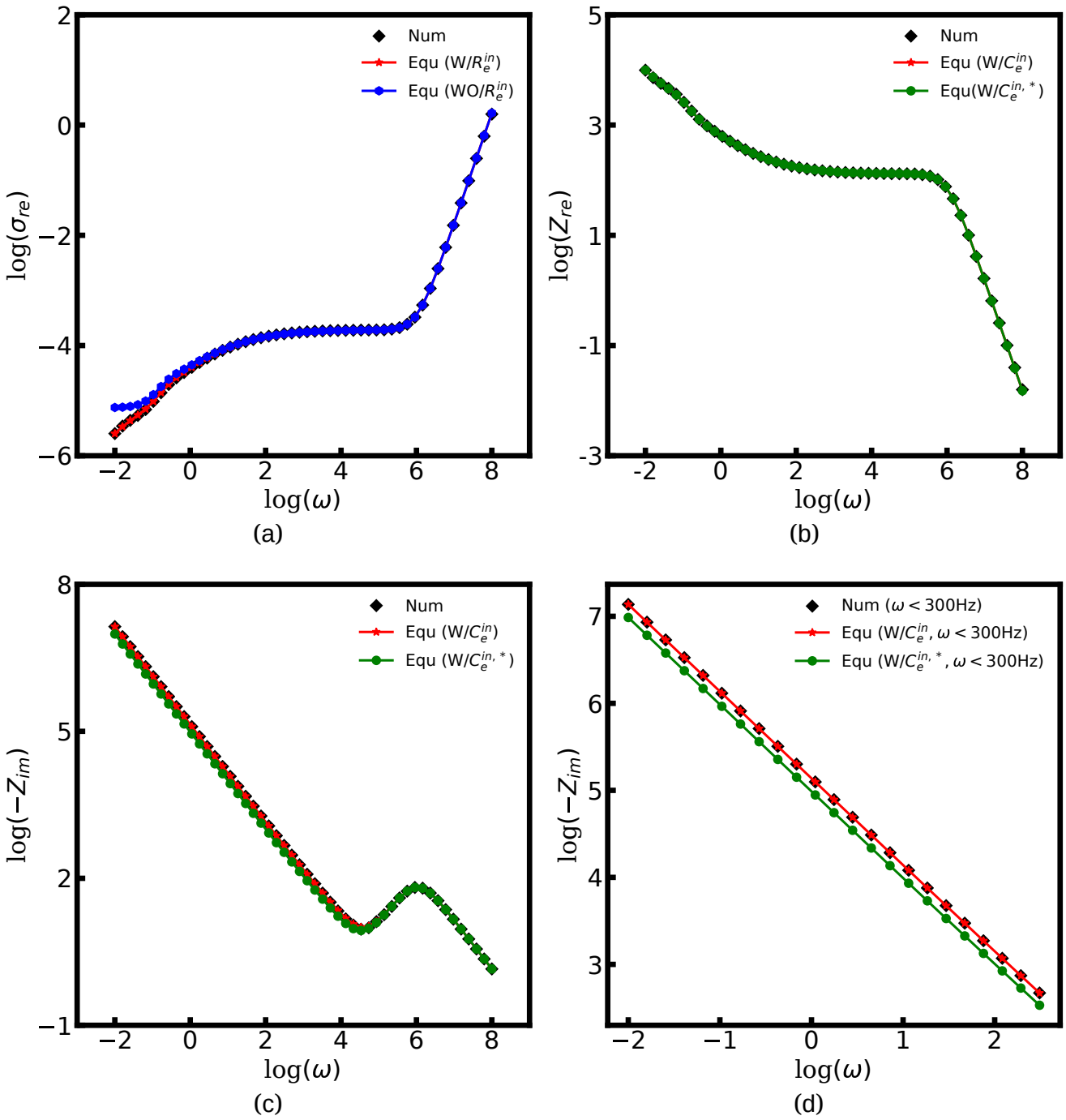


FIGURE 5.4 (e) The ionic conductivities. (f) The real Bode plot with different space charge layer capacitances, Eqs. (5.11) and (5.10) are plotted. The imaginary Bode plots: (g) $10^{-2} < \omega < 10^8$ Hz and (h) $\omega < 300$ Hz.

frequency-dependent. In order to comprehensively investigate the space charge layer impedance, a new frequency-dependent space charge layer resistance is included in the proposed equivalent circuit model and exhibits a large influence at low frequencies.

Fig. 5.3b plots the overall results ($10^{-2} < \omega < 10^8$ Hz) of these two cases. It is evident

that the space charge layer without the frequency-dependent resistance R_e^{in} fails to match the electrochemical results at low frequencies. Figs. 5.3c and 5.3d are the real and imaginary Bode plots, respectively, and the numerical results are well fitted with our equivalent circuit model by introducing the new space charge layer resistance. Moreover, it can be noted that the space charge layer resistance plays an important role at low frequencies. Fig. 5.4a is the ionic conductivity curve of the solid-state electrolyte, and is similar to the experimental results of the LiPON thin film as given in the literature [105, 107, 146, 147] and will be discussed in detail in the following part. To further confirm our impedance results, we follow the method given by Yu [147] and calculate the ionic conductivity $\sigma_{e,+}$ of the solid-state electrolyte. The result is calculated from the real impedance Z_{re} at the frequency ω at which $-Z_{im}$ goes through a local minimum, and this feature is also verified in both of our numerical and equivalent circuit models. Fig. 5.4b to 5.4d are the Bode plots with the different space charge layer capacitances. $C_s^{in,*}$ is the extensively applied method to estimate the space charge layer capacitance and is shown by Eq. (5.11). We can note that the derived space charge layer capacitance C_e^{in} exhibits more accurately than $C_e^{in,*}$ when fitting impedance results.

In real materials, the electronic conductivity of solid-state electrolytes is extremely low and can be assumed as immobile electrons when compared with lithium-ion, e.g., $\sigma_{e,+} = 10^{-6} \text{ S cm}^{-1}$ and $\sigma_{e,-} = 10^{-15} \sim 10^{-12} \text{ S cm}^{-1}$ in LiPON [108]. Thus, we discuss the solid-state electrolyte with immobile electrons to verify the applicability of the proposed equivalent circuit model. Here, the diffusivity $D_{e,-} = 0$, $D_{e,+} = 10^{-14} \text{ m}^2 \text{ s}^{-1}$ and the initial concentrations are $\tilde{c}_{e,+} = \tilde{c}_{e,-} = 0.5$. Because of the immobile electrons, the electronic line in the transmission line in Fig. 5.1b is ignored. In the corresponding equivalent circuit model, the electronic resistance is $R_{e,-}^{bu} = 0$ and the space charge layer capacitance C_e^{in} is merely caused by lithium-ions and is given by

$$C_{e,+}^{in} = C_e^{in} = A \frac{Fc_{max} \left[\frac{-z\tilde{c}_{e,+}^{bu} e^{-zF\Phi_e^{bu}/RT}}{1 + \tilde{c}_{e,+}^{bu} (e^{-zF\Phi_e^{bu}/RT} - 1)} \right] + F\tilde{c}_{e,+}^{bu} c_{max}}{\sqrt{\frac{2RTc_{max}}{\varepsilon_0\varepsilon_i} \ln [1 + \tilde{c}_{e,+}^{bu} (e^{-zF\Phi_e^{bu}/RT} - 1)] + \frac{2F\Phi_e^{bu}\tilde{c}_{e,+}^{bu} c_{max}}{\varepsilon_0\varepsilon_i}}}. \quad (5.20)$$

The space charge layer impedances are given by $Z_{e,+}^{in}(L) = R_{e,+}^{in} + 1/(j\omega C_{e,+}^{in})$ and $Z_{e,-}^{in}(L) = 0$, respectively. The polarization capacitance is connected in series with the ionic resistance [65] and the transmission line impedance Z_w is

$$Z_w = R_{e,+}^{bu} + Z_{e,+}^{in}(L) + \frac{1}{j\omega C_e^\delta}. \quad (5.21)$$

To better understand the frequency-dependent space charge layer resistance, the impedance plots with immobile electrons in the solid-state electrolyte are shown in Fig. 5.5. When the space charge layer is assumed to be a capacitor, i.e., the space charge layer resistance R_e^{in} is ignored, the corresponding equivalent circuit model fails to show the tail as shown in Fig. 5.5c. The reason

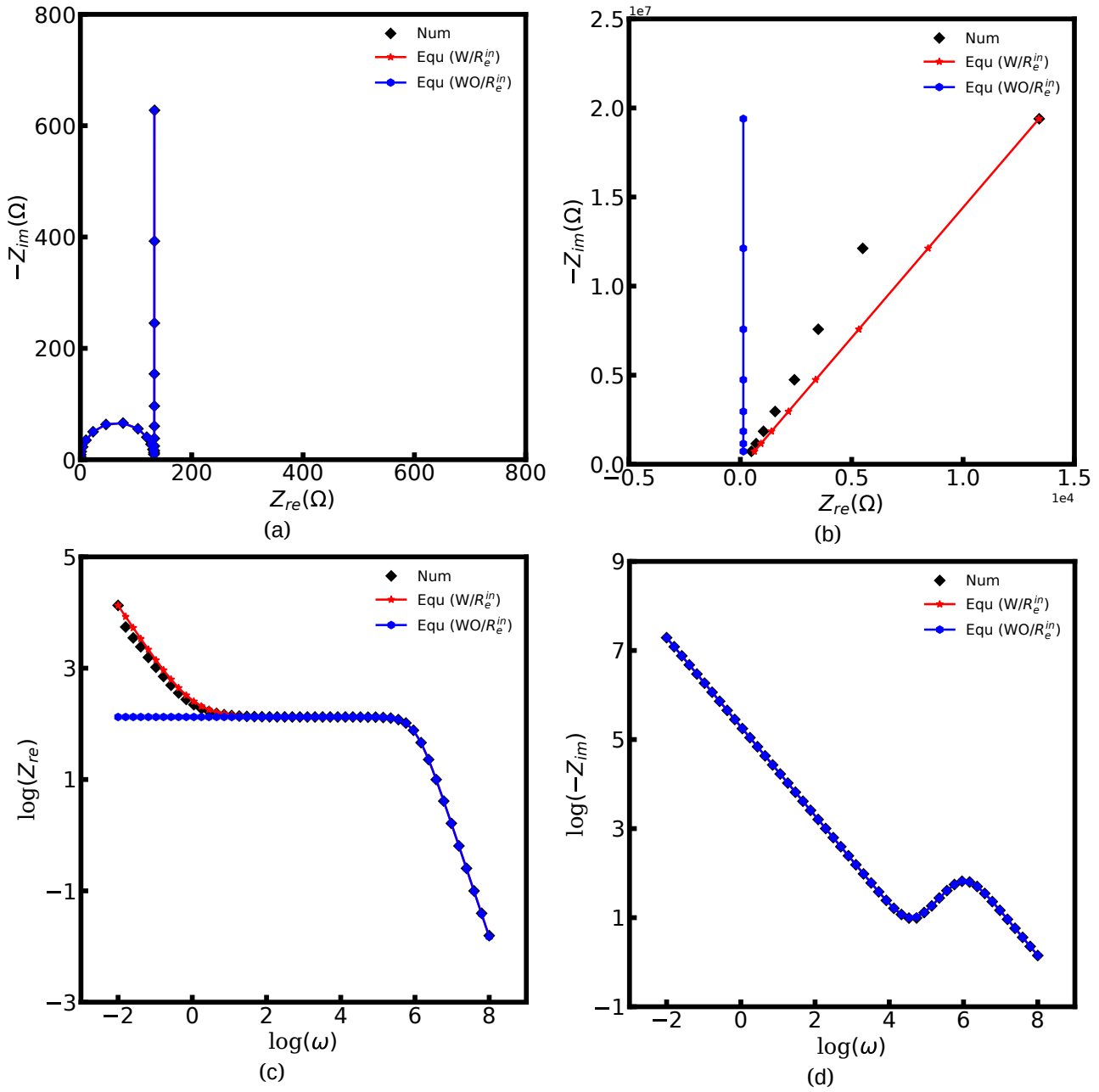


FIGURE 5.5 Nyquist plots of the solid-state electrolyte with and without the space charge layer resistance: (a) $300 \text{ Hz} < \omega$, (b) $10^{-2} < \omega < 10^8 \text{ Hz}$, (c, d) the corresponding real and imaginary Bode plots

is that lithium-ions deplete in the space charge layer and lead to a drastic potential drop at low frequencies. The depletion layer and the potential are frequency-dependent; unfortunately, the pure capacitor C_e^{in} is unable to explain this effect. In our equivalent circuit model, the frequency-dependent impedance R_e^{in} is included in the space charge layer and the results fit quite well. The slight difference is caused by the total current deviation. From the above discussion, we can conclude that the pure capacitor assumption is unable to explain the real impedance tail, which is shown in Fig. 5.5c, and the frequency-dependent space charge layer resistance R_e^{in} has to be

considered for a perfect fit.

5.2.3 Impedance Analysis of Non-ideally Blocking Solid-State Electrolytes

In Sec. 5.2.2, we discuss an ideally blocking electrolyte for both lithium-ions and electrons. Nevertheless, electrons cannot be ideally blocked and may transfer to the blocking electrode, e.g. Au and Pt. To further verify our proposed equivalent circuit model and the elements quantifications, a non-blocked solid-state electrolyte for electrons is presented in this section. The initial concentrations for lithium-ions and electrons in the solid-state electrolyte are $\tilde{c}_{e,+} = \tilde{c}_{e,+} = 0.5$, and other parameters are taken from Tab. 5.1. The concentration boundary conditions are given by $J_{e,+}(L) = 0$ and $\tilde{c}_{e,-}(L) = 0.5$ on the left-hand side, and $\tilde{c}_{e,+}(R) = \tilde{c}$, $\tilde{c}_{e,-}(L) = \tilde{c}$ on the right-hand side, respectively.

Based on the equivalent circuit model as depicted in Fig. 5.1b, the transmission line impedance Z_w of non-ideally blocking electrolytes leads to

$$Z_w = \frac{R_{e,+}^{bu} R_{e,-}^{bu}}{R_w} + \frac{(R_{e,-}^{bu})^2 Z_{e,+}^{in}(L)}{R_w^2 + \cosh\left(\sqrt{j\omega C_e^\delta}\right) \left[R_w Z_{e,+}^{in}(L) \sqrt{j\omega C_e^\delta} R_w \right]} \quad (5.22)$$

Figs. 5.6a and 5.6b are the Nyquist plots of the solid-state electrolyte at high frequencies and the overall results. The semicircle attributes to the solid-state electrolyte bulk capacitor C_e^{bu} and resistance R_i^{bu} and is also observed in Fig. 5.3a. It can be noted that the numerical and analytical impedance curves fit quite well and show the applicability of our circuit model. Nevertheless, in comparison to Figs. 5.3 and 5.5, the space charge layer effect cannot be observed in Fig. 5.6. This phenomenon attributes to non-blocking electrons, as shown in Fig. 5.1b, the total space charge layer impedance consists of ionic and electronic lines, i.e., $Z_{e,+}^{in}(L)$ and $Z_{e,-}^{in}(L)$. When electrons are non-blocking in solid-state electrolytes, i.e., $\tilde{c}_{e,-}(L) = 0.5$, no space charge layer formation at the interface, and the electronic line interface impedance yields $Z_{e,-}^{in}(L) = 0$. Therefore, the ionic line is a short circuit under this condition and lithium-ion interface impedance $Z_{e,+}^{in}(L)$ is overlooked at low frequencies.

5.2.4 Impedance Analysis of Grain Boundaries in Solid-State Electrolytes

In the above sections, we present a specific discussion with ideally blocking and non-ideally electrolytes. However, the grain and grain boundary impedances are also difficult to analyse and puzzle researchers. According to the investigations [148, 151–153], lithium-ions can form the space charge layer in the grain boundary region like a solid/solid interface. Here, we will utilize the proposed equivalent circuit model to deeper the understanding of the grain and grain boundary impedances.

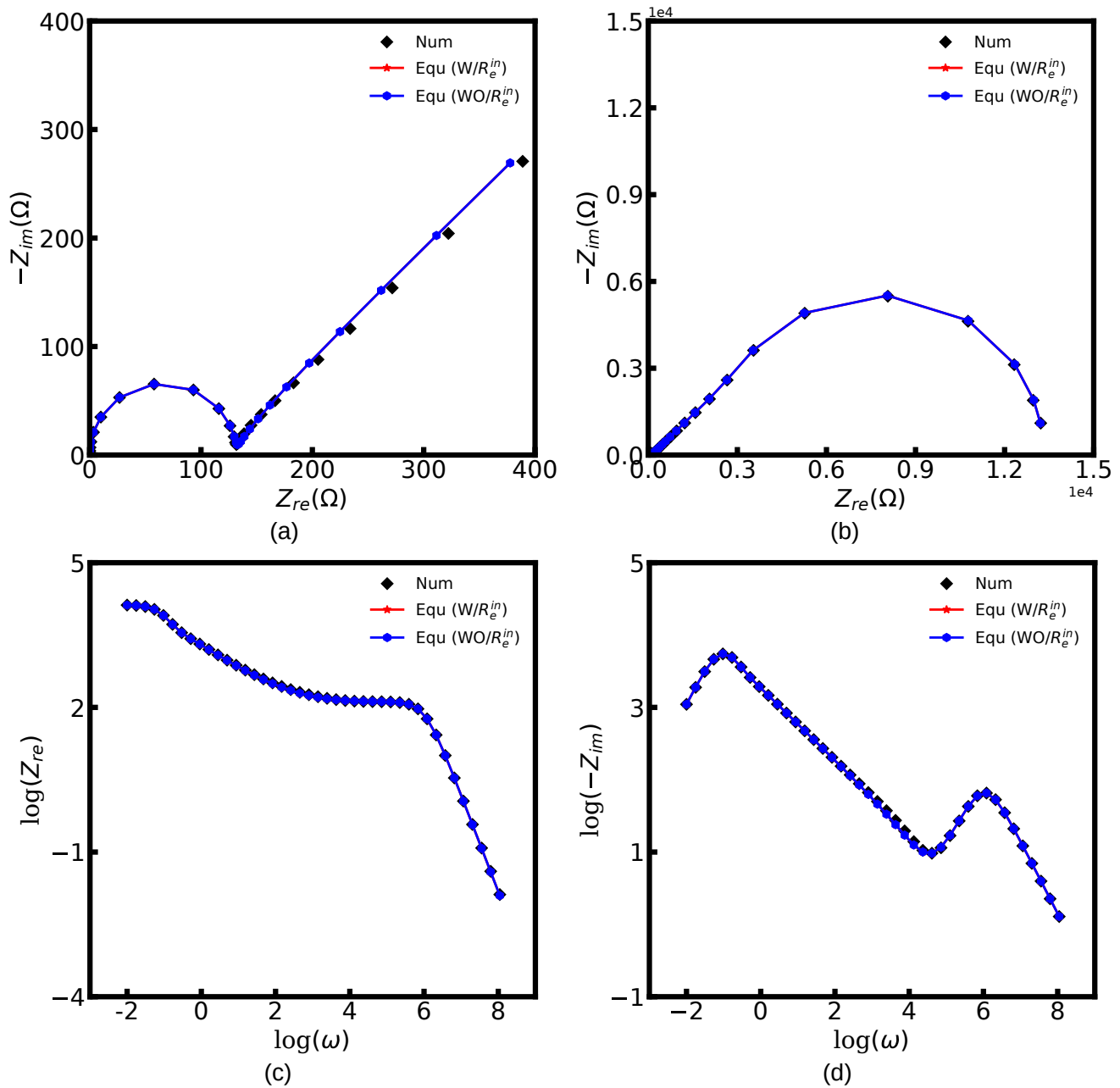


FIGURE 5.6 Nyquist plots of the solid-state electrolyte with and without the space charge layer resistance: (a) $300 \text{ Hz} < \omega$, (b) $10^{-2} < \omega < 10^8 \text{ Hz}$, (c, d) the corresponding real and imaginary Bode plots

When the grain boundary impedance is much larger than the grain resistance, the grain is similar to an ideally blocking electrolyte. Thus, the total grain can be estimated by Eqs. (5.18) and (5.21), and the capacitance associated to the grain boundary can be observed. As shown in a previous study [154], the grain boundary impedance of LATP is about one order of magnitude higher than its grain resistance at the room temperature. Therefore, the electrolyte impedance curve show a non-ideal vertical tail at low frequencies. When the grain boundary impedance can

be ignored in comparison to the grain impedance, i.e., the non-ideally blocking electrolyte, the space charge layer capacitance is vanished at low frequencies. Therefore, the impedance curve at the medium-frequency range is a 45° line, as shown in Fig. 5.6a, and this phenomenon is also widely observed in experimental results [152, 153].

5.2.5 Impedance Analysis of Temperature Influence

We introduced an advanced MPNP model and the corresponding equivalent circuit model for the metal/electrolyte/metal cell impedance calculation in Secs. 5.2.2 and 5.2.3. In order to confirm our models, we consider the temperature influence and verify our results by the experimental data published in the literature [107]. The conductivity and permittivity are calculated using the following equations

$$\sigma(\omega) = \frac{L}{A} \left[\frac{1}{Z_{re}(\omega)} + \frac{j}{Z_{im}(\omega)} \right] = \sigma_{re}(\omega) + j\sigma_{im}(\omega) \quad \varepsilon = \frac{\sigma(\omega)}{j\omega\varepsilon_0} = \varepsilon_{re}(\omega) - j\varepsilon_{im}(\omega). \quad (5.23)$$

According to the experiments, the electrolyte ionic conductivity $\sigma_{e,+}$ follows the Arrhenius behaviour and is described by the equation

$$T\sigma_{e,+} = \sigma_0 \exp\left(-\frac{E_a}{k_b T}\right), \quad (5.24)$$

where σ_0 is the pre-exponential factor, E_a is the hopping activation energy in LiPON, and k_b is the Boltzmann constant. From Eq. (5.24), the electrolyte ionic conductivity σ_+ increases with increasing the temperature T , and the plot is shown in Fig. 5.7a. Because the diffusivity is proportional to the ionic conductivity, different lithium-ions diffusivities are discussed in order to simplify the calculation. The initial concentrations in the solid-state electrolyte are $\tilde{c}_{e,+} = \tilde{c}_{e,-} = 0.5$; however, with different diffusion coefficients $D_{e,+} = 10^{-14}, 2 \times 10^{-14}, 4 \times 10^{-14} \text{ m}^2 \text{ s}^{-1}$ and $D_{e,-} = 10^{-16} \text{ m}^2 \text{ s}^{-1}$.

Figs. 5.7 presents the ionic conductivity and permittivity calculated by our equivalent circuit model with different temperatures. In Figs. 5.7b and 5.7c, the impedance curves are divided into three parts, i.e., high frequency ($10^6 < \omega$), medium frequency ($10^2 < \omega < 10^6$) and low frequency regions ($\omega < 10^2$), which are similar to experimental results [107, 131, 154]. At high frequencies, the ionic conductivity increases dramatically with the frequency ω while the permittivity reaches a stable limit. Thus, the material corresponds to a relaxed system without an electric field. Therefore, lithium-ion tend to non-randomly hopping and migrate by carrying along their neighbours, in the manner of “jellyfish-type” movement [154–156]. Moreover, in Fig. 5.7c, the intersection of the dashed line and the permittivity curve corresponds to the equilibrium relative permittivity ε_i marked by the arrow as given in Tab. 5.1. The intersection value is $\log(\varepsilon_{re}) = 1.3$ in Fig. 5.7c, thus the calculated permittivity is $\varepsilon_{re} = 19.95$ and fulfils the material relative permittivity ε_i . This result can verify that our equivalent circuit model is physical from another perspective. In the

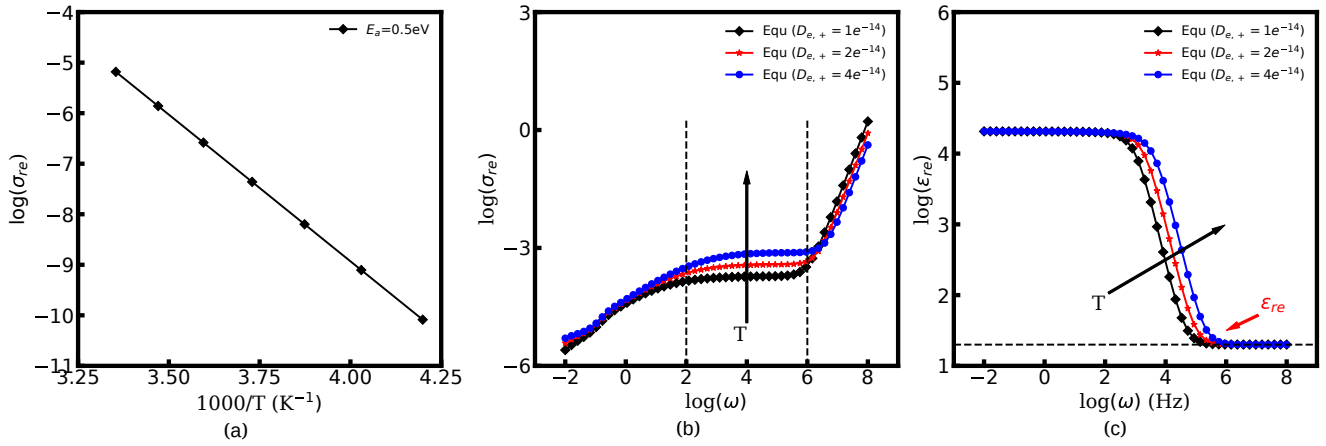


FIGURE 5.7 (a) Temperature dependence of the ionic conductivity (b), (c) frequency dependence of the real ionic conductivity and permittivity with different diffusivities.

medium-frequency region, the ionic conductivity curve shows a stable plateau, which corresponds to the constant value $\sigma_{e,+}$ in Eq. (5.23). Figs. 5.7b shows that the material conductivity $\sigma_{e,+}$ increases with the diffusivity, which also means that the ionic conductivity increases with the temperature. In medium-frequency ranges, lithium-ions migrate randomly and are described by Eq. (5.24). At low frequencies, the ionic conductivity decreases to a relatively low value due to the polarization effect [105]. With a low-frequency potential perturbation, electrons accumulate in the space charge layer, then leading to a depletion of lithium-ions. The feature causes a large electrostatic potential drop and a drastic fall of the ionic conductivity in this small region. Even though this equivalent circuit model is able to calculate the impedance spectroscopies at different temperatures, the permittivity influence is not included. The solid-state electrolyte permittivity is also changed with the temperature, this part can be taken into consideration in the future work.

5.3 Experimental Verification

We introduced an advanced MPNP model and the corresponding equivalent circuit model for the impedance spectroscopy simulation in the above sections. The calculated impedance spectroscopy shows typical features, which are observed in experimental results. To further verify our equivalent circuit model, the impedance data which taken from [107] are applied to compare them with our equivalent circuit model. In his work, Pt/LiPON/Pt cell operates with an AC perturbation and the thickness of solid-state electrolyte LiPON is $L_e = 1.4 \mu\text{m}$, the active surface area is $A = 1 \times 10^{-5} \text{ m}^2$. According to the electrochemical analysis, the mobile lithium-ion concentration is $c_{e,+} = 249.17 \text{ mol m}^{-3}$ and the maximum concentration is $c_{max} = 5.98 \times 10^4 \text{ mol m}^{-3}$. The diffusion coefficient of lithium-ions is uncertain based on different measurement methods and the

range is from 1.7×10^{-13} to $2 \times 10^{-12} \text{ m}^2 \text{ s}^{-1}$ at 300 K. Concerning the impedance spectroscopy and other ionic conductivity values of the LiPON thin film [157], lithium-ion diffusion coefficient is determined as $D_{e,+} = 1.7 \times 10^{-13} \text{ m}^2 \text{ s}^{-1}$ in the calculation. Thus, the ionic and electronic conductivities are $\sigma_{e,+} = 1.58 \times 10^{-4}$ and $\sigma_{e,-} = 8 \times 10^{-12} \text{ S m}^{-1}$, respectively. Moreover, the relative permittivity in his measurement is around $\varepsilon_i = 45$ according to the data from Fig. 5 in the citation [107]. The electronic conductivity is much smaller than the ionic conductivity, thus, the electronic resistance is ignored in the simulation. The relevant equivalent circuit model for the impedance spectroscopy simulation is given by Eq. (5.21)

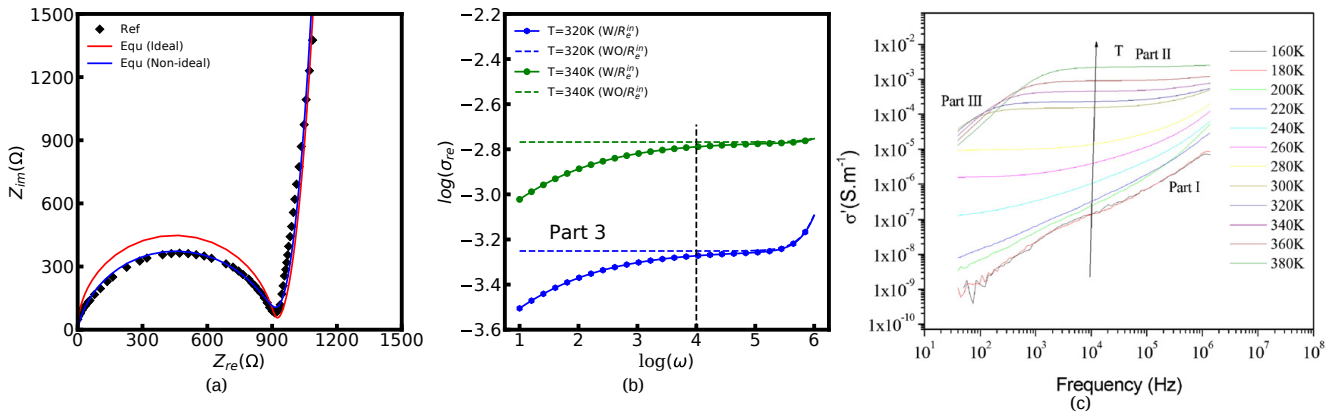


FIGURE 5.8 (a) Nyquist plot, (b) conductivity of LiPON calculated by the equivalent circuit model, and (c) experimental data as presented by ref [107]. Reproduced with the permission from Le Van-Jodin et al. Copyright 2013 Elsevier

Fig. 5.8 shows the Nyquist impedance plots of the experimental and the equivalent circuit model results. Because lithium-ions in solid-state electrolytes cannot be ideally blocked in practical, this deviation has to be taken into consideration. As shown in Eq. (5.14), α represents the solid-state electrolyte blocking for lithium-ions and is given as $\alpha = 0.4$ in our calculation. The legend “Equ (Ideal)” indicates the solid-state electrolyte is an ideal capacitor and vice versa. It is evident that the curves fit well at low frequencies but have a slight difference in the high-frequency region. Due to the real material properties, the solid-state electrolyte cannot be regarded as an ideal capacitor. It can be observed that our ideal equivalent circuit model is not able to show the depressed semicircle in the experimental curve. In order to tackle this issue, the non-ideal capacitor of the solid-state electrolyte is considered [105], and is presented by $1/(j\omega C_e^{bu})^\beta$. Thus, the depressed semi-circle is clearly shown in our equivalent circuit model with a non-ideal electrolyte. These results clearly show the application of our equivalent circuit model. Fig. 5.8b presents the conductivity curves of LiPON thin film layer at different temperatures, and Fig. 5.8c is the experimental results taken from the literature [107]. Note that the impedance tail at low frequencies is clearly shown in both our equivalent circuit model and experimental results.

However, this feature cannot be observed in the widely applied circuit model without the space charge layer resistance R_e^{in} . This result shows the advantage of our new model and verifies the influence of the space charge layer resistance. We have to notice that all the inputs of the LiPON layer in our model are merely derived from the citation and may show the deviations, but these results can still show the applicability of the proposed equivalent circuit model.

5.4 Summary

In this work, we employ the MPNP model and the corresponding equivalent circuit model for the solid-state electrolyte impedance simulation. Within the MPNP framework, the space charge layer and the unoccupied regular lattice sites (vacancies) in the solid-state electrolyte are considered. In the proposed equivalent circuit model, the elements are quantified and related to the solid-state electrolyte properties. Verified by the experimental impedance results (Pt/LiPON/Pt), this equivalent circuit model is physically meaningful and can calculate the solid-state electrolyte impedance which includes the space charge layer. It should be noted that the equivalent circuit model is a general model for solid-state electrolytes and provides a perspective to identify the origin of high interface resistance.

To figure out the interface impedance, the analytical space charge layer capacitance is derived based on the MPNP model. The concentrations of mobile species in the solid-state electrolyte are discussed. Thus the analytical capacitance is not only limited to the neutrality case. We also discuss the compositions of space charge layer impedance in detail and introduce the frequency-dependent resistance in the corresponding equivalent circuit model. The impedance is caused by the perturbed charge density in the space charge layer. Numerical results indicate that the space charge layer resistance has a critical influence on the impedance spectroscopy in the low-frequency region, especially for the electrolyte with immobile electrons. Moreover, the calculated spectroscopies clearly show that the ionic conductivities increase with the temperature and fulfill the Arrhenius equation. To verify our equivalent circuit model further, the relative permittivity is calculated from the spectroscopies and is equal to the material property. This study presents a physical equivalent circuit model to calculate the solid-state electrolyte impedance and provides specific explanations about the space charge layer impedance. Moreover, the material properties quantifications are studied in order to investigate and optimize the high interface impedance of the solid-state electrolyte. This electrochemical continuum model will be used to calculate the full cell impedance which considers cathode/electrolyte interface reaction in the next chapter.

6 Impedance Modelling of ASSBs: Influence of the Kinetic Reaction

Noted that this chapter is based on the publication “Y. Liu, W.-B Yu and B.-X. Xu, *Journal of Materials Chemistry A*, 10, 313-325 (2022)”.

In Chap. 5, we present a specific explanation of the space charge layer impedance in solid-state electrolytes. This work ignores lithium-ion reaction at the interface and cannot be applied to calculate the cell impedance. ASSBs obtain a high interface impedance and this is the inevitable bottleneck for the development of high performance batteries for electrical vehicles and other applications [20, 75, 158, 159]. During the charging and discharging process, charges accumulate at the interface and form the space charge layers in both the electrode and the electrolyte [89, 90, 92]. The charge density and the space charge layer thickness are associated with the reaction kinetics. As shown in the reference [75], the interface impedance decreases from $1710 \Omega \text{ cm}^2$ to $1 \Omega \text{ cm}^2$ with an ultrathin Al_2O_3 layer, and the reason lies in the lithium-ion binding energy difference of materials (11.4 to 1.6 eV nm^{-2}). Nevertheless, the energy parameters that appear in the Butler-Volmer (BV) equation and the reaction kinetics are never addressed in the current electrochemical impedance models. Consequently, a methodology to include within the impedance calculation directly the information of the energy barrier is still missing.

To address these issues, the MPNP-FBV model and the corresponding equivalent circuit model for ASSBs impedance calculation are proposed in this work. All elements in the equivalent circuit model can be quantified from material properties and the related equilibrium quantities such as the exchange current and the bulk electrostatic potentials. This work is the first theoretical study that considers the reaction kinetics in the battery impedance calculation. It provides a novel perspective on the microscopic origin of the interface impedance. The work is organized as follows: In Sec. 6.1, lithium-ion reaction kinetics at the solid/solid interface, the MPNP-FBV model, the impedance calculation methodology, and the corresponding equivalent circuit model for ASSBs are presented. Sec. 6.2 shows the calculated exchange current and the impedance spectroscopy. Here, the impact of the free enthalpy difference, the diffusivity, and the electrical double layer structure on the impedance are investigated. A summary of this work and an outlook are shown in Sec. 6.3.

6.1 Impedance Models for ASSBs

6.1.1 Interface Reaction Kinetics

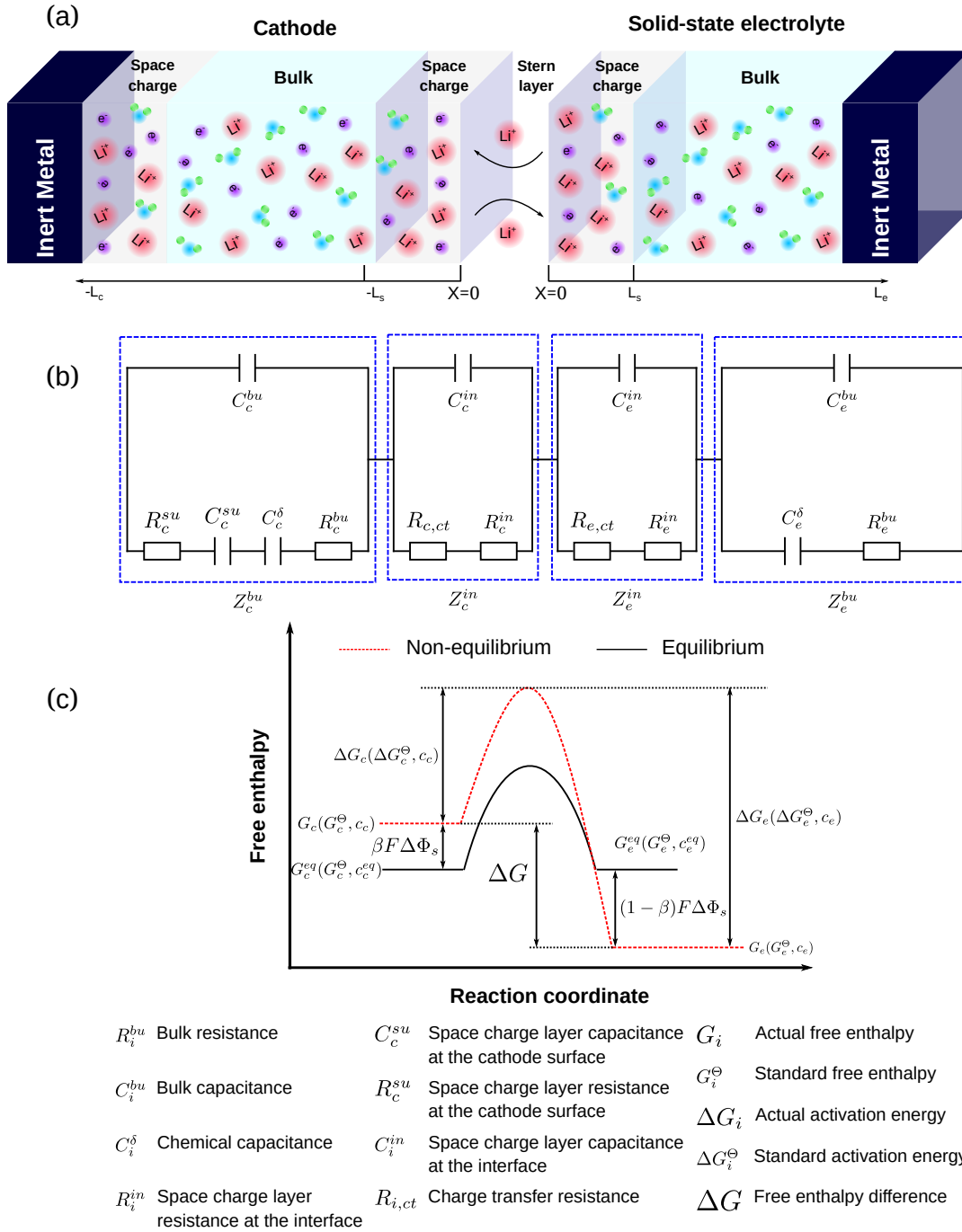
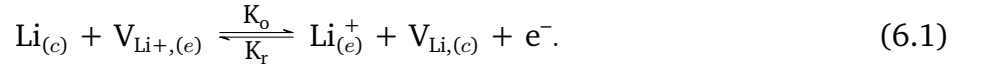


FIGURE 6.1 (a) The schematic of a cathode/electrolyte half cell, and (b) the proposed equivalent circuit model. (c) The free enthalpy profile of lithium-ion reaction at the electrode/electrolyte interface.

Here, we consider a half cell consisting of a cathode and a solid-state electrolyte as an example for simplicity. Fig. 6.1a illustrates the schematics of characteristic regions in the half cell that

operates with a perturbation potential. Due to the initial free enthalpy difference of materials, lithium-ion reaction happens spontaneously at the cathode/electrolyte interface and form the space charge layers. Denote the thickness of the cathode by L_c and the solid-state electrolyte with a thickness L_e . Based on the electrochemical continuum model, which will be explained in following subsections, we propose the corresponding equivalent circuit model as illustrated in Fig. 6.1b. Thereby the circuit elements are closely related to material properties, and physical explanations are shown in the following sections. To deepen the understanding, the free enthalpy profile of the electrochemical reaction is depicted in Fig. 6.1c. Unless it is stated differently, the subscripts “c” and “e” in this work indicate the cathode and the electrolyte, respectively. G_c (G_e) denotes the corresponding actual free enthalpy and is determined by both the standard free enthalpy G_c^\ominus (G_e^\ominus) and the concentration c_c (c_e). In addition, ΔG is the free enthalpy difference of materials and is expressed as $\Delta G = G_c - G_e$.

To take the vacancy effect into consideration, the modified FBV equation has been employed to model lithium-ion reaction at the cathode/electrolyte interface and is expressed as



It should be noticed that the amount of vacancies, e.g., $\text{V}_{\text{Li}+, (e)}$ and $\text{V}_{\text{Li}, (c)}$, constrains lithium-ion reaction rate at the interface. Here, the partial flux of reactions yields

$$\begin{aligned} J_c &= K_o \exp\left(-\frac{F\Delta G_c^\ominus}{RT}\right) \exp\left[\frac{\beta F\Delta\Phi_s}{RT}\right] c_c [c_{max} - c_e], \\ J_e &= K_r \exp\left(-\frac{F\Delta G_e^\ominus}{RT}\right) \exp\left[-\frac{(1-\beta)F\Delta\Phi_s}{RT}\right] c_e [c_{max} - c_c]. \end{aligned} \quad (6.2)$$

As shown in Eq. (6.2), the energy parameters of the specific material are involved, values of which can be obtained from the DFT calculation and allows us to take into the atomic structure into account in the kinetics simulation. $\Delta\Phi_s$ represents the electrostatic potential drop in the Stern layer and is given by $\Delta\Phi_s = \Phi_c - \Phi_e$. Without the external perturbation at the equilibrium state, i.e., the net current is zero, the partial currents must be numerically equal, and both have the same magnitude called the exchange current density J_0 [68]. Therefore, the exchange current leads to

$$I_0 = FAJ_0 = FA(K_o')^{1-\beta} (K_r')^\beta (c_c^{eq})^{1-\beta} (c_{max} - c_e^{eq})^{1-\beta} (c_e^{eq})^\beta (c_{max} - c_c^{eq})^\beta. \quad (6.3)$$

Hereby A is the cross section area, and the superscript “eq” represents interface lithium-ion concentrations at the intrinsic equilibrium state, i.e., $J_c = J_e = J_0$. In addition, K_r' and K_o' are expressed as

$$K_o' = K_o \exp\left(-\frac{F\Delta G_c^\ominus}{RT}\right) \quad K_r' = K_r \exp\left(-\frac{F\Delta G_e^\ominus}{RT}\right), \quad (6.4)$$

where R is the gas constant, T is the temperature, and F is the Faraday constant. The charge transfer resistance is inversely proportional to the exchange current and is given by

$$R_{ct} = \frac{RT}{FI_0}. \quad (6.5)$$

Eqs. (6.3) and (6.5) indicate that the charge transfer resistance is explicitly determined by the standard activation energy barrier ΔG_i^\ominus (i indicating c or e) and the equilibrium concentrations c_c and c_e at the interface. The latter is eventually also determined by the other material parameters.

The two electrostatic potentials at the solid/solid interface can be related by the diffuse double layer model [68]. Moreover, experimental results [70] also show the similar distribution of the electrostatic potential for solid-state batteries. Within the diffuse double layer model, the electrostatic potential drops both in the space charge layer and the Stern layer. Therefore, the potential distribution in the space charge layer should be numerically identified and the interface condition is defined as

$$\Phi_c = \Phi_e - \vec{n} \cdot \lambda_s \nabla \Phi_c. \quad (6.6)$$

λ_s denotes the thickness of the Stern layer and is independent of materials, i.e., $\lambda_s = H/2 = 0.3 \sim 0.5$ nm, where H is the diameter of lithium-ion [68, 71]. where Φ_c and Φ_e are the interface electrostatic potentials in the cathode and the solid-state electrolyte, respectively. $\nabla \Phi_c$ is the differential of the electrostatic potential drop in the Stern layer. More details about the FBV equation and the interface condition can refer to our previous work [160].

6.1.2 Electrochemical Model and Methodology

The electrochemical models for the solid components, i.e., cathode or electrolyte, share the similar structure but are subjected to the corresponding material parameters. The electrochemical potential for the component i ($i = c$ or e) is expressed as $\mu_i = \mu_i^\ominus + RT \ln \tilde{c}_i / (1 - \tilde{c}_i) + z_i F \Phi$, where μ_i^\ominus indicates the standard chemical potential and \tilde{c}_i denotes the normalized concentration in the corresponding component c_i (more exactly c_c or c_e) [65]. Under this circumstance, a material balance leads to the differential conservation law and is given by

$$\frac{\partial c_i}{\partial t} = \frac{D_i}{1 - \tilde{c}_i} \nabla^2 c_i + z_i \frac{F D_i}{RT} \nabla \cdot (c_i \nabla \Phi). \quad (6.7)$$

In addition, the relationship between the charge density and the electrostatic potential is depicted by the Poisson equation

$$\nabla^2 \Phi = -\frac{F}{\varepsilon_0 \varepsilon_i} (z_+ c_+ + z_- c_-). \quad (6.8)$$

Where ε_0 and ε_i represent the vacuum and the relative dielectric permittivities, respectively, and z_i denotes the valence of species i . As depicted in Fig. 6.1a, the pulse electric potential formulates

$\Phi = \Phi_{dc} + \Phi_{ac}(\cos \omega t + j \sin \omega t)$, and the resulting current is expressed as $I = I_{dc} + I_{ac}[\cos(\omega - \omega_0)t + j \sin(\omega - \omega_0)t]$. Therefore, the impedance Z leads to [94, 95]

$$Z = \frac{\Phi_{ac}(\cos \omega t + j \sin \omega t)}{I_{ac}[\cos(\omega - \omega_0)t + j \sin(\omega - \omega_0)t]} = Z_{re} + j \cdot Z_{im}, \quad (6.9)$$

Z_{re} and Z_{im} are the real and imaginary parts of the complete impedance of the battery, and more details can refer to Chaps. 3 and 5. The applied boundary conditions of the concentration are $J_c(L) = 0$ and $c_e(R) = c$, which means the left-hand side is ideally blocking and the right-hand side is ideally conducting. With the given boundary conditions, charges will form the space charge layer at the cathode surface, nevertheless, no charge accumulation at the right-hand side of the solid-state electrolyte, as shown in Fig. 6.1a. A similar impedance analysis can be applied to the electrolyte surface if it is included.

6.1.3 Equivalent Circuit Model and Element Quantification

The MPNP-FBV model and the numerical methodology for the battery impedance calculation are comprehensive and fully based physical chemistry. Nevertheless, the complete impedance from such an electrochemical model is difficult to distinguish the contribution of each part and consumes the computation resources as well. Thereby, an equivalent circuit model for ASSBs is derived here based on the electrochemical model. The derived model is depicted in Fig. 6.1b and reflects the impedance spectroscopy contribution of individual component and interface.

In batteries, charges prone to accumulate or deplete at the interface and form the space charge layer, while lithium-ion concentrations remain almost homogeneous in the bulk. We first derive the bulk impedance of ASSBs [161]

$$R_i^{bu} = \int_0^{L_i} \frac{RTL_i}{z^2 F^2 AD_i^{bu} c_i^{bu}} \quad C_i^{bu} = A \frac{\varepsilon_0 \varepsilon_i}{L_i}, \quad (6.10)$$

where R_i^{bu} is the bulk resistance, C_i^{bu} indicates the bulk capacitance, and L_i is the corresponding thickness of the component. As mentioned that lithium-ion migration in solids strongly relies on hopping through the vacancies, thus, the stoichiometry effect plays an important role in the battery impedance. Under this circumstance, the chemical capacitance C_i^δ [113, 162] is included in the proposed equivalent circuit model and is defined as

$$C_i^\delta = \frac{c_{max}(zF)^2 AL_i}{RT} \left[\frac{1}{\tilde{c}_i(1 - \tilde{c}_i)} \right]. \quad (6.11)$$

According to Chap. 5, the analytical concentration distribution of the MPNP model can be expressed as

$$c_i = \frac{c_i^{bu} e^{-zF(\Phi - \Phi_i^{bu})/RT}}{1 + \tilde{c}_i^{bu} [e^{-zF(\Phi - \Phi_i^{bu})/RT} - 1]} \quad (6.12)$$

where Φ_i^{bu} and c_i^{bu} denote the electrostatic potential and the concentration in the bulk, respectively. In this study, electrons are assumed immobile to simplify the numerical calculation, i.e., $D_{c,-} = D_{e,-} = 0$. Based on Eq. (6.8), the analytical electric field can be resolved and leads to

$$E = \sqrt{\frac{2RTc_{max}}{\varepsilon_0\varepsilon_i} \ln \left\{ 1 + \tilde{c}_i^{bu} [e^{-zF(\Phi - \Phi_i^{bu})/RT} - 1] \right\}} + \frac{2zFc_{max}\tilde{c}_i^{bu}(\Phi - \Phi_i^{bu})}{\varepsilon_0\varepsilon_i}. \quad (6.13)$$

The space charge layer capacitance is related to the charge density [72] and the analytical solution is defined as

$$C = -\frac{\partial Q}{\partial \Phi} = \pm A \frac{F c_{max} \frac{-z\tilde{c}_i^{bu} e^{-zF(\Phi - \Phi_i^{bu})/RT}}{1 + \tilde{c}_i^{bu} [e^{-zF(\Phi - \Phi_i^{bu})/RT} - 1]} + F \tilde{c}_i^{bu} c_{max}}{\sqrt{\frac{2RTc_{max}}{\varepsilon_0\varepsilon_i} \ln \left\{ 1 + \tilde{c}_i^{bu} [e^{-zF(\Phi - \Phi_i^{bu})/RT} - 1] \right\}} + \frac{2F(\Phi - \Phi_i^{bu})\tilde{c}_i^{bu}c_{max}}{\varepsilon_0\varepsilon_i}} \quad (6.14)$$

Where, Q is the charge density in the space charge layer and is given by $Q = AE\varepsilon_0\varepsilon_i$. As depicted in Eq. (6.14), the analytical capacitance is closely related to the bulk electrostatic potential Φ_i^{bu} . Moreover, we can notice that the bulk electrostatic potentials are determined by lithium-ion kinetic reaction at the interface and are difficult to identify. Therefore, Eq. (6.14) is rarely adopted in the equivalent circuit models available in the literature when discussing the space charge layer capacitance. Instead, Eq. (6.15) has been extensively applied [95]

$$C_i^{in,*} = A \frac{\varepsilon_0\varepsilon_i}{\lambda_D} = A \sqrt{\frac{F^2\varepsilon_0\varepsilon_i \sum z^2 c_i}{RT}}, \quad (6.15)$$

where λ_D denotes the Debye length. This formula provides an easy way to calculate the space charge layer capacitance. But, it is less accurate than Eq. (6.14) because the influence of lithium-ion kinetic reaction is ignored in Eq. (6.15). The objective of this work is to investigate ASSBs impedance by considering the reaction kinetics. Therefore, Eq. (6.14) has been employed to calculate the space charge layer capacitance. The bulk electrostatic potential Φ_i^{bu} in the corresponding component is obtained from the numerical results of the electrochemical model, as explained in Chap. 4. Additionally, a simple approach to identify the electrostatic potential Φ_i^{bu} from material properties is also proposed, by utilizing the free enthalpy difference. Because the total potential drop is equal to the free enthalpy difference and more details can be found in Sec. 6.2.2.

The charge transfer resistance R_{ct} and the space charge layer capacitance can be calculated from Eqs. (6.5) and (6.14) as explained in the previous subsection. Based on Fig. 6.1b and the analytical results, the impedance of the proposed equivalent circuit model are given by

$$Z_c = \frac{1}{\underbrace{j\omega C_c^{bu} + \frac{1}{R_c^{su} + R_c^{bu} + 1/(j\omega C_c^{su}) + 1/(j\omega C_c^\delta)}}_{Z_c^{bu}}} + \frac{1}{\underbrace{j\omega C_c^{in} + 1/(R_{c,ct} + R_c^{in})}_{Z_c^{in}}} \quad (6.16)$$

$$Z_e = \frac{1}{\underbrace{j\omega C_e^{bu} + \frac{1}{R_e^{bu} + 1/(j\omega C_e^\delta)}}_{Z_e^{bu}}} + \frac{1}{\underbrace{j\omega C_e^{in} + 1/(R_{e,ct} + R_e^{in})}_{Z_e^{in}}} \quad (6.17)$$

$$Z = Z_c + Z_e. \quad (6.18)$$

In particular, C_c^{in} and C_e^{in} are the space charge layer capacitance at the interface, and C_c^{su} attributes to the charge accumulation at the cathode surface. R_c^{su} and R_i^{in} are the space charge layer resistances of the cathode surface and the interface, respectively. The charge transfer resistance in the cathode (or the electrolyte) is proportional to the concentration and is depicted by

$$R_{ct,i} = R_{ct}\tilde{c}_i/(\tilde{c}_c + \tilde{c}_e) \quad (6.19)$$

where R_{ct} is defined in Eq. (6.5).

6.2 Results and Discussion

The numerical methodology of impedance calculation based on the electrochemical model and the derived equivalent circuit model presented in Sec. 6.1 are both comparatively applied in this section for specific cases and parameter studies. The calculated impedance evolutions of the main electrochemical parameters are given here and show the applicability of impedance models. To make the problem mathematically tractable, several additional assumptions and boundary conditions follow literature has been adopted in this work. (1) The cathode/solid-state electrolyte half cell, as shown in Fig. 6.1a, is regarded as a one-dimensional domain and operated with an alternating current (ac) potential perturbation in the frequency range. (2) Only mobile lithium-ions are considered in the half cell, and electrons are assumed immobile. Moreover, lithium-ion reaction only happens at the interface. (3) The perturbation potential for ASSBs are expressed as $\Phi_c(L) = \Phi_{dc} + \Phi_{ac}(e^{j\omega t})$ and $\Phi_c(R) = 0$, respectively. (4) Heat generation is ignored and the temperature is uniform and constant in the half cell. Numerical simulation has been performed with the finite element method in the MOOSE framework with 2000 first-order bulk elements [145]. In particular, finite element interface elements between the components are subjected to the FBV model, while in the infinite element bulk elements the MPNP equations for individual component are solved. Moreover, to improve the convergence of numerical calculation, normalization of the model is carried out by using the following dimensionless parameters indicated by the tilde hat.

$$\tilde{L} = \frac{L}{L_0} \quad \tilde{t} = \frac{t}{t_0} \quad \tilde{c} = \frac{c}{c_{max}} \quad \tilde{\Phi} = \frac{F}{RT}\Phi \quad \tilde{D} = \frac{t_0}{L_0^2}D \quad \tilde{\omega} = t_0\omega \quad (6.20)$$

L_0 and t_0 are the normalization parameters and are given by 1 nm and 10^{-6} s, respectively.

Parameter	Unit	Value	Description
L_e	nm	50	Thickness of the electrolyte (LiPON) ^a
L_c	nm	50	Thickness of the cathode (LiCoO ₂) ^a
λ_s	nm	0.3	Thickness of the Stern layer ^b
D_c	m ² s ⁻¹	10^{-14}	Diffusivity of lithium ions in the cathode ^a
D_e	m ² s ⁻¹	10^{-14}	Diffusivity of lithium ions in the electrolyte ^b
ΔG_c^\ominus	eV	0.5	Standard activation energy barrier
ΔG_e^\ominus	eV	0.8	Standard activation energy barrier
ϵ_0	F m ⁻¹	8.85×10^{-12}	Vacuum permittivity
ϵ_e	-	80	Relative permittivity in the electrolyte ^a
ϵ_c	-	80	Relative permittivity in the cathode ^a
c_{max}	mol m ⁻³	10^4	Maximum lithium ions concentration ^a
c_e	mol m ⁻³	5×10^3	Initial concentration in the electrolyte ^a
c_c	mol m ⁻³	5×10^3	Initial concentration in the cathode ^a
β	-	0.5	Symmetry factor ^b
F	C mol ⁻¹	96 485	Faraday constant
T	K	298.15	Temperature
R	J mol ⁻¹ K ⁻¹	8.314	Gas constant
z_+	-	1	Lithium ion valence
z_-	-	-1	Electron valence
K_o	m ⁴ mol ⁻¹ s ⁻¹	100	Oxidation reaction rate ^a
K_r	m ⁴ mol ⁻¹ s ⁻¹	100	Reduction reaction rate ^a
A	m ²	10^{-4}	Geometrical surface ^a

TABLE 6.1 ^aDesigned parameters and ^bparameters are taken from Landstorfer, Okubo and Mei separately et al. [94, 130, 131]

6.2.1 EIS Current

To better understand the impedance calculation by using the MPNP-FBV model, the resulting current as a function of time is plotted here. The total electric current I is composed of the faradaic current I_f and the maxwell displacement current I_d , which is expressed as $I = I_f + I_d$. The faradaic current attributes to the species migration and is given by $I_f = FA \sum_i z_i J_i$. The maxwell displacement current results from the frequency of the electric field strength and is $I_d = -A\epsilon_0\epsilon_i[\partial(\nabla\Phi)/\partial t]$. In this work, the dimensionless alternate-current potential at the left-

hand side leads to $\tilde{\Phi}_{ac} = 0.01$ and the direct-current potential is $\tilde{\Phi}_{dc} = 0$, and other parameters are taken from Tab. 6.1.

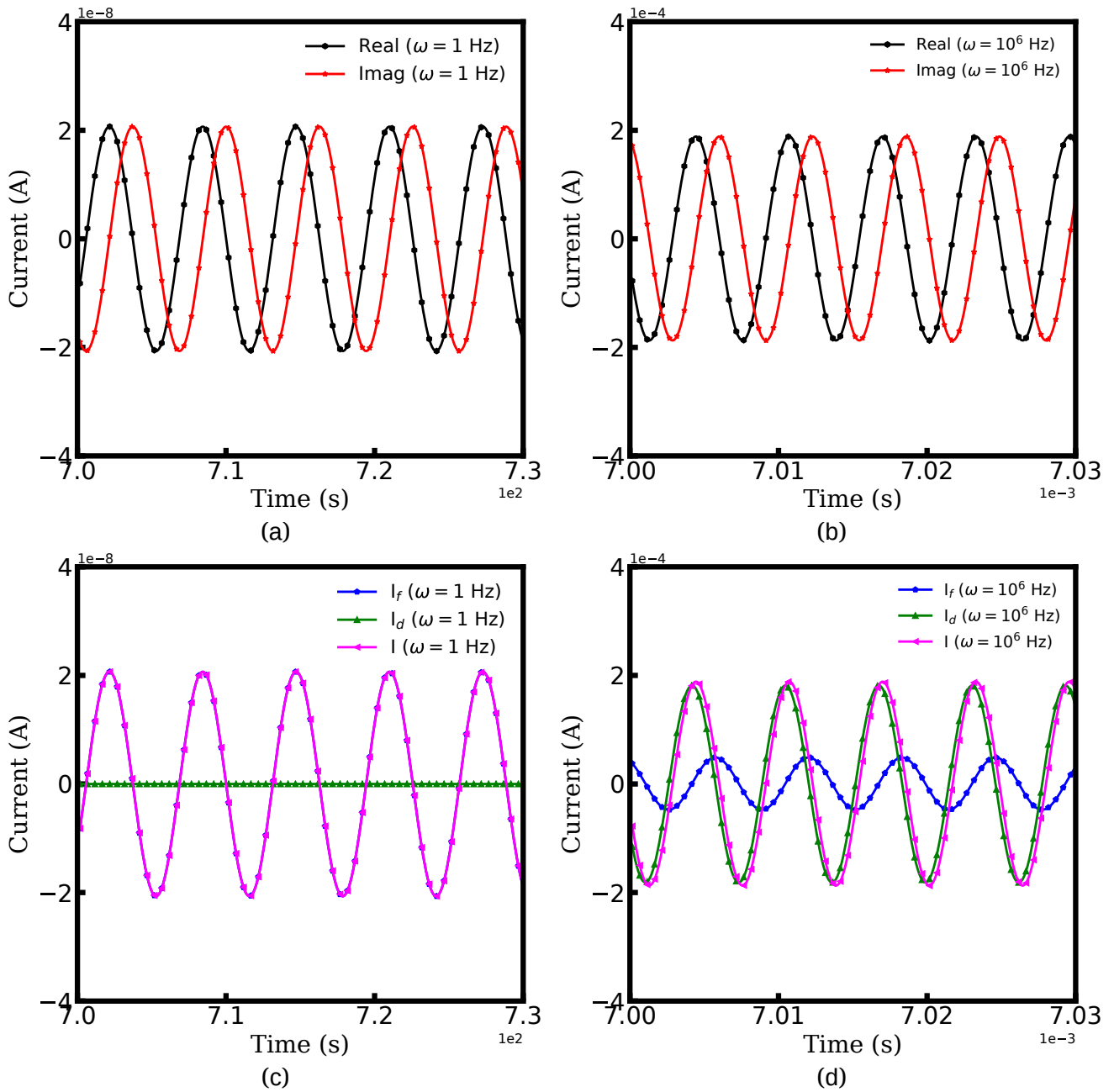


FIGURE 6.2 (a, b) The real and imaginary currents of ASSBs at specific frequencies. (c, d) The faradaic, displacement and total currents at different frequencies.

Fig. 6.2 depicts the resulting currents of the half cell as a function of time at two specific frequencies, i.e., $\omega = 1$ and 10^6 Hz. The legend “Real” and “Imag” indicate the real and the imaginary parts of the total current, respectively. Note that the half cell reaches a quasi-equilibrium

state with the perturbation potential, and the amplitude of the resulting current is utilized for the battery impedance calculation, as shown in Eq. (6.9). From Figs. 6.2a and 6.2b, we can conclude that the amplitude of current increases with the frequency increasing. Therefore, this conclusion can explain that the impedance magnitude of batteries decreases at high frequencies [96].

Moreover, to identify the impedance contribution, the Faradaic current I_f and the maxwell displacement I_d current are shown in Figs. 6.2c and 6.2d, as well as the total current I . At the frequency $\omega = 1$ Hz, the displacement current equals zero and the plots of the Faradaic current and the displacement current appear to be superimposed here. Results show that the impedance associated with lithium-ion migration plays an important role at low frequencies. However, at the high-frequency region, the maxwell current increases while the Faradaic current decreases, which means that the applied potential plays a more important role. The reason attributes that lithium-ion cannot migrate inside materials because of the rapid frequency change. Therefore, solid-state batteries prone to exhibit dielectric properties at high frequencies.

6.2.2 Charge Transfer Resistance with Dependency on the Free Enthalpy Difference

In this section, the kinetics of lithium-ion reaction is discussed from the fundamental point of view. The related thermodynamic properties of the electrode/electrolyte interface are shown in Fig. 6.1c, and the actual free enthalpy G_i of material is expressed by

$$G_i = G_i^\ominus + \frac{RT}{F} \ln \frac{\tilde{c}_i}{1 - \tilde{c}_i}, \quad (6.21)$$

G_i^\ominus is the standard free enthalpy and \tilde{c}_i denotes the normalized concentration. Thus, the free enthalpy difference of materials yields

$$\Delta G = G_c - G_e = G_c^\ominus - G_e^\ominus + \frac{RT}{F} \ln \frac{\tilde{c}_c}{1 - \tilde{c}_c} - \frac{RT}{F} \ln \frac{\tilde{c}_e}{1 - \tilde{c}_e}. \quad (6.22)$$

It should be noted that the standard free enthalpy difference $G_c^\ominus - G_e^\ominus$ numerically equals the standard activation energy difference $-(\Delta G_c^\ominus - \Delta G_e^\ominus)$. To investigate the influence of the free enthalpy difference on the charge transfer resistance, lithium-ion concentration and the standard activation energy are discussed here, respectively. The diffusion coefficients are $D_e = D_c = 10^{-14} \text{ m}^2 \text{ s}^{-1}$, and other parameters are shown in Tab. 6.1.

Fig. 6.3 plots the charge transfer resistance and the total electrostatic potential drop with respect to the free enthalpy difference, e.g., the state of charge and the standard activation energy. The charge transfer resistance is calculated by Eqs. (6.3) and (6.5), and the concentrations at the intrinsic equilibrium state are determined numerically by the MPNP-FBV model. The total electrostatic potential drop is equal to the difference of bulk potentials and is expressed

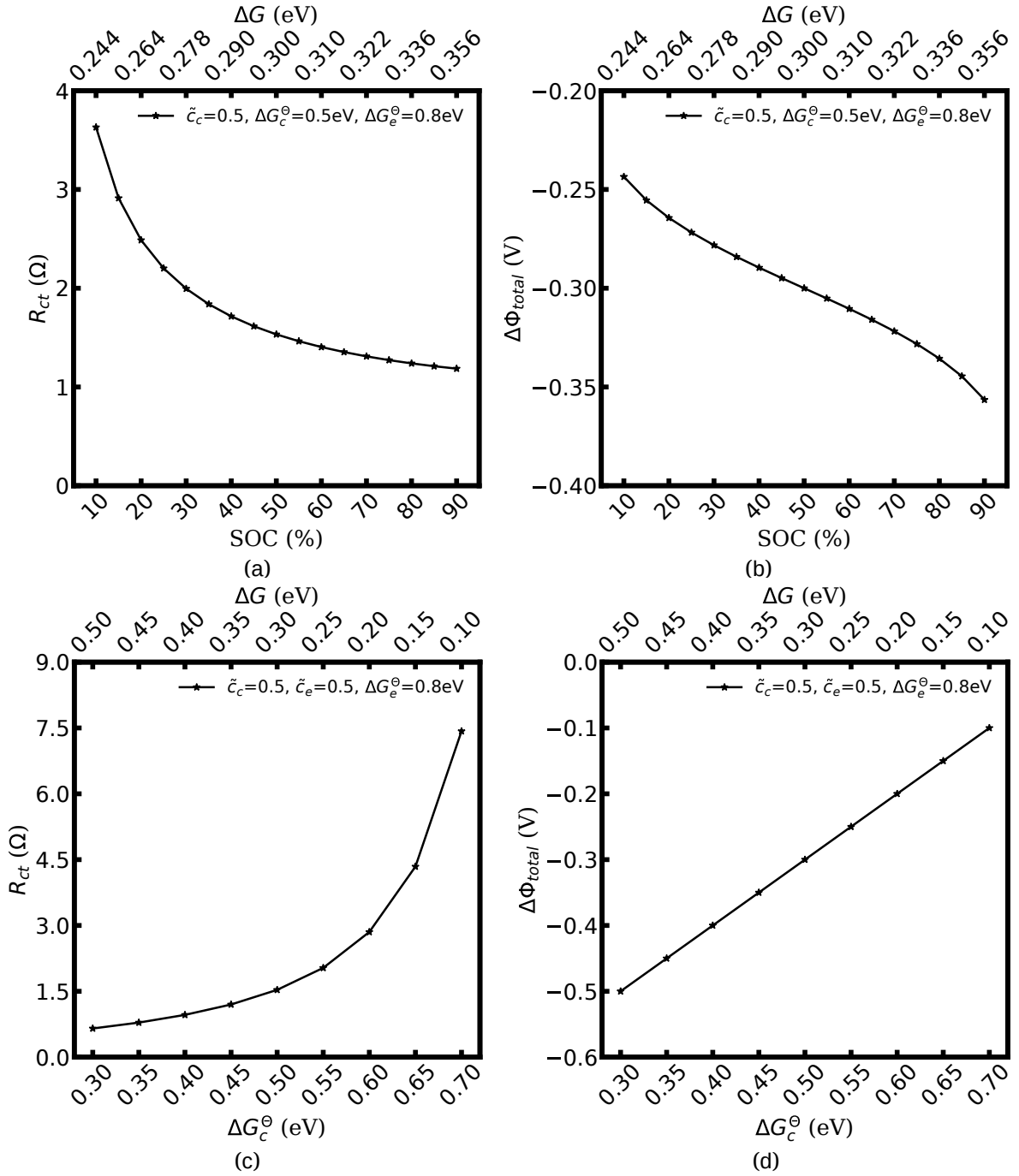


FIGURE 6.3 (a, b) The charge transfer resistance and the total electrostatic potential drop with different lithium-ion concentrations in the cathode. (c, d) The charge transfer resistance and the electrostatic potential drop with different standard activation energy barriers in the cathode.

by $\Delta\Phi_{total} = \Phi_c^{bu} - \Phi_e^{bu}$. In Figs. 6.3a and 6.3b, lithium-ion concentration of the solid-state electrolyte is $\tilde{c}_e = 0.5$, and the standard activation energies are assumed to be $\Delta G_c^\ominus = 0.5$ eV and $\Delta G_e^\ominus = 0.8$ eV, respectively. It should be noted that the activation energies of materials can be identified through the DFT calculation [130]. The initial concentrations of the cathode are

$\tilde{c}_c = 0.1 \sim 0.9$, which represents the theoretical state of charge (SOC) varies from 10% to 90%.

Figs. 6.3c and 6.3d illustrate that lithium-ion concentrations are $\tilde{c}_c = \tilde{c}_e = 0.5$ and the electrolyte standard activation energy remains $\Delta G_e^\ominus = 0.8$ eV, while the cathode activation energy varies from $\Delta G_c^\ominus = 0.3 \sim 0.7$ eV. Here, the free enthalpy difference ΔG is calculated by Eq. (6.22), Figs. 6.3a and 6.3c show that the charge transfer resistance decreases with increasing free enthalpy difference. In addition, references [163, 164] show that the charge transfer resistance decreases with increasing concentration and verify the numerical results. Furthermore, Figs. 6.3b and 6.3d plot the total electrostatic potential drop as a function of the free enthalpy difference. Results demonstrate that the potential drop equals to the free enthalpy difference, i.e., $|\Delta\Phi_{total}| = \Delta G$. It is evident that increasing the free enthalpy difference can significantly reduce the charge transfer resistance. Nevertheless, increasing the large free enthalpy difference also leads to a large electrostatic potential drop at the interface, which is harmful to the working potential. Therefore, the free enthalpy difference between the cathode and the electrolyte is a paradox criterion for high performance battery design and has to be optimized.

6.2.3 Influence of Standard Activation Energy on the Battery Impedance

Sec. 6.1.3 gives the analytical expressions for the equivalent circuit elements. Note that thereby the bulk electrostatic potential applied in Eq. (6.14) is still need to be determined. As demonstrated in Sec. 6.2.2, the total potential drop is associated with the free enthalpy difference. Therefore, the approach to identify the bulk electrostatic potential based on material properties is established in this section. Furthermore, the impedance spectroscopies of the half cell calculated by the MPNP-FBV model are also plotted to contrast the analytical results.

The initial normalized concentrations are fixed at $\tilde{c}_c = \tilde{c}_e = 0.5$, and lithium-ion diffusion coefficients are $D_c = D_e = 10^{-14} \text{ m}^2 \text{ s}^{-1}$. The effect of the free enthalpy difference is assessed by performing simulation for the cathode standard activation energies are $\Delta G_c^\ominus = 0.5$ and 0.6 eV, while the electrolyte standard activation energy is given as $\Delta G_e^\ominus = 0.8$ eV. The considered frequency of the perturbation potential is from $1 \leq \omega \leq 10^6$ Hz, and other parameters are shown in Tab. 6.1. It should be noticed that 50 samples of the corresponding current are recorded. Therefore each point in the impedance curves denotes a specific frequency.

Figs. 6.4a to 6.4d depict the half cell impedance curves for the two different standard activation energies of the cathode, e.g., $\Delta G_c^\ominus = 0.5$ and 0.6 eV. The corresponding equilibrium states are shown in Figs. 6.5a to 6.5d. In the legend, “Num” denotes the impedance results calculated by the MPNP-FBV model, and “Equ” represents the analytical results estimated by the equivalent circuit model. Fig. 6.4a shows that the impedance plots of the half cell can be divided into “I” and “II” two regions, and the intersection points with the real impedance are denoted by “A” and “B”, respectively. In addition, “I” is the high-frequency region, and the impedance results in the

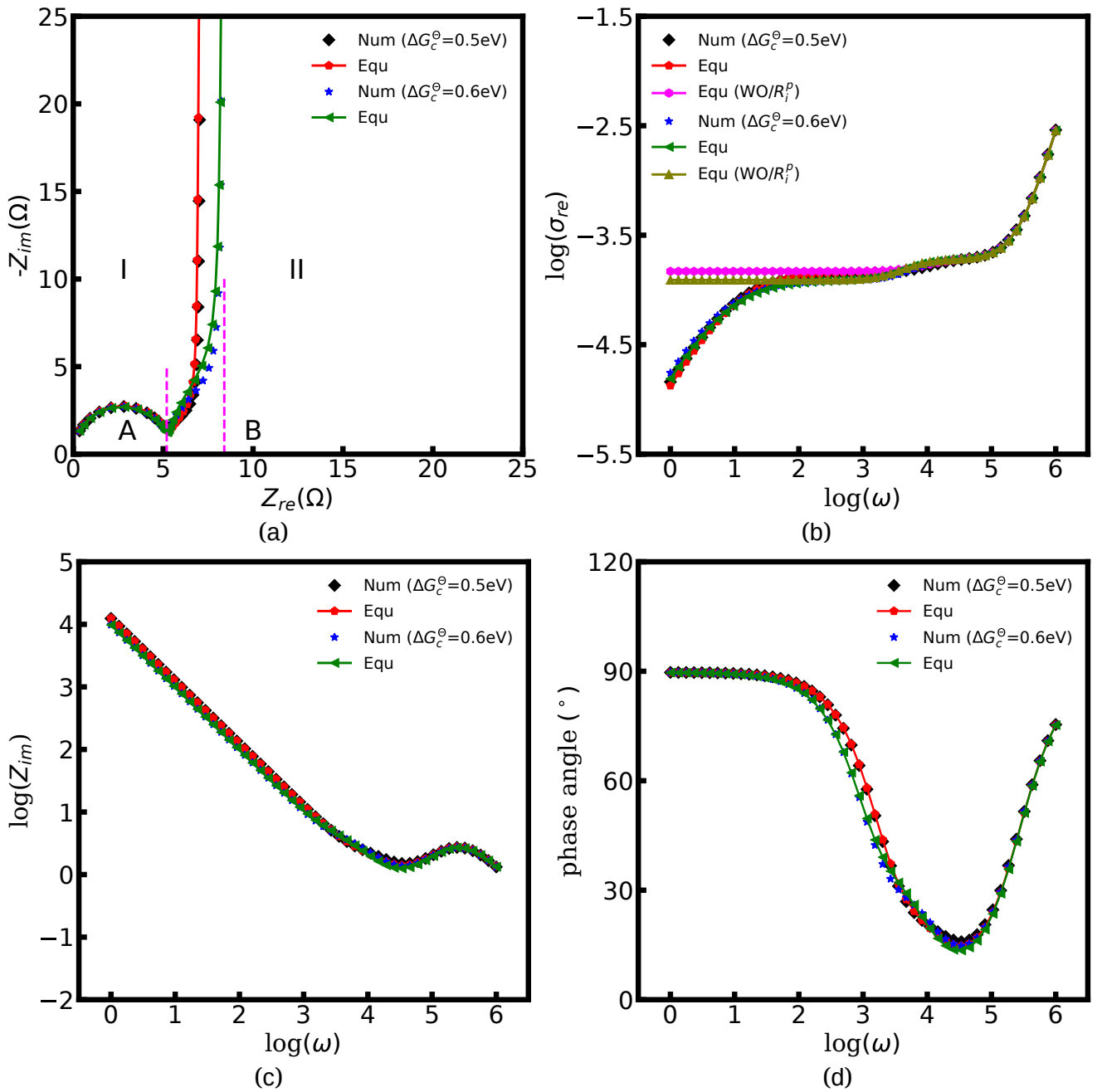


FIGURE 6.4 Numerical impedance curves of all-solid-state batteries with the different standard activation energies of the cathode, e.g., $\Delta G_c^\ominus = 0.5$ and 0.6eV . (a) The Nyquist plot, (b) the conductivity, (c) the imaginary Bode plot, and (d) the phase angle.

region “II” are calculated at the medium and low frequencies.

In the region “I”, the impedance curve shows an ideal semicircle and is assumed as a resistor in series with a capacitor [95]. It can be observed that the impedance plots are overlapped in the region “I” which means that the activation energy cannot influence the battery impedance at the

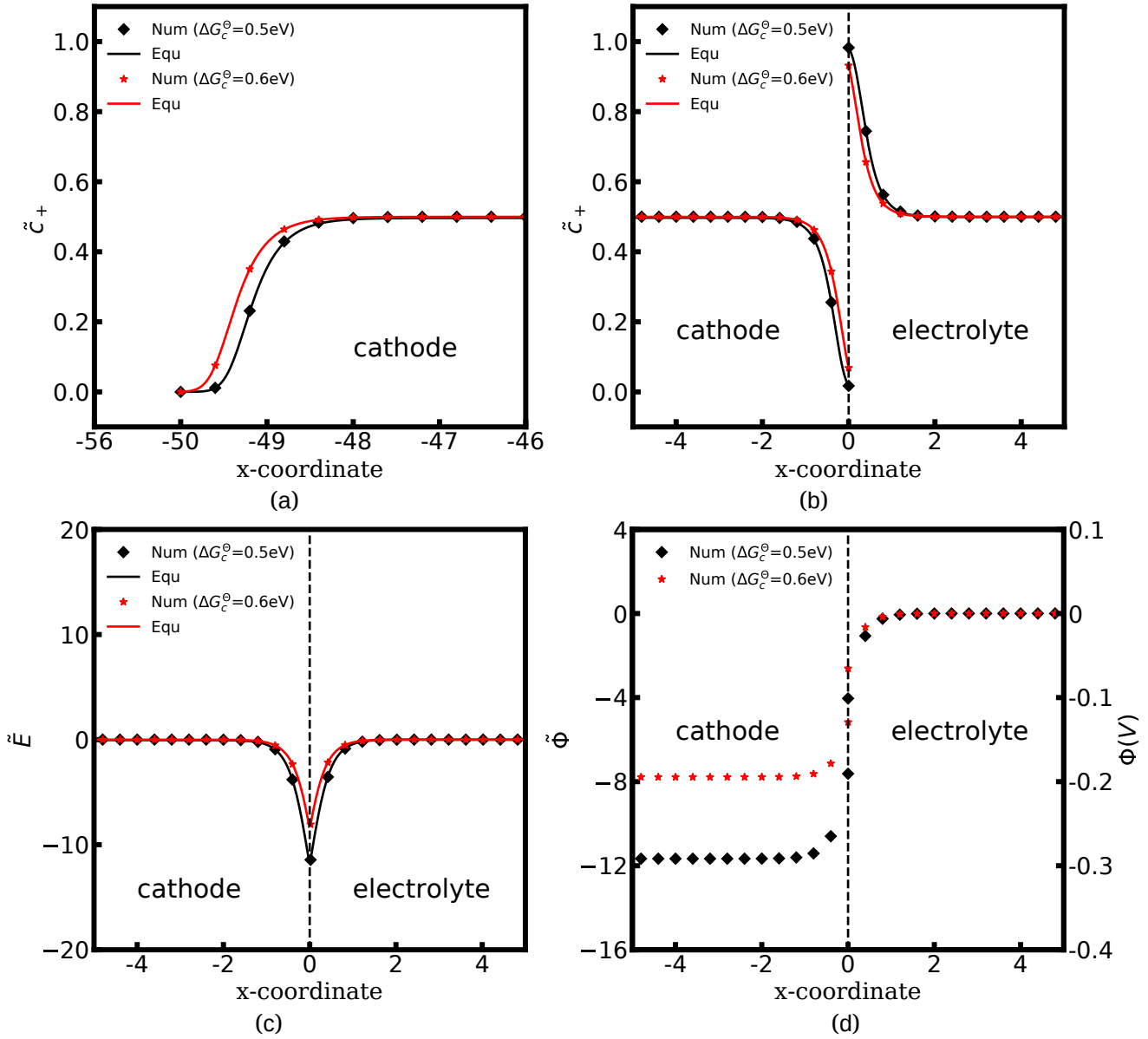


FIGURE 6.5 The corresponding equilibrium states: (a) the concentration distribution at the cathode surface, (b) the concentration, (c) the electric field, and (d) the electrostatic potential distributions at the cathode/electrolyte interface.

high-frequency region. According to the numerical calculation, the value of intersection point “A” is equal to 5.4Ω and the capacitance is calculated as $2.84 \times 10^{-6} \text{ F}$. Based on the analytical solution Eq. (6.10), the bulk impedance are $R_c^{bu} = R_e^{bu} = 2.66 \Omega$ and $C_c^{bu} = C_e^{bu} = 1.42 \times 10^{-6} \text{ F}$. Results indicate that the value of the intersection point “A” equals to the total bulk resistance, e.g., $R_c^{bu} + R_e^{bu}$, and the capacitance is associated with the bulk capacitor. From the discussion, it can be concluded that the region “I” in Fig. 6.4a is caused by the bulk impedance of batteries.

The region “II” contributes to the interface and surface impedance, and is regarded as a capacitor

in parallel with resistors and then in series with a capacitor. The shunt-wound resistors and the capacitor attribute to the cathode/electrolyte interface impedance, i.e., the charge transfer resistance, the interface space charge layer capacitance and the interface space charge layer resistance. As shown in Chap. 3, the Warburg impedance is also employed to explain that the space charge resistance, which is caused by the charge density perturbations. Therefore, both impedances are used to explain the same behaviour. The series-wound capacitor is explained by the space charge layer at the cathode surface, as illustrated in Fig. 6.1b. The discrepancy between the impedance curves in the region “II” indicates that lithium-ion kinetic reaction plays an important role in the charge transfer resistance.

From Fig. 6.4a, the charge transfer resistance can be read as $R_{ct} = 2.9 \Omega$ for the case $\Delta G_c^\ominus = 0.6 \text{ eV}$. The value of the intersection point “B” is 8.3Ω , and is equal to the total battery resistance, e.g., $R_{ct} + R_c^{bu} + R_e^{bu}$. A similar conclusion can be drawn when the standard activation energy is $\Delta G_c^\ominus = 0.5 \text{ eV}$. The space charge layer capacitances at the interface and the surface are calculated by Eq. (6.14). Thus, the bulk electrostatic potential plays an important role in the capacitance calculation. In this study, the standard activation energies are $\Delta G_c^\ominus = 0.5$ and 0.6 eV , $\Delta G_e^\ominus = 0.8 \text{ eV}$ and the concentrations are equal to $\tilde{c}_c = \tilde{c}_e = 0.5$. Based on Eq. (6.22), the free enthalpy differences are calculated as $\Delta G = 0.3$ and 0.2 eV , respectively. Moreover, the previous section indicates that the total electrostatic potential drop is equal to the free enthalpy difference, as shown in Figs. 6.3b and 6.3d. Therefore, the total electrostatic potential drops lead to $\Delta\Phi_{total} = -0.3$ and -0.2 V . With the boundary conditions, e.g., $\Phi_e^{bu} = 0$ and $\nabla\Phi_e^{bu} = 0$, the cathode bulk electrostatic potentials are $\Phi_c^{bu} = -0.3$ and -0.2 V . Referring to Eq. (6.14), the space charge layer capacitances at the interface are calculated as $C_c^{in} = C_e^{in} = 1.52 \times 10^{-4}$ and $1.90 \times 10^{-4} \text{ F}$, and the surface capacitances C_c^{su} as 8.03×10^{-5} and $1.02 \times 10^{-4} \text{ F}$, for the two cases $\Delta G_c^\ominus = 0.5$ and 0.6 eV , respectively. By using these results and Eq. (6.18), the analytical impedance spectroscopies are plotted and fit quite well with the numerical curves as predicted.

As shown in the citations [127, 165, 166] and Chap. 5, the space charge layer resistance plays an important role in the interface impedance. Moreover, the charge transfer resistance has to be taken into account when considering the interface reaction. Therefore, as illustrated in Fig. 6.1b, the real portion of the space charge layer impedance involves the charge transfer resistance and the space charge layer resistance. As shown in the reference [167], the space charge layer resistance is regarded as a constant ohmic resistance and is independent of lithium-ion concentration. However, as mentioned in Chaps. 3 and 5, the space charge layer resistance is associated with the charge density and is frequency-dependent. Therefore, Maier [126, 148] pointed out that the space charge layer resistance is caused by deviation from the bulk contribution and is expressed as

$$R_i^{in} = -\frac{2RT\lambda_D}{z_i^2 F^2 A D_i c_i^{bu}} \frac{2\theta}{1 + \theta} \quad (6.23)$$

The parameter θ , which is called degree of influence, and means the enrichment or depletion

effect on the charge carrier number in the space charge layer regions. During the impedance measurement a perturbation potential is applied. Hence, the charge accumulation or depletion θ and the space charge layer resistance are frequency-dependent. The diffusivity in Eq. (6.23) is taken as independent, nevertheless, lithium-ion diffusivity in the space charge layer relies on the concentration and differs from the bulk according to the study [81]. Therefore, to consider this effect, a frequency-dependent ohmic resistance has been employed in the proposed equivalent circuit model. Moreover, the cathode surface space charge layer resistance is also taken into consideration, and the total frequency-dependent resistance is expressed as $R_i^p = R_c^{in} + R_e^{in} + R_c^{su}$. Adjusting with numerical results, it can be found that $R_i^p = Z_{re}/\omega$, where ω indicates the applied frequency, and Z_{re} is the real impedance of battery system at $\omega = 1$ Hz. Fig. 6.4b shows the conductivities of ASSBs with the proposed frequency-dependent resistance. “Equ (WO/ R_i^p)” denotes the equivalent circuit model without the total space charge layer resistance. It can be concluded that the frequency-dependent ohmic resistance can explain the tail of material conductivity well at the low-frequency region, and this conclusion is also presented in our previous work [161]. As expected, the analytical imaginary portion of the complex impedance fits well with the numerical results, as depicted in Fig. 6.4c. Fig. 6.4d plots the phase angle as a function of the potential frequencies and shows the purely capacitive [96] of batteries at the low-frequency region. This is explained by the space charge layer formation at the cathode surface. Moreover, the phase angle increases at the medium and high frequencies, showing that more current flows through the displacement path and is also confirmed by Fig. 6.2d.

To explain the impedance results more clearly, the equilibrium states with the different standard activation energies are also presented in Figs. 6.5a to 6.5d. It depicts that the bulk concentrations remain $\tilde{c}_c = \tilde{c}_e = 0.5$ for both the standard activation energies $\Delta G_c^\ominus = 0.5$ and 0.6 eV. Therefore, we can conclude that the bulk resistance and the capacitance are not influenced by the activation energy, and the impedance results are also verified by the overlapped curves in the region “I”. However, the concentration distributions at the interface are different and indicates that the interfacial impedance of these two cases are different, as depicted in Fig. 6.5b. Hence, it can explain the diversity in the region “II” of Fig. 6.4a. Moreover, the similar conclusion about the cathode surface capacitance also can be drawn through Fig. 6.5a.

6.2.4 Influence of Concentration on the Battery Impedance

Eq. (6.22) indicates that the free enthalpy difference is determined by both the standard activation energy and the concentration. The influence of the standard activation energy on the half cell impedance has been studied in Sec. 6.2.3, thus, the impact of concentrations is discussed here. The electrolyte concentration remains $\tilde{c}_e = 0.5$, and the standard activation energy barriers are assumed $\Delta G_c^\ominus = 0.5$ eV and $\Delta G_e^\ominus = 0.8$ eV, respectively. Two cases with different normalized

lithium-ion concentrations in the cathode $\tilde{c}_c = 0.3$ and 0.5 are compared in this subsection.

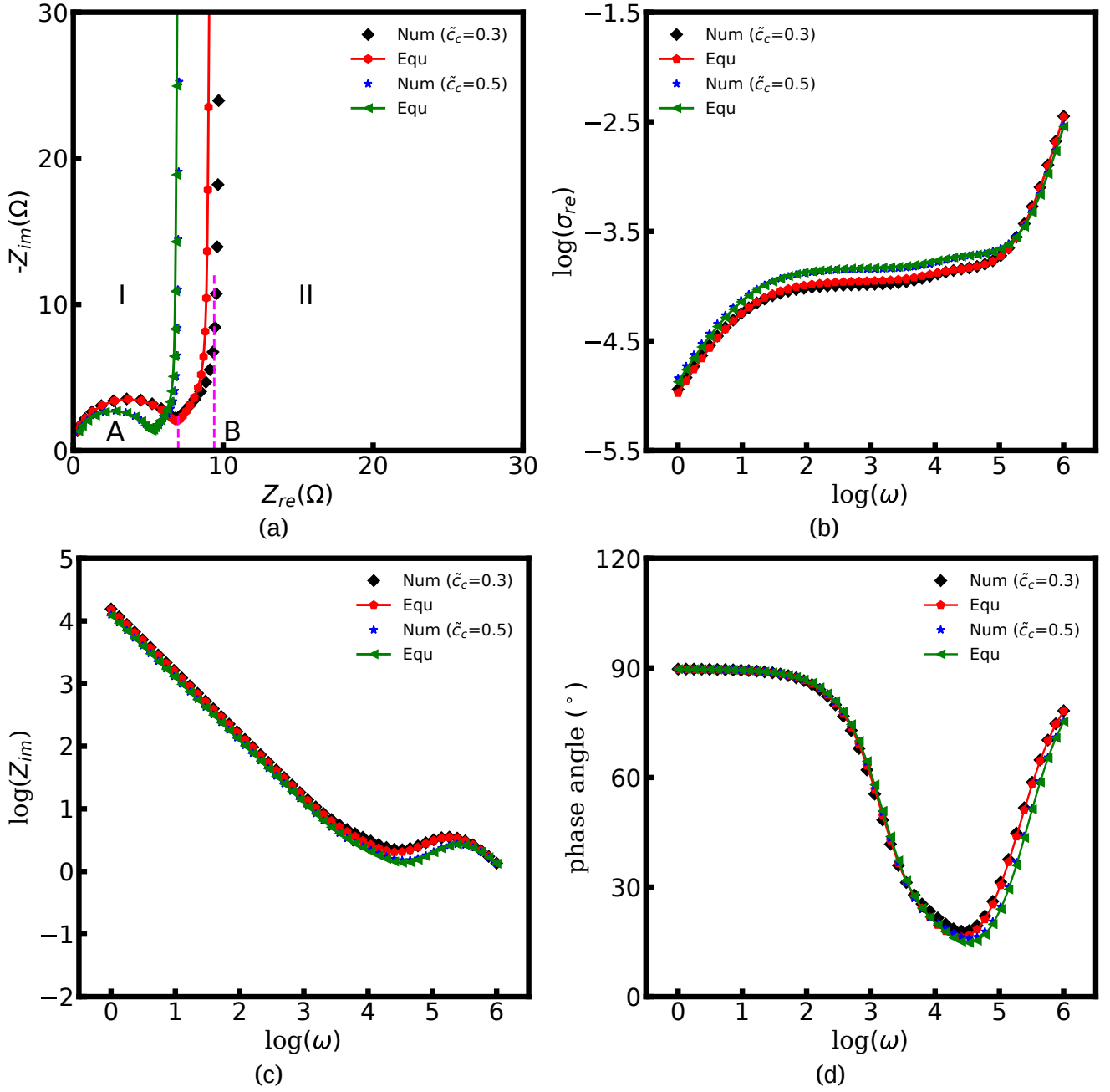


FIGURE 6.6 Numerical impedance curves of ASSBs for two cases with different concentration in the cathode, e.g., $\tilde{c}_c = 0.3$, and 0.5 . (a) the Nyquist plot, (b) the conductivity, (c) the imaginary Bode plot, and (d) the phase angle.

The impedance curves and the equilibrium states with different concentrations are contrasted in Fig. 6.6 for the two cases. Fig. 6.7a shows that the intersection point “A” of the semi-circle in the region “I” increases with concentration. This phenomenon can be explained by Eq. (6.10). The

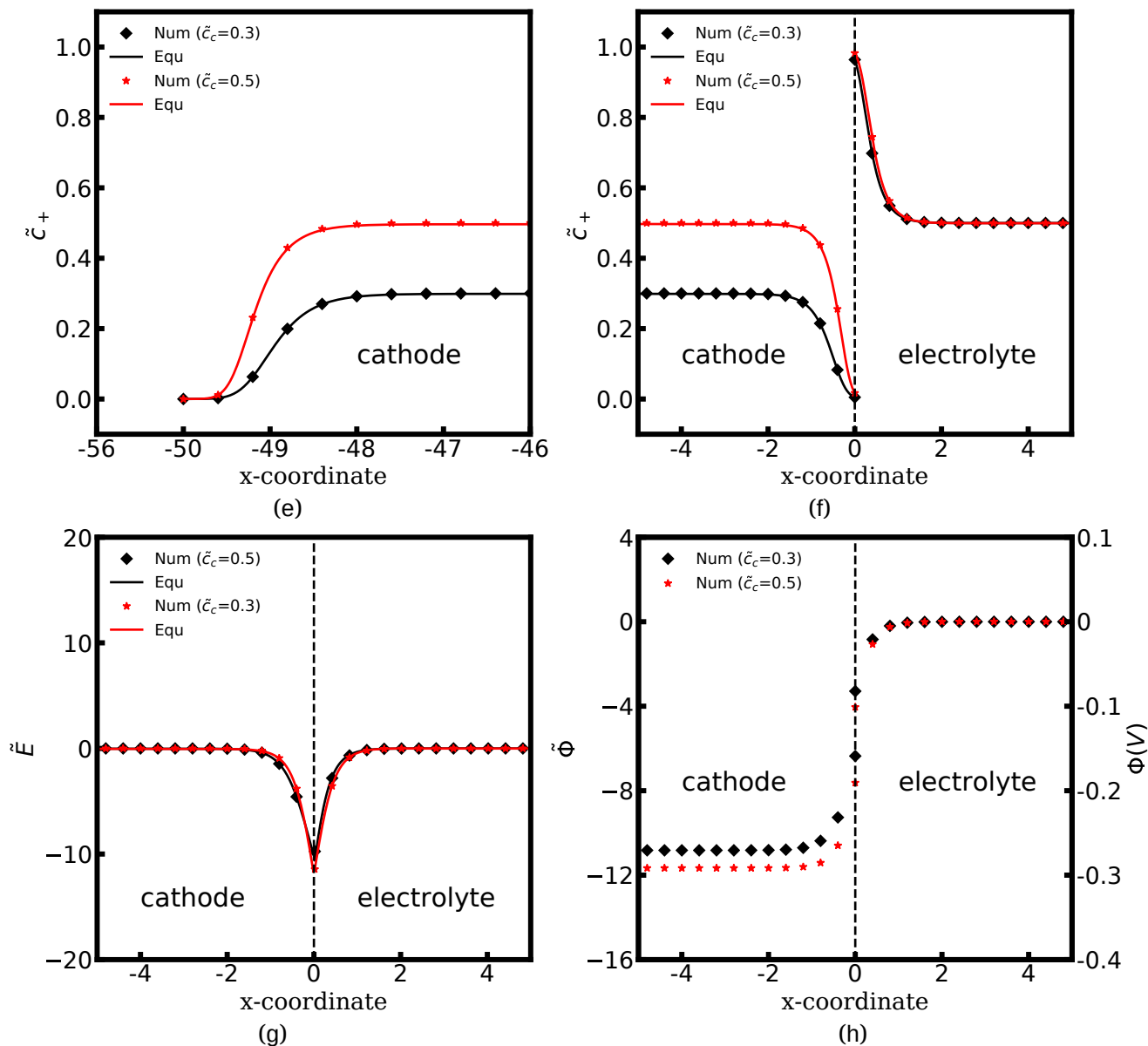


FIGURE 6.7 The corresponding equilibrium states: (e) the concentration distribution at the cathode surface, (f) the concentration, (g) the electric field, and (h) the electrostatic potential distributions at the cathode/electrolyte interface.

analytical results for the total bulk resistances $R_c^{bu} + R_e^{bu}$ are 7.1 and 5.4 Ω for $\tilde{c}_c = 0.3$ and 0.5, respectively. They are verified very well by the numerical results as shown in Fig. 6.6. In addition, the charge transfer resistances can be read out from the figure: $R_{ct} = 2$ and 1.53 Ω , which can be confirmed by the intersection point “B”. Referring to Eq. (6.22), the free enthalpy difference is obtained as $\Delta G = 0.278$ and 0.3 eV, respectively. Thus, the bulk electrostatic potential in the cathode at the equilibrium state should be $\Phi_c^{bu} = -0.278$ and -0.3 V, and the cathode surface

space charge capacitance is $C_c^{su} = 6.43 \times 10^{-5}$ and 8.03×10^{-5} F, respectively. The capacitance is calculated by $C = -\partial Q/\partial \Phi$, and is determined by the electric field and the charge density. As shown in Eq. (6.14), the space charge layer capacitance is related to the initial concentration. Thus, the analytical interfacial capacitances are $C_c^{in} = 1.08 \times 10^{-4}$ F and $C_e^{in} = 1.7 \times 10^{-4}$ F when the cathode concentration is $\tilde{c}_c = 0.3$. For the case $\tilde{c}_c = 0.5$, the charge densities are equal and the capacitances are calculated as $C_c^{in} = C_e^{in} = 1.51 \times 10^{-4}$ F. Comparison between Figs. 6.4 and 6.6 shows that lithium-ion concentration has relatively smaller influence on the interfacial impedance than the standard activation energy. Nevertheless, the concentration plays a comparatively more important role on the bulk resistance.

6.2.5 Influence of Diffusivity on the Battery Impedance

In previous sections, we give a specific investigation on the battery impedance spectroscopy with the free enthalpy difference, e.g., the standard activation energy and the concentration. In practice, increasing lithium-ion diffusivity, especially that of the electrolyte, is mostly the preferred attempt for researchers to develop high performance batteries. Therefore, a particular discussion on the interfacial impedance under different lithium-ion diffusivity constants is presented here. For the sake of simplicity, only ion diffusion coefficients of the electrolyte are regarded here, and two different cases with $D_e = 10^{-13}$ and 10^{-14} m² s⁻¹ are compared. The diffusivity of the cathode remains the same, i.e., $D_c = 10^{-14}$ m² s⁻¹, and the normalized concentrations are $\tilde{c}_c = \tilde{c}_e = 0.5$. In addition, the standard activation energies of both cases are assumed to be the same, more exactly, $\Delta G_c^\ominus = 0.5$ eV and $\Delta G_e^\ominus = 0.8$ eV.

Figs. 6.8a to 6.8d depict the impedance plots for the two cases with different lithium-ion diffusion coefficients of the solid-state electrolyte. The analytical impedance curves fit again very well with the numerical results and show the applicability of the proposed equivalent circuit model for all-solid-state batteries. Fig. 6.8a shows that the intersection point “A” decreases if the lithium-ion diffusivity is increased, while the charge transfer resistances of these two cases are numerically equal. By using Eq. (6.10), the electrolyte analytical bulk resistances are calculated as $R_e^{bu} = 0.27$ and 2.7Ω , for $D_e = 10^{-13}$ and 10^{-14} m² s⁻¹, respectively. Thus, the total bulk resistances are 2.97 and 5.4, and confirm the numerical results. Regarding the charge transfer resistance, it can be clearly explained by the half cell at the equilibrium state, as depicted in Figs. 6.9a to 6.9d. Results show that the charge density and the electrostatic potential are not influenced by lithium-ion diffusion coefficient. Therefore, the space charge layer resistance and the space charge layer capacitance remain the same for the two cases under comparison. From these results, it can be concluded that increasing lithium-ion diffusion coefficients may not help to reduce the interfacial impedance, but it can play an important role in the bulk resistance.

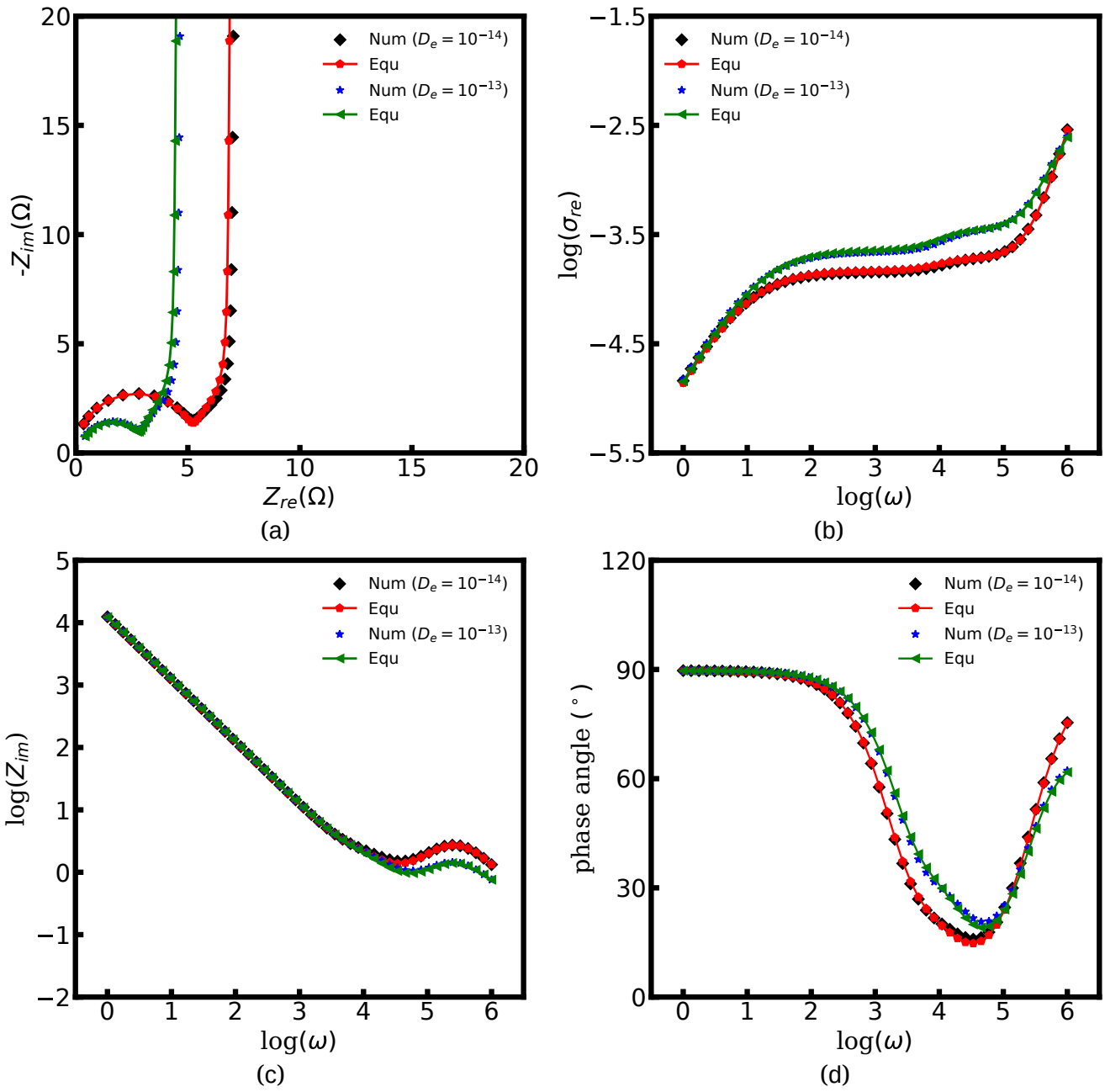


FIGURE 6.8 Numerical impedance curves of ASSBs with different diffusion coefficients of the electrolyte, e.g., $D_e = 10^{-14}$ and $10^{-13} \text{ m}^2 \text{ s}^{-1}$. (a) the Nyquist plot, (b) the conductivity, (c) the imaginary Bode plot, and (d) the phase angle.

6.2.6 Influence of Electrical Double Layer on the Battery Impedance

In this work, the electrostatic potential drop at the interface is modelled by the Gouy-Chapman-Stern formulation [68] or called the diffuse double layer model, i.e., $\Phi_c = \Phi_e - \vec{n}\lambda_s \nabla \Phi_c$. Under this circumstance, the electrostatic potential drops both in the diffuse layer and the Stern layer, and is in

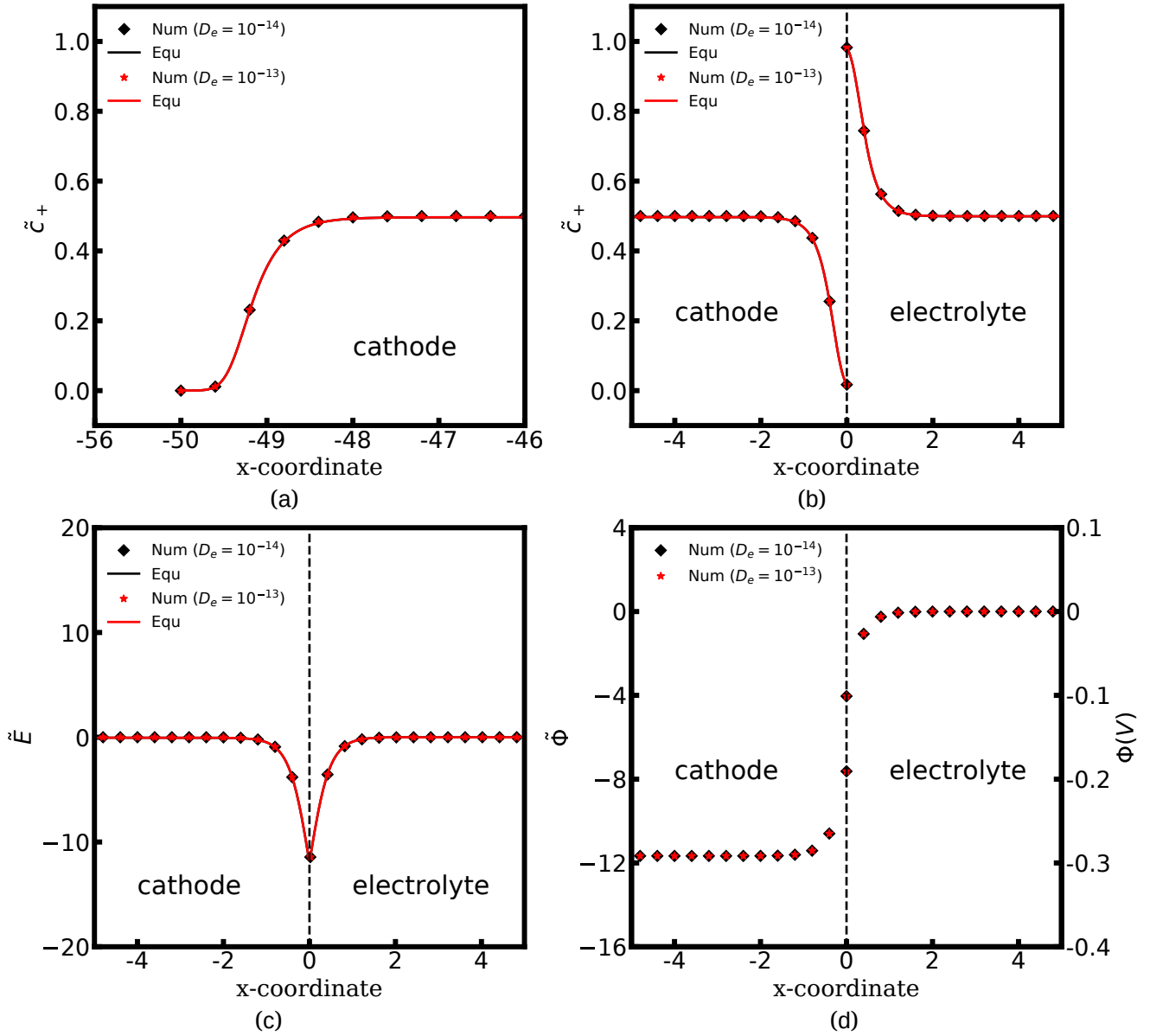


FIGURE 6.9 The corresponding equilibrium states: (e) the concentration distribution at the cathode surface, (f) the concentration, (g) the electric field, and (h) the electrostatic potential distributions at the cathode/electrolyte interface.

agreement with the experimental observations [70]. Nevertheless, the diffuse double layer model is utilized to explain the solution/solid interface and is still questionable for researchers to analyze the solid/solid interface. Therefore, to deeper the understanding of the interfacial impedance, the Helmholtz-layer model or called the compacted double layer model is also employed here to calculate the half cell impedance. With this assumption, the electrostatic potential only drops in the Stern layer, and the potential gradient equals zero in the diffuse layer, i.e., $\nabla\Phi_c = \nabla\Phi_e = 0$. To focus on the interface structure, lithium-ion concentrations of the cathode and the electrolyte

are $\tilde{c}_c = \tilde{c}_e = 0.5$, and the diffusion coefficients equal to $D_c = D_e = 10^{-14} \text{ m}^2 \text{ s}^{-1}$. Furthermore, the standard activation energies are given as $\Delta G_c^\ominus = 0.5 \text{ eV}$ and $\Delta G_e^\ominus = 0.8 \text{ eV}$.

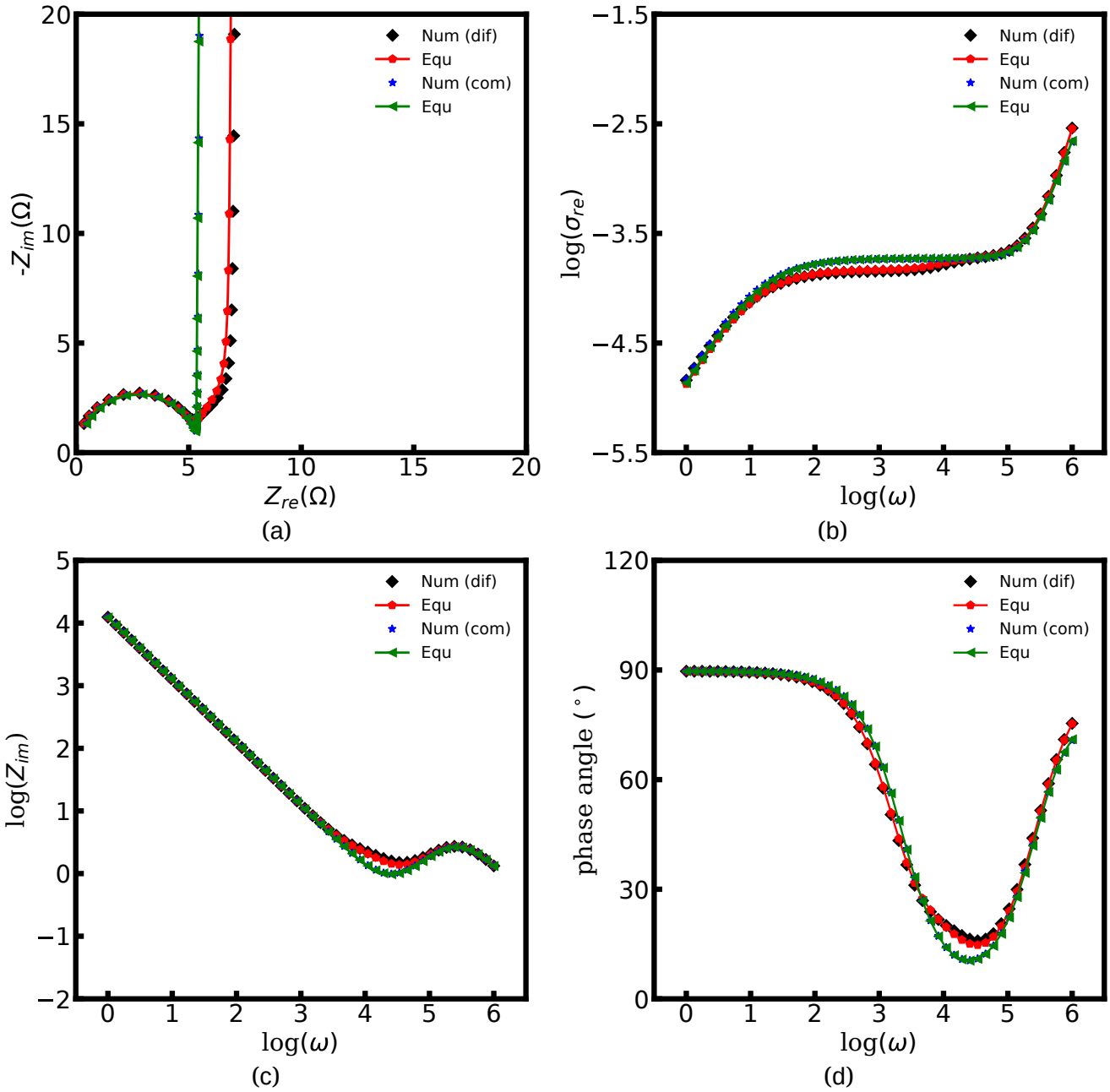


FIGURE 6.10 Numerical impedance curves of all-solid-state batteries with the different electrical double layer structures, e.g. the diffuse double layer model and the compact double layer. (a) the Nyquist plot, (b) the conductivity, (c) the imaginary Bode plot, and (d) the phase angle.

Figs. 6.10a to 6.10d present the half cell impedance spectroscopies for the above two cases, namely the diffuse double layer model and the compact double layer model. Note that the analytical results fit well with the numerical results based on the electrochemical model, and

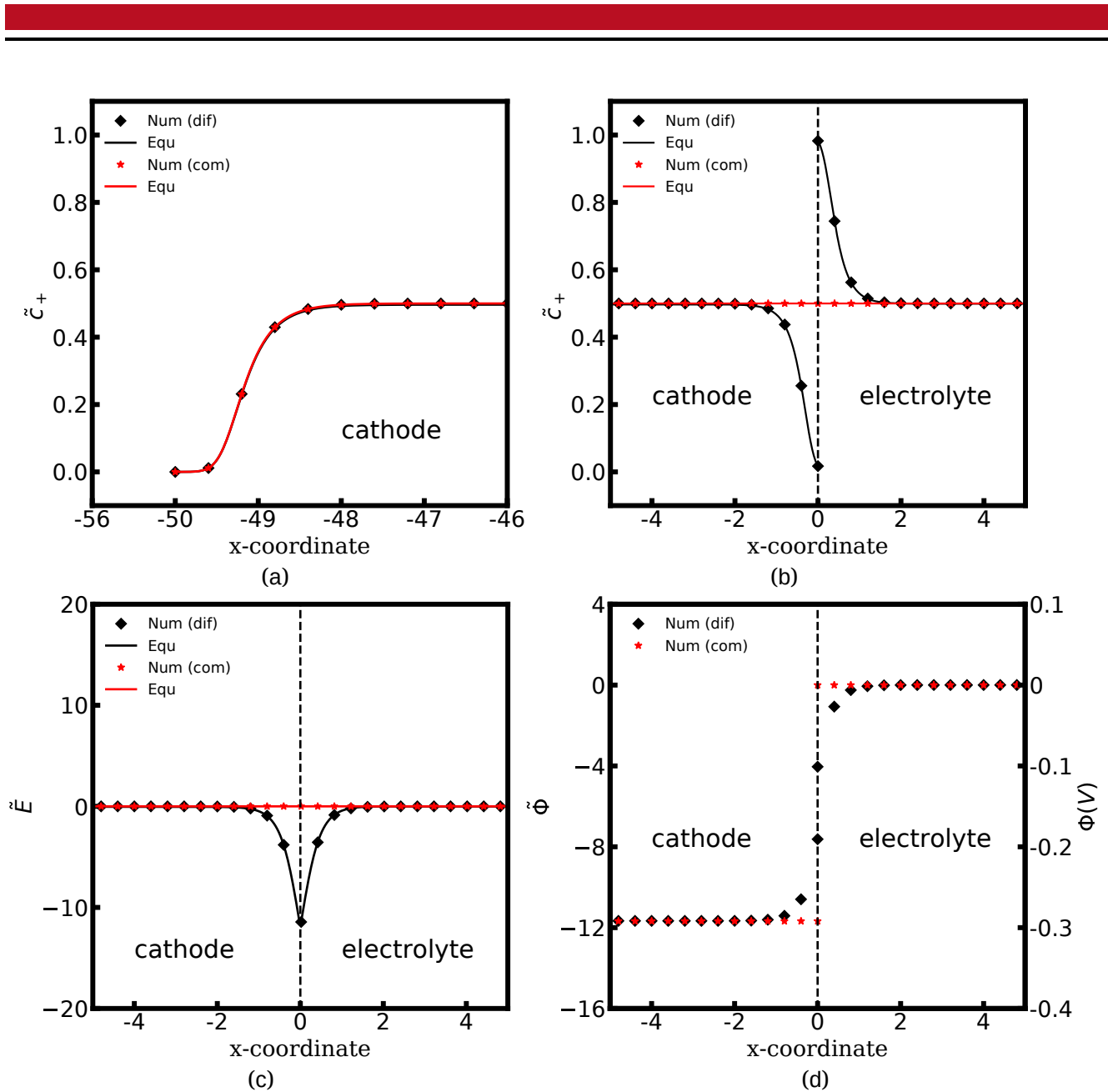


FIGURE 6.11 The corresponding equilibrium states: (e) the concentration distribution at the cathode surface, (f) the concentration, (g) the electric field, and (h) the electrostatic potential distributions at the cathode/electrolyte interface.

confirms the applicability of the proposed equivalent circuit model. As shown in Fig. 6.10a, the Nyquist plots nearly overlap on the same line in the region “I” regardless of the electrical double layer (EDL) structure changes. In other words, the interface structure has no significant effects on the impedance plots at medium and high frequencies. By contrast, it is interesting that the semicircle caused by the charge transfer resistance and the interfacial capacitance in the region “II” vanishes in the compact double layer model. To further explore the reason for this phenomenon, the concentration and the potential distributions at the intrinsic equilibrium state are plotted.

Fig. 6.11b depicts that no charge density formation or depletion appears at the interface in the case of the compact double layer structure. The space charge layer capacitance is associated with the redox reaction and is determined by the charge density, referring to Eq. (6.14). Thus, the interfacial capacitance C_i^{in} can be ignored under this circumstance. The charge transfer resistance with the diffuse double layer structure equals to $R_{ct} = 1.53 \Omega$ and is much larger than that of the compact double layer case, i.e., $R_{ct} = 0.10 \Omega$. The surface concentration distributions with the different EDL structures appear to be superimposed in Fig. 6.11a and indicates that the surface capacitance C_c^{su} is not influenced by the EDL structure when the material thickness is much larger than the surface space charge layer, i.e., $L_s \ll L$. Based on these results, we can conclude that ASSBs with a large potential drop in the Stern layer lead to a relatively high charge transfer resistance and the space charge layer capacitance.

6.2.7 Experimental Verification of Charge Transfer Resistance

The electrochemical MPNP-FBV model and the corresponding equivalent circuit model for ASSBs impedance calculation are introduced in the above sections. Nevertheless, the experimental impedance spectroscopy of half cell is hard to find and verify with the numerical results. Thus, we just take the LiFePO_4 cathode as an example and confirm the charge transfer resistance caused by the reaction kinetics. Noted that the corresponding experimental data are taken from the reference [163] at different temperature and state-of-charge (SOC). For the simulation, the activation energy is assumed to be $\Delta G_c = 0.4 \text{ eV}$ along the b-channel of the pure LiFePO_4 surface. It should be noted that the values of the activation energy of LiFePO_4 are still controversial, and the reported values span over a wide range [168–172]. Moreover, the electrolyte activation energy is assumed as $\Delta G_e = 0.8 \text{ eV}$.

Fig. 6.12 shows the charge transfer resistance curves of the experimental and numerical results. As shown in Figs. 6.12a and 6.12b, R_{ct} decreases with increasing battery temperature or increasing SOC. The same tendency is also observed in our numerical results. More specifically, the experimental value of the charge transfer resistance at 318 K is reduced to 1/10 of that at 278 K, and the measured R_{ct} at SOC of 90% decreases to 1/3 of that at 10%. As it can be seen, the calculated charge transfer resistance at SOC = 10% and SOC = 90% reads $R_{ct} = 1.53 \text{ m}\Omega$ and $0.41 \text{ m}\Omega$, respectively. In other words, the similar conclusions can also be derived from our numerical model. Because of the ideal assumption and the realistic situation, the calculated results show deviations at certain points from the corresponding experimental data, particularly at 278 K. The reason attributes parameters deviations at different temperatures such as the permittivity. Nevertheless, it is still sufficient to demonstrate the applicability of the MPNP-FBV model for the charge transfer resistance calculation.

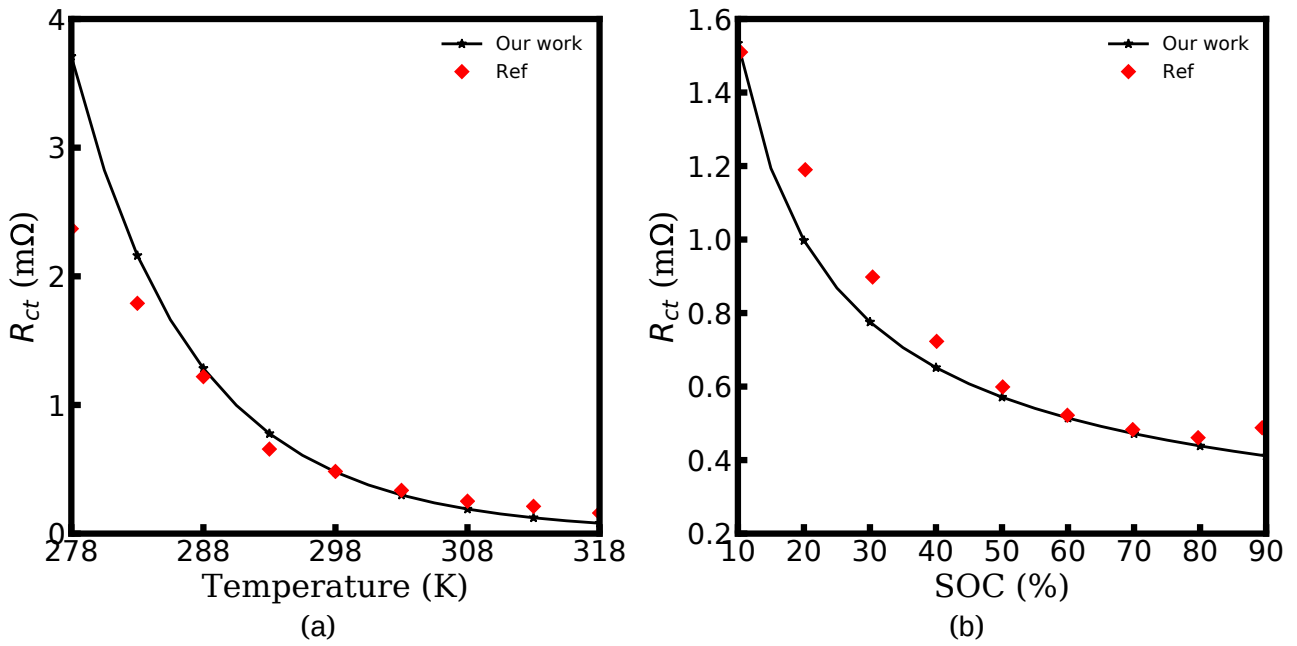


FIGURE 6.12 The charge transfer resistance R_{ct} at different temperature and state of charge. (a, b) The experimental data, and (c, d) the numerical results from the MPNP-FBV model. Reproduced with permission from Xueyuan Wang et al [163]. Copyright 2019 Elsevier

6.3 Concluding Remarks

In this project, we investigate ASSBs impedance by utilizing the electrochemical model (MPNP-FBV) and the corresponding equivalent circuit model. This new equivalent circuit model is derived from the electrochemical continuum model, and the elements in the circuit are characterized from fundamental material parameters and state variables. For the first time, lithium-ion kinetic reaction at the cathode/electrolyte interface is physically coupled in the proposed MPNP-FBV model to calculate the battery impedance. It enables us to estimate the battery impedance from fundamental material properties, e.g., the activation energy, the concentration, and the diffusivity. In addition, the comparison between the calculated and the measured charge transfer resistance of LiFePO_4 at different temperature and at different SOCs implies that the proposed equivalent circuit model is reliable.

Since the vacancy effect in solids is included in the MPNP-FBV model, we could obtain reasonable results on the concentration and the electrostatic potential distributions in the space charge layer region. In addition, we derived successfully the analytical results for the MPNP-FBV model. Thereafter, we take a further step and introduce a methodology to identify the bulk electrostatic potential which is critical for the space charge layer capacitance calculation. Thus, all the circuit elements in the proposed model are quantified based on the analytical solutions and stems closely from material properties. To deeper the understanding of battery impedance, the influence of

different material parameters on the battery impedance has been investigated. Results show that ASSBs with a large free enthalpy difference will lead to a large potential drop across the interface, and is unfavourable for battery application. Nevertheless, it has a low charge transfer resistance. On the other hand, increasing the electrolyte conductivity cannot help to reduce the interface impedance, but reduce the bulk resistance. Thereafter, different EDL structures have also been discussed comparatively in this work. It can be observed that the impedance associated with the space charge layer capacitance vanishes when the diffuse double layer model is applied. Interestingly, under this circumstance, the impedance spectroscopy is unusual in comparison to the experimental results. Therefore, this work provides an easy way to quantify the battery impedance from fundamental material properties and also shows the perspective to optimize the solid-solid interface. As future work, the MPNP-FBV model can make use of the DFT results on the activation energy for the specific systems. In this sense a multi-scale modelling of impedance can be expected.

7 Conclusions and Outlook

7.1 Conclusion

This thesis is dedicated to enriching the understanding of the intrinsic equilibrium states, the space charge layer impedance, and the reaction kinetics on the high interface impedance of all-solid-state lithium-ion batteries. Even though the extensively applied electrochemical models and the corresponding equivalent circuit models for batteries have been summarized in Chaps. 2 and 3, the innovations of our work are presented as following.

- (1) In all-solid-state batteries, lithium-ion migration relies on the mobile ions hopping through the unoccupied regular lattice sites (defects or vacancies). This unique feature for solids is included in the advanced modified Plank-Nernst-Poisson (MPNP) model.
- (2) Lithium-ions reaction at the interface is constrained by the number available unoccupied lattice sites in materials, thus a new Frumkin-Bulter-Volmer (FBV) equation which includes the vacancy effect is introduced in our model.
- (3) The exchange current is a crucial parameter in the battery modelling and the interface impedance assessment, whereas it is difficult to identify this value by experiments. By using the MPNP-FBV model, the exchange current can be calculated from material properties. Moreover, the interface behaviours at the intrinsic equilibrium state are well explained and provide a perspective to investigate the high interfacial impedance.
- (4) Based on the MPNP model, the corresponding equivalent circuit model are proposed to calculate the solid-state electrolyte impedance. In addition, the analytical solutions for the concentration and the electrostatic potential distributions are proposed. In comparison with other results, the new analytical space charge layer capacitance with the consideration of the vacancy effect shows more accuracy.
- (5) The space charge layer impedance is associated with the charge density and the electric field at the interface or surface, thus it should be frequency-dependent. To address this issue, a new space charge layer resistance has been introduced in the proposed equivalent circuit model.

(6) The charge transfer resistance and the space charge layer impedance at the solid/solid interface rely on the reaction kinetics, nevertheless, the energy parameter is never addressed in the current electrochemical impedance models. Consequently, this work is the first theoretical study that considers reaction kinetics in the battery impedance calculation. Furthermore, the interfacial impedances caused by the reaction are quantified by material properties.

Chaps. 3 to 6 present the numerical results calculated by the introduced MPNP-FBV model and the corresponding equivalent circuit models. To demonstrate the applicability of these models, the numerical results are verified from the chemical and experimental viewpoint. Therefore, this work provides a deeper understanding of the intrinsic equilibrium state and a novel perspective on the microscopic origin of the interfacial impedance. By analysing the results, the conclusions are presented here.

- (1) The vacancy effect in solid-state materials plays an important role in the concentration and the electrostatic potential distributions in the space charge layer. In comparison to the standard PNP-FBV model, the calculated maximum concentration based on the MPNP-FBV model is well constrained and is more physical.
- (2) The interface behaviours at intrinsic equilibrium state are determined by the reaction kinetics and the interface structure. However, the total electrostatic potential drop is only associated with the free enthalpy difference of materials, and is not affected by the different double layer structures.
- (3) The exchange current and the charge transfer resistance can be calculated from material properties through the MPNP-FBV model. Results indicate that lithium-ion diffusion coefficient has no impact on the potential drop and the charge transfer resistance at the interface. Batteries with the diffuse double layer structure have a relatively low exchange current in comparison to that with the compact double layer.
- (4) The analytical space charge layer capacitance based on the MPNP-FBV is more accurate in comparison to other results. Furthermore, the equivalent circuit model with the frequency-dependent space charge layer resistance can well adapt the experimental results, particularly in the low-frequency region.
- (5) It is evident that increasing the free enthalpy difference can significantly reduce the charge transfer resistance. Nevertheless, increasing the large free enthalpy difference can also lead to a large electrostatic potential drop at the interface, which is harmful to the working potential.

7.2 Outlook

In short, all-solid-state lithium-ion batteries have been extensively investigated in this work and other researchers from different perspectives. However, there still exist plentiful open questions and challenges yet to be answered. Based on this dissertation, such aspects can be investigated further to gain a better understanding of solid-state batteries.

- (1) Combining the density functional theory (DFT) calculation with the MPNP-FBV model, thus the new work can be applied to study the specific material or interface. Moreover, the energy parameter and the diffusivity with different temperatures or lattice orientation can be coupled in the proposed model.
- (2) Phase transition, deformation, and cracking within materials during the charging and discharging process may also be included in the MPNP-FBV model.
- (3) Growth of the solid electrolyte interphase (SEI) and lithium-ion dendrite at solid/solid interface can be investigated at a later stage.

Appendix A

The analytical impedance result of an ideally-blocking electrolyte is given in Chap. 5, thus the derivation details are presented in this appendix. The circuit illustration is given by Fig. 7.1

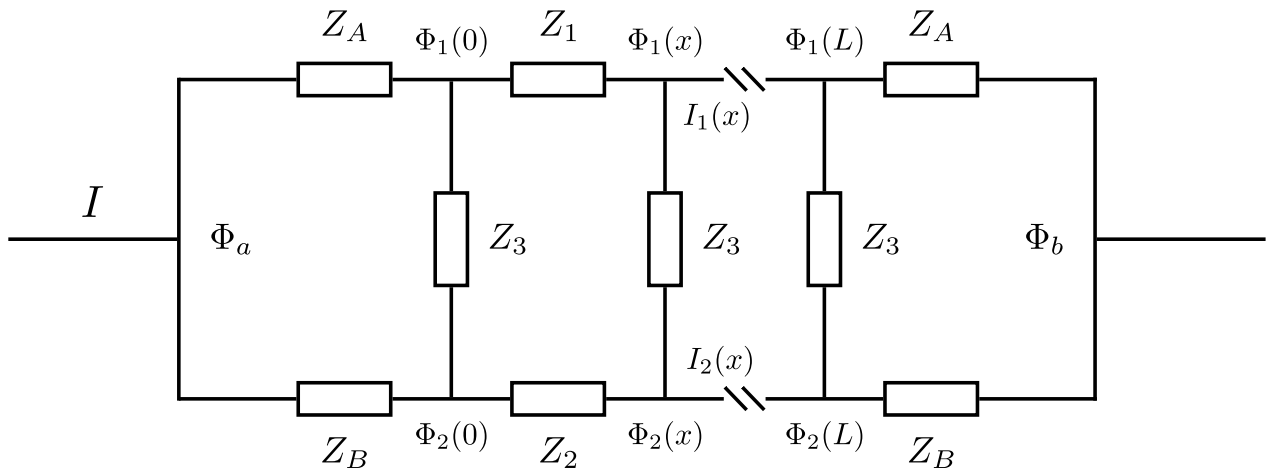


FIGURE 7.1 The equivalent circuit model of a solid-state electrolyte.

Z_A and Z_B represent the interface impedances, Φ_a and Φ_b are the input and output potentials, whereas I is the total current. $\Phi_1(0)$, $\Phi_2(0)$, $\Phi_1(L)$ and $\Phi_2(L)$ are the branch points potentials, I_1 and I_2 are the currents of rails 1 and 2, respectively. Moreover, Z_1 , Z_2 and Z_3 are the unite impedances, and yield

$$Z_1 = Z_1^{total} \frac{dx}{L} \quad (7.1)$$

$$Z_2 = Z_2^{total} \frac{dx}{L} \quad (7.2)$$

$$Z_3 = Z_3^{total} \frac{dx}{L} \quad (7.3)$$

Based on Ohm's law, we can derive

$$\frac{d\Phi_1(x)}{dx} = -\frac{Z_1^{total}(x)}{L} I_1(x) \quad (7.4)$$

$$\frac{d\Phi_2(x)}{dx} = -\frac{Z_2^{total}(x)}{L} I_2(x) \quad (7.5)$$

According to Kirchoff's law

$$\frac{\Phi_1(x) - \Phi_2(x)}{Z_3^{total} L} = -\frac{dI_1(x)}{dx} = \frac{dI_2(x)}{dx} \quad (7.6)$$

$$I = I_1(x) + I_2(x) \quad (7.7)$$

then, Eq. (7.6) yields

$$\frac{d\Phi_1(x)}{dx} - \frac{d\Phi_2(x)}{dx} = -Z_3^{total} L \nabla^2 I_1(x) \quad (7.8)$$

and

$$Z_3^{total} L \nabla^2 I_1(x) - (Z_1^{total} + Z_2^{total}) I_1(x) + Z_2^{total} I = 0 \quad (7.9)$$

Therefore, $I_1(x)$ and $I_2(x)$ can be solved, respectively

$$I_1(x) = \frac{Z_2^{total}}{Z_1^{total} + Z_2^{total}} + Ae^{kx} + Be^{-kx} \quad (7.10)$$

$$I_2(x) = \frac{Z_1^{total}}{Z_1^{total} + Z_2^{total}} - Ae^{kx} - Be^{-kx} \quad (7.11)$$

A, B, k are coefficients. Furthermore, recalling to Eqs. (7.4) and (7.5), $\Phi_1(x)$ and $\Phi_2(x)$ are given by

$$\Phi_1(x) = -\frac{Z_1^{total} Z_2^{total}}{Z_1^{total} + Z_2^{total}} \frac{x}{L} I - \frac{AZ_1^{total}}{kL} e^{kx} + \frac{BZ_1^{total}}{kL} e^{-kx} \quad (7.12)$$

$$\Phi_2(x) = -\frac{Z_1^{total} Z_2^{total}}{Z_1^{total} + Z_2^{total}} \frac{x}{L} I + \frac{AZ_2^{total}}{kL} e^{kx} - \frac{BZ_2^{total}}{kL} e^{-kx} \quad (7.13)$$

In our work, the boundary conditions lead to

$$\Phi_a - \Phi_1(0) = Z_A I_1(0) \quad (7.14)$$

$$\Phi_a - \Phi_2(0) = Z_B I_2(0) \quad (7.15)$$

$$\Phi_1(L) - \Phi_b = 0 \quad (7.16)$$

$$\Phi_2(L) - \Phi_b = 0 \quad (7.17)$$

$$\Phi_a - \Phi_b = Z^{total} I \quad (7.18)$$

Considering Eqs. (7.14) to (7.18), the total impedance Z^{total} is

$$Z^{total} = \frac{Z_1^{total} Z_2^{total}}{Z_1^{total} + Z_2^{total}} + \frac{\tanh(kL)[(Z_1^{total})^2 Z_B + (Z_2^{total})^2 Z_A] + Z_A Z_B (Z_1^{total} + Z_2^{total}) kL}{(Z_1^{total} + Z_2^{total})[\tanh(kL)(Z_1^{total} + Z_2^{total}) + kL(Z_A + Z_B)]} \quad (7.19)$$

where k is

$$k = \sqrt{\frac{Z_1^{total} + Z_2^{total}}{Z_3^{total} L^2}} \quad (7.20)$$

It should be noted that the total impedance has different results when different boundary conditions are applied.

Appendix B

This appendix gives the details for the impedance calculation implementation through the FEM method. In the calculation, the perturbation variables can be written as

$$\Phi = \Phi_{dc} + \Phi_{ac}e^{j\omega_1 t} = \Phi_{dc} + \Phi_{ac}(\cos \omega_1 t + j \sin \omega_1 t) \quad (7.21)$$

$$I = I_{dc} + I_{ac}e^{j\omega_2 t} = I_{dc} + I_{ac}(\cos \omega_2 t + j \sin \omega_2 t) \quad (7.22)$$

$$\tilde{c} = \tilde{c}_{dc} + \tilde{c}_{ac}e^{j\omega_3 t} = \tilde{c}_{dc} + \tilde{c}_{ac}(\cos \omega_3 t + j \sin \omega_3 t) \quad (7.23)$$

ω_1 , ω_2 and ω_3 represent different phase angles, whereas the impedance leads to

$$Z = Z_{re} + jZ_{im} = \frac{\Phi_{ac}(\cos \omega_1 t + j \sin \omega_1 t)}{I_{ac}(\cos \omega_2 t + j \sin \omega_2 t)} \quad (7.24)$$

Therefore, the real and imaginary parts of the impedance can be simplified to Eqs. (7.25) and (7.26), respectively

$$Z_{re} = \frac{\Phi_{ac}(\cos \omega_1 t)I_{ac}(\cos \omega_2 t) + \Phi_{ac}(\sin \omega_1 t)I_{ac}(\sin \omega_2 t)}{[I_{ac}(\cos \omega_2 t)]^2 + [I_{ac}(\sin \omega_2 t)]^2} \quad (7.25)$$

$$Z_{im} = j \frac{\Phi_{ac}(\sin \omega_1 t)I_{ac}(\cos \omega_2 t) - \Phi_{ac}(\cos \omega_1 t)I_{ac}(\sin \omega_2 t)}{[I_{ac}(\cos \omega_2 t)]^2 + [I_{ac}(\sin \omega_2 t)]^2} \quad (7.26)$$

Publication

Publications

- 1) **Y. Liu**, Y.-B. Ma, W. Jaegermann, R. Hausbrand and B.-X. Xu, “Interface Equilibrium Modeling of All-Solid-State Lithium-Ion Thin Film Batteries”, *Journal of Power Sources* 454, 227892 (2020).
- 2) **Y. Liu**, Y. Bai, W. Jaegermann, R. Hausbrand and B.-X. Xu, “Impedance Modeling of Solid-State Electrolytes: Influence of the Contacted Space Charge Layer”, *ACS Applied Materials & Interfaces*, 13, 5895–5906 (2021).
- 3) **Y. Liu**, W.-B. Yu and B.-X. Xu, “Impedance Modeling of Solid-State Electrolytes: Influence of the Reaction Kinetics”, *Journal of Materials Chemistry A*, 10, 313-325 (2022).
- 4) **Y. Liu**, W.-B. Yu and B.-X. Xu, “New Insight into the Interface of TiO₂/C as Nanocomposite Electrode for Lithium-Ion Batteries”, *Journal of Power Sources* (under review).
- 5) T. Frömling, **Y. Liu**, A.-P. Hoang, M. Gehringer, S. Steiner, M. Zhuk, J. Glaum, and B.-X. Xu, “A Chemo-Mechanical Grain Boundary Model and its Application to Understand the Damage of Li-Ion Battery Materials,” *Journal of Materiomics* (<https://doi.org/10.1016/j.jmat.2021.12.005>).
- 6) Y. Bai, K.-J. Zhao, **Y. Liu**, P. Stein, and B.-X. Xu, “A Chemo-Mechanical Grain Boundary Model and its Application to Understand the Damage of Li-Ion Battery Materials,” *Scripta Materialia*, 183, 45-49 (2020).

Conferences with Presentations and Posters

- 1) Materials Science and Engineering Congress, 2018, Darmstadt
- 2) Materials Science and Engineering Congress, 2020, Darmstadt.

Curriculum Vitae

Personal

Yao Liu.

Born on May 2, 1992.

From Wuhan, Hubei Province, China.

Educational background

September, 2016 - Dezember, 2021

Ph.D. Candidate in Materials Science, Technische Universität Darmstadt, Germany

Thesis: Interface Simulation of All-Solid-State Lithium-ion Thin Film Battery

Supervisor: Prof. Dr. Bai-Xiang Xu, Prof. Dr. Wolfram Jaegermann

April, 2021 - Oktober, 2021

Visiting student, Wuhan University of Technology, China

Research: Designing Polymer-in-Salt Electrolyte for Integrated Solid-State Lithium-ion Batteries

September, 2013 - July, 2016

Master in Materials Science, Wuhan University of Technology, China

Thesis: Preparation and Properties of W–SiC/Cu Graded Composites by Tape Casting

Supervisor: Prof. Dr. Lian-Meng Zhang

September, 2009 - July, 2013

Bachelor in Materials Science, Wuhan University of Technology, China

Thesis: The Strength Investigation of ZrO_2/Al_2O_3 Advanced Ceramics

Supervisor: Prof. Dr. Xiao-Hong Xu

Bibliography

- [1] J.-M. Tarascon; M. Armand: “Issues and challenges facing rechargeable lithium batteries”. In: *Materials for sustainable energy: a collection of peer-reviewed research and review articles from Nature Publishing Group*. World Scientific, 2011, pp. 171–179.
- [2] G. Zubi et al.: “The lithium-ion battery: State of the art and future perspectives”. In: *Renewable and Sustainable Energy Reviews* 89 (2018), pp. 292–308.
- [3] X. Luo et al.: “Overview of current development in electrical energy storage technologies and the application potential in power system operation”. In: *Applied energy* 137 (2015), pp. 511–536.
- [4] H. Chen et al.: “Progress in electrical energy storage system: A critical review”. In: *Progress in natural science* 19.3 (2009), pp. 291–312.
- [5] Z. Yang et al.: “Electrochemical energy storage for green grid”. In: *Chemical reviews* 111.5 (2011), pp. 3577–3613.
- [6] W. A. v. S. B. Scrosati: *Advances in lithium-ion batteries*. Springer Science & Business Media, 2002.
- [7] R. Huggins: *Advanced batteries: materials science aspects*. Springer Science & Business Media, 2008.
- [8] F. Cheng et al.: “Functional materials for rechargeable batteries”. In: *Advanced Materials* 23.15 (2011), pp. 1695–1715.
- [9] K. Xu: “Nonaqueous liquid electrolytes for lithium-based rechargeable batteries”. In: *Chemical reviews* 104.10 (2004), pp. 4303–4418.
- [10] A. Manthiram: “An outlook on lithium ion battery technology”. In: *ACS central science* 3.10 (2017), pp. 1063–1069.
- [11] Y.-X. Yin et al.: “Lithium–sulfur batteries: electrochemistry, materials, and prospects”. In: *Angewandte Chemie International Edition* 52.50 (2013), pp. 13186–13200.
- [12] C. F. Francis; I. L. Kyratzis; A. S. Best: “Lithium-Ion Battery Separators for Ionic-Liquid Electrolytes: A Review”. In: *Advanced Materials* 32.18 (2020), p. 1904205.

-
- [13] D. Lin; Y. Liu; Y. Cui: “Reviving the lithium metal anode for high-energy batteries”. In: *Nature nanotechnology* 12.3 (2017), p. 194.
- [14] S. Goriparti et al.: “Review on recent progress of nanostructured anode materials for Li-ion batteries”. In: *Journal of power sources* 257 (2014), pp. 421–443.
- [15] Z. W. Seh et al.: “Designing high-energy lithium–sulfur batteries”. In: *Chemical Society Reviews* 45.20 (2016), pp. 5605–5634.
- [16] J. Janek; W. G. Zeier: “A solid future for battery development”. In: *Nature Energy* 1.9 (2016), pp. 1–4.
- [17] K. Xu: “Electrolytes and interphases in Li-ion batteries and beyond”. In: *Chemical reviews* 114.23 (2014), pp. 11503–11618.
- [18] J. B. Goodenough: “Evolution of strategies for modern rechargeable batteries”. In: *Accounts of chemical research* 46.5 (2013), pp. 1053–1061.
- [19] Y. Zhao et al.: “A chemistry and material perspective on lithium redox flow batteries towards high-density electrical energy storage”. In: *Chemical Society Reviews* 44.22 (2015), pp. 7968–7996.
- [20] T. Famprikis et al.: “Fundamentals of inorganic solid-state electrolytes for batteries”. In: *Nature materials* (2019), pp. 1–14.
- [21] J. C. Pramudita et al.: “An initial review of the status of electrode materials for potassium-ion batteries”. In: *Advanced energy materials* 7.24 (2017), p. 1602911.
- [22] A. Manthiram: “A reflection on lithium-ion battery cathode chemistry”. In: *Nature communications* 11.1 (2020), pp. 1–9.
- [23] A. Manthiram: “Materials challenges and opportunities of lithium ion batteries”. In: *The Journal of Physical Chemistry Letters* 2.3 (2011), pp. 176–184.
- [24] J. B. Goodenough; Y. Kim: “Challenges for rechargeable Li batteries”. In: *Chemistry of materials* 22.3 (2010), pp. 587–603.
- [25] J. B. Goodenough; Y. Kim: “Challenges for rechargeable batteries”. In: *Journal of Power Sources* 196.16 (2011), pp. 6688–6694.
- [26] J. B. Goodenough: “Rechargeable batteries: challenges old and new”. In: *Journal of Solid State Electrochemistry* 16.6 (2012), pp. 2019–2029.
- [27] J. B. Goodenough; K.-S. Park: “The Li-ion rechargeable battery: a perspective”. In: *Journal of the American Chemical Society* 135.4 (2013), pp. 1167–1176.
- [28] R. Hausbrand: *Surface Science of Intercalation Materials and Solid Electrolytes: A View on Electron and Ion Transfer at Li-ion Electrodes Based on Energy Level Concepts*. Springer Nature, 2020.

-
- [29] Q. Zhou et al.: “Intermolecular chemistry in solid polymer electrolytes for high-energy-density lithium batteries”. In: *Advanced Materials* 31.50 (2019), p. 1902029.
- [30] C. Chen; L. Hu: “Nanocellulose toward advanced energy storage devices: structure and electrochemistry”. In: *Accounts of chemical research* 51.12 (2018), pp. 3154–3165.
- [31] L.-Z. Fan; H. He; C.-W. Nan: “Tailoring inorganic–polymer composites for the mass production of solid-state batteries”. In: *Nature Reviews Materials* (2021), pp. 1–17.
- [32] A. Mauger et al.: “Building better batteries in the solid state: A review”. In: *Materials* 12.23 (2019), p. 3892.
- [33] A. Manthiram; X. Yu; S. Wang: “Lithium battery chemistries enabled by solid-state electrolytes”. In: *Nature Reviews Materials* 2.4 (2017), pp. 1–16.
- [34] A. Varzi et al.: “Challenges and prospects of the role of solid electrolytes in the revitalization of lithium metal batteries”. In: *Journal of Materials Chemistry A* 4.44 (2016), pp. 17251–17259.
- [35] J. Li et al.: “Solid electrolyte: the key for high-voltage lithium batteries”. In: *Advanced Energy Materials* 5.4 (2015), p. 1401408.
- [36] B. Zhou et al.: “A flexible, self-healing and highly stretchable polymer electrolyte via quadruple hydrogen bonding for lithium-ion batteries”. In: *Journal of Materials Chemistry A* 6.25 (2018), pp. 11725–11733.
- [37] P. Hu et al.: “Progress in nitrile-based polymer electrolytes for high performance lithium batteries”. In: *Journal of Materials Chemistry A* 4.26 (2016), pp. 10070–10083.
- [38] J. W. Choi; D. Aurbach: “Promise and reality of post-lithium-ion batteries with high energy densities”. In: *Nature Reviews Materials* 1.4 (2016), pp. 1–16.
- [39] W. Zhou et al.: “Rechargeable sodium all-solid-state battery”. In: *ACS central science* 3.1 (2017), pp. 52–57.
- [40] K. Kerman et al.: “practical challenges hindering the development of solid state Li ion batteries”. In: *Journal of The Electrochemical Society* 164.7 (2017), A1731.
- [41] V. Thangadurai; S. Narayanan; D. Pinzaru: “Garnet-type solid-state fast Li ion conductors for Li batteries: critical review”. In: *Chemical Society Reviews* 43.13 (2014), pp. 4714–4727.
- [42] L. Yue et al.: “All solid-state polymer electrolytes for high-performance lithium ion batteries”. In: *Energy Storage Materials* 5 (2016), pp. 139–164.
- [43] X.-B. Cheng et al.: “Recent advances in energy chemistry between solid-state electrolyte and safe lithium-metal anodes”. In: *Chem* 5.1 (2019), pp. 74–96.

-
- [44] P. H. Notten et al.: “3-D integrated all-solid-state rechargeable batteries”. In: *Advanced Materials* 19.24 (2007), pp. 4564–4567.
- [45] E. Quartarone; P. Mustarelli: “Electrolytes for solid-state lithium rechargeable batteries: recent advances and perspectives”. In: *Chemical Society Reviews* 40.5 (2011), pp. 2525–2540.
- [46] C. Sun et al.: “Recent advances in all-solid-state rechargeable lithium batteries”. In: *Nano Energy* 33 (2017), pp. 363–386.
- [47] L. Fan et al.: “Recent progress of the solid-state electrolytes for high-energy metal-based batteries”. In: *Advanced Energy Materials* 8.11 (2018), p. 1702657.
- [48] F. Zheng et al.: “Review on solid electrolytes for all-solid-state lithium-ion batteries”. In: *Journal of Power Sources* 389 (2018), pp. 198–213.
- [49] H.-D. Lim et al.: “A review of challenges and issues concerning interfaces for all-solid-state batteries”. In: *Energy Storage Materials* 25 (2020), pp. 224–250.
- [50] X. He; Y. Zhu; Y. Mo: “Origin of fast ion diffusion in super-ionic conductors”. In: *Nature communications* 8.1 (2017), pp. 1–7.
- [51] S. Hull: “Superionics: crystal structures and conduction processes”. In: *Reports on Progress in Physics* 67.7 (2004), p. 1233.
- [52] Z. Gao et al.: “Promises, challenges, and recent progress of inorganic solid-state electrolytes for all-solid-state lithium batteries”. In: *Advanced materials* 30.17 (2018), p. 1705702.
- [53] B. Zhang et al.: “Mechanisms and properties of ion-transport in inorganic solid electrolytes”. In: *Energy Storage Materials* 10 (2018), pp. 139–159.
- [54] P. P. Kumar; S Yashonath: “Ionic conduction in the solid state”. In: *Journal of Chemical Sciences* 118.1 (2006), pp. 135–154.
- [55] J. W. Perram: *The Physics of superionic conductors and electrode materials*. Vol. 92. Springer Science & Business Media, 2013.
- [56] L. Porz et al.: “Mechanism of lithium metal penetration through inorganic solid electrolytes”. In: *Advanced Energy Materials* 7.20 (2017), p. 1701003.
- [57] A. C. Luntz; J. Voss; K. Reuter: *Interfacial challenges in solid-state Li ion batteries*. 2015.
- [58] S. Stegmaier et al.: “Li⁺ defects in a solid-state Li ion battery: theoretical insights with a Li₃OCl electrolyte”. In: *Chemistry of Materials* 29.10 (2017), pp. 4330–4340.
- [59] D Danilov; R. Niessen; P. Notten: “Modeling all-solid-state Li-ion batteries”. In: *Journal of the Electrochemical Society* 158.3 (2011), A215–A222.

-
- [60] M. Finsterbusch et al.: “High capacity garnet-based all-solid-state lithium batteries: fabrication and 3D-microstructure resolved modeling”. In: *ACS applied materials & interfaces* 10.26 (2018), pp. 22329–22339.
- [61] L. Raijmakers et al.: “An advanced all-solid-state Li-ion battery model”. In: *Electrochimica Acta* 330 (2020), p. 135147.
- [62] K. Becker-Steinberger et al.: “A mathematical model for all solid-state lithium-ion batteries”. In: *ECS Transactions* 25.36 (2010), pp. 285–296.
- [63] R. Xu et al.: “Heterogeneous damage in Li-ion batteries: experimental analysis and theoretical modeling”. In: *Journal of the Mechanics and Physics of Solids* 129 (2019), pp. 160–183.
- [64] R. Behrou; K. Maute: “Numerical modeling of damage evolution phenomenon in solid-state lithium-ion batteries”. In: *Journal of The Electrochemical Society* 164.12 (2017), A2573.
- [65] J. Maier: *Physical chemistry of ionic materials: ions and electrons in solids*. John Wiley & Sons, 2004.
- [66] R. DeHoff: *Thermodynamics in materials science*. CRC Press, 2006.
- [67] M. Z. Bazant: “Theory of chemical kinetics and charge transfer based on nonequilibrium thermodynamics”. In: *Accounts of chemical research* 46.5 (2013), pp. 1144–1160.
- [68] C. Hamann; A. Hamnett; W. Vielstich: *Electrochemistry*. Wiley, 1998. ISBN: 9783527290963. URL: <https://books.google.de/books?id=Ee2YQgAACAAJ>.
- [69] M. Doyle; T. F. Fuller; J. Newman: “Modeling of galvanostatic charge and discharge of the lithium/polymer/insertion cell”. In: *Journal of the Electrochemical society* 140.6 (1993), pp. 1526–1533.
- [70] K. Yamamoto et al.: “Dynamic visualization of the electric potential in an all-solid-state rechargeable lithium battery”. In: *Angewandte Chemie International Edition* 49.26 (2010), pp. 4414–4417.
- [71] N. Sato: *Electrochemistry at metal and semiconductor electrodes*. Elsevier, 1998.
- [72] J. Newman; K. E; Thomas-Alyea: *Electrochemical systems*. John Wiley & Sons, 2012.
- [73] A. Latz; J. Zausch: “Thermodynamic derivation of a Butler–Volmer model for intercalation in Li-ion batteries”. In: *Electrochimica Acta* 110 (2013), pp. 358–362.
- [74] P. Biesheuvel; M Van Soestbergen; M. Bazant: “Imposed currents in galvanic cells”. In: *Electrochimica Acta* 54.21 (2009), pp. 4857–4871.
- [75] X. Han et al.: “Negating interfacial impedance in garnet-based solid-state Li metal batteries”. In: *Nature materials* 16.5 (2017), pp. 572–579.

-
- [76] X.-B. Cheng et al.: “Toward safe lithium metal anode in rechargeable batteries: a review”. In: *Chemical reviews* 117.15 (2017), pp. 10403–10473.
- [77] Y. Zhao; K. Zheng; X. Sun: “Addressing interfacial issues in liquid-based and solid-state batteries by atomic and molecular layer deposition”. In: *Joule* 2.12 (2018), pp. 2583–2604.
- [78] L. Xu et al.: “Interfaces in solid-state lithium batteries”. In: *Joule* 2.10 (2018), pp. 1991–2015.
- [79] B. Put et al.: “Electrical characterization of ultrathin RF-sputtered LiPON layers for nanoscale batteries”. In: *ACS applied materials & interfaces* 8.11 (2016), pp. 7060–7069.
- [80] F. S. Gittleson; F. El Gabaly: “Non-faradaic Li⁺ migration and chemical coordination across solid-state battery interfaces”. In: *Nano letters* 17.11 (2017), pp. 6974–6982.
- [81] N. J. de Klerk; M. Wagemaker: “Space-charge layers in all-solid-state batteries; important or negligible?” In: *ACS applied energy materials* 1.10 (2018), pp. 5609–5618.
- [82] M. Levi; D Aurbach: “Simultaneous measurements and modeling of the electrochemical impedance and the cyclic voltammetric characteristics of graphite electrodes doped with lithium”. In: *The Journal of Physical Chemistry B* 101.23 (1997), pp. 4630–4640.
- [83] P. Taberna; P. Simon; J.-F. Fauvarque: “Electrochemical characteristics and impedance spectroscopy studies of carbon-carbon supercapacitors”. In: *Journal of the Electrochemical Society* 150.3 (2003), A292.
- [84] J. Segalini et al.: “Qualitative electrochemical impedance spectroscopy study of ion transport into sub-nanometer carbon pores in electrochemical double layer capacitor electrodes”. In: *Electrochimica Acta* 55.25 (2010), pp. 7489–7494.
- [85] R. H. Nilson; M. T. Brumbach; B. C. Bunker: “Modeling the electrochemical impedance spectra of electroactive pseudocapacitor materials”. In: *Journal of The Electrochemical Society* 158.6 (2011), A678.
- [86] F. La Mantia; J. Vetter; P. Novák: “Impedance spectroscopy on porous materials: A general model and application to graphite electrodes of lithium-ion batteries”. In: *Electrochimica Acta* 53.12 (2008), pp. 4109–4121.
- [87] J. Zhao et al.: “Kinetic investigation of LiCOO₂ by electrochemical impedance spectroscopy (EIS)”. In: *Int. J. Electrochem. Sci* 5.4 (2010), pp. 478–488.
- [88] S. Dierickx et al.: “Advanced impedance model for double-layered solid oxide fuel cell cermet anodes”. In: *Journal of Power Sources* 415 (2019), pp. 69–82.

-
- [89] S. Braun; C. Yada; A. Latz: “Thermodynamically consistent model for space-charge-layer formation in a solid electrolyte”. In: *The Journal of Physical Chemistry C* 119.39 (2015), pp. 22281–22288.
- [90] M. Fingerle et al.: “Reaction and Space Charge Layer Formation at the LiCoO₂–LiPON Interface: Insights on Defect Formation and Ion Energy Level Alignment by a Combined Surface Science–Simulation Approach”. In: *Chemistry of Materials* 29.18 (2017), pp. 7675–7685.
- [91] P. Schichtel et al.: “On the impedance and phase transition of thin film all-solid-state batteries based on the Li₄Ti₅O₁₂ system”. In: *Journal of Power Sources* 360 (2017), pp. 593–604.
- [92] J. Haruyama et al.: “Space–charge layer effect at interface between oxide cathode and sulfide electrolyte in all-solid-state lithium-ion battery”. In: *Chemistry of Materials* 26.14 (2014), pp. 4248–4255.
- [93] J. Jamnik: “Impedance spectroscopy of mixed conductors with semi-blocking boundaries”. In: *Solid State Ionics* 157.1-4 (2003), pp. 19–28.
- [94] B.-A. Mei et al.: “Physical interpretations of Nyquist plots for EDLC electrodes and devices”. In: *The Journal of Physical Chemistry C* 122.1 (2017), pp. 194–206.
- [95] B.-A. Mei et al.: “Physical interpretations of Nyquist plots for EDLC electrodes and devices”. In: *The Journal of Physical Chemistry C* 122.1 (2018), pp. 194–206.
- [96] J. P. Meyers et al.: “The impedance response of a porous electrode composed of intercalation particles”. In: *Journal of The Electrochemical Society* 147.8 (2000), pp. 2930–2940.
- [97] J. Huang et al.: “Analytical solution to the impedance of electrode/electrolyte interface in lithium-ion batteries”. In: *Journal of The Electrochemical Society* 162.13 (2015), A7037–A7048.
- [98] J. Huang; J. Zhang: “Theory of impedance response of porous electrodes: simplifications, inhomogeneities, non-stationarities and applications”. In: *Journal of the Electrochemical Society* 163.9 (2016), A1983.
- [99] S. Devan; V. R. Subramanian; R. E. White: “Analytical solution for the impedance of a porous electrode”. In: *Journal of The Electrochemical Society* 151.6 (2004), A905.
- [100] C. L. Schmidt; P. M. Skarstad: “Development of an equivalent-circuit model for the lithium/iodine battery”. In: *Journal of power sources* 65.1-2 (1997), pp. 121–128.
- [101] B. Y. Liaw et al.: “Modeling of lithium ion cells—A simple equivalent-circuit model approach”. In: *Solid state ionics* 175.1-4 (2004), pp. 835–839.

-
- [102] C. Zhang et al.: “Online estimation of battery equivalent circuit model parameters and state of charge using decoupled least squares technique”. In: *Energy* 142 (2018), pp. 678–688.
- [103] P. Gao; C. Zhang; G. Wen: “Equivalent circuit model analysis on electrochemical impedance spectroscopy of lithium metal batteries”. In: *Journal of Power Sources* 294 (2015), pp. 67–74.
- [104] J. Gomez et al.: “Equivalent circuit model parameters of a high-power Li-ion battery: Thermal and state of charge effects”. In: *Journal of Power Sources* 196.10 (2011), pp. 4826–4831.
- [105] S Larfaillou et al.: “Comprehensive characterization of all-solid-state thin films commercial microbatteries by Electrochemical Impedance Spectroscopy”. In: *Journal of Power Sources* 319 (2016), pp. 139–146.
- [106] J. Bates et al.: “Fabrication and characterization of amorphous lithium electrolyte thin films and rechargeable thin-film batteries”. In: *Journal of power sources* 43.1-3 (1993), pp. 103–110.
- [107] L. Le Van-Jodin et al.: “Dielectric properties, conductivity and Li⁺ ion motion in LiPON thin films”. In: *Solid State Ionics* 253 (2013), pp. 151–156.
- [108] F. Han et al.: “High electronic conductivity as the origin of lithium dendrite formation within solid electrolytes”. In: *Nature Energy* 4.3 (2019), pp. 187–196.
- [109] W. Lai; S. M. Haile: “Impedance spectroscopy as a tool for chemical and electrochemical analysis of mixed conductors: a case study of ceria”. In: *Journal of the American Ceramic Society* 88.11 (2005), pp. 2979–2997.
- [110] J. Jamnik; J. Maier: “Treatment of the impedance of mixed conductors equivalent circuit model and explicit approximate solutions”. In: *Journal of the Electrochemical society* 146.11 (1999), pp. 4183–4188.
- [111] H. Wang; L. Pilon: “Intrinsic limitations of impedance measurements in determining electric double layer capacitances”. In: *Electrochimica Acta* 63 (2012), pp. 55–63.
- [112] J. Song; M. Z. Bazant: “Effects of nanoparticle geometry and size distribution on diffusion impedance of battery electrodes”. In: *Journal of The Electrochemical Society* 160.1 (2013), A15–A24.
- [113] J. Jamnik; J. Maier: “Generalised equivalent circuits for mass and charge transport: chemical capacitance and its implications”. In: *Physical Chemistry Chemical Physics* 3.9 (2001), pp. 1668–1678.

-
- [114] H. Wang; L. Pilon: “Accurate simulations of electric double layer capacitance of ultra-microelectrodes”. In: *The Journal of Physical Chemistry C* 115.33 (2011), pp. 16711–16719.
- [115] A. J. Bard; L. R. Faulkner, et al.: “Fundamentals and applications”. In: *Electrochemical Methods* 2.482 (2001), pp. 580–632.
- [116] V. S. Bagotsky: Fundamentals of electrochemistry. Vol. 44. John Wiley & Sons, 2005.
- [117] H.-J. Butt; M. Kappl, et al.: Surface and interfacial forces. Wiley Online Library, 2010.
- [118] J. H. Masliyah; S. Bhattacharjee: Electrokinetic and colloid transport phenomena. John Wiley & Sons, 2006.
- [119] M Schönleber et al.: “A consistent derivation of the impedance of a lithium-ion battery electrode and its dependency on the state-of-charge”. In: *Electrochimica Acta* 243 (2017), pp. 250–259.
- [120] J. Song; M. Z. Bazant: “Effects of nanoparticle geometry and size distribution on diffusion impedance of battery electrodes”. In: *Journal of The Electrochemical Society* 160.1 (2012), A15.
- [121] D. R. Franceschetti; J. R. Macdonald; R. P. Buck: “Interpretation of Finite-Length-Warburg-Type Impedances in Supported and Unsupported Electrochemical Cells with Kinetically Reversible Electrodes”. In: *Journal of the Electrochemical Society* 138.5 (1991), p. 1368.
- [122] S. Sunde et al.: “An impedance model for a porous intercalation electrode with mixed conductivity”. In: *Journal of the Electrochemical Society* 156.8 (2009), B927.
- [123] A. Lasia: “Electrochemical impedance spectroscopy and its applications”. In: *Modern aspects of electrochemistry*. Springer, 2002, pp. 143–248.
- [124] J. B. Allen; R. F. Larry: Electrochemical methods fundamentals and applications. John Wiley & Sons, 2001.
- [125] M. Levi; D Aurbach: “Impedance of a single intercalation particle and of non-homogeneous, multilayered porous composite electrodes for Li-ion batteries”. In: *The Journal of Physical Chemistry B* 108.31 (2004), pp. 11693–11703.
- [126] J. Jamnik; J. Maier; S. Pejovnik: “Interfacial impedance of the boundary Ag/AgCl and its investigations by a novel method”. In: *Solid State Ionics* 80.1-2 (1995), pp. 19–26.
- [127] J. Jamnik; S. Pejovnik; J. Maier: “A new approach for the computation of the frequency response of space charge-containing interfaces”. In: *Electrochimica acta* 38.14 (1993), pp. 1975–1978.
- [128] Y. Hamon et al.: “Influence of sputtering conditions on ionic conductivity of LiPON thin films”. In: *Solid State Ionics* 177.3-4 (2006), pp. 257–261.

-
- [129] P. Knauth: “Inorganic solid Li ion conductors: An overview”. In: *Solid State Ionics* 180.14-16 (2009), pp. 911–916.
- [130] M. Okubo et al.: “Determination of activation energy for Li ion diffusion in electrodes”. In: *The Journal of Physical Chemistry B* 113.9 (2009), pp. 2840–2847.
- [131] M. Landstorfer; S. Funken; T. Jacob: “An advanced model framework for solid electrolyte intercalation batteries”. In: *Physical Chemistry Chemical Physics* 13.28 (2011), pp. 12817–12825.
- [132] S. D. Fabre et al.: “Charge/discharge simulation of an all-solid-state thin-film battery using a one-dimensional model”. In: *Journal of the Electrochemical Society* 159.2 (2011), A104–A115.
- [133] A. Schwöbel; W. Jaegermann; R. Hausbrand: “Interfacial energy level alignment and energy level diagrams for all-solid Li-ion cells: Impact of Li-ion transfer and double layer formation”. In: *Solid State Ionics* 288 (2016), pp. 224–228.
- [134] R. Hausbrand et al.: “Energy level offsets and space charge layer formation at electrode-electrolyte interfaces: X-ray photoelectron spectroscopy analysis of Li-ion model electrodes”. In: *Thin Solid Films* 643 (2017), pp. 43–52.
- [135] S. Schuld et al.: “Experimental studies on work functions of Li⁺ ions and electrons in the battery electrode material LiCoO₂: a thermodynamic cycle combining ionic and electronic structure”. In: *Advanced Energy Materials* 8.18 (2018), p. 1703411.
- [136] R. Hausbrand et al.: “Surface and bulk properties of Li-ion electrodes—A surface science approach”. In: *Journal of Electron Spectroscopy and Related Phenomena* 221 (2017), pp. 65–78.
- [137] M. Rossi et al.: “Modeling and simulation of electrochemical cells under applied voltage”. In: *Electrochimica Acta* 258 (2017), pp. 241–254.
- [138] R. Hausbrand et al.: “Surface and interface analysis of LiCoO₂ and LiPON thin films by photoemission: Implications for Li-Ion batteries”. In: *Zeitschrift für Physikalische Chemie* 229.9 (2015), pp. 1387–1414.
- [139] Z. Wang et al.: “Effects of cathode electrolyte interfacial (CEI) layer on long term cycling of all-solid-state thin-film batteries”. In: *Journal of Power Sources* 324 (2016), pp. 342–348.
- [140] S. Rodrigues; N. Munichandraiah; A. Shukla: “AC impedance and state-of-charge analysis of a sealed lithium-ion rechargeable battery”. In: *Journal of Solid State Electrochemistry* 3.7-8 (1999), pp. 397–405.

-
- [141] M. Ardani et al.: “Combined experimental and numerical evaluation of the differences between convective and conductive thermal control on the performance of a lithium ion cell”. In: *Energy* 144 (2018), pp. 81–97.
- [142] T. Ohzuku; A. Ueda: “Phenomenological Expression of Solid-State Redox Potentials of LiCoO_2 , $\text{LiCo}_{1/2}\text{Ni}_{1/2}\text{O}_2$, and LiNiO_2 Insertion Electrodes”. In: *Journal of the Electrochemical Society* 144.8 (1997), pp. 2780–2785.
- [143] M Van Soestbergen; P. Biesheuvel; M. Bazant: “Diffuse-charge effects on the transient response of electrochemical cells”. In: *Physical Review E* 81.2 (2010), p. 021503.
- [144] J. R. MacDonald: “Theory of space-charge polarization and electrode-discharge effects”. In: *The Journal of Chemical Physics* 58.11 (1973), pp. 4982–5001.
- [145] D. Gaston et al.: “MOOSE: A parallel computational framework for coupled systems of nonlinear equations”. In: *Nuclear Engineering and Design* 239.10 (2009), pp. 1768–1778.
- [146] C. Nimisha et al.: “Sputter deposited LiPON thin films from powder target as electrolyte for thin film battery applications”. In: *Thin Solid Films* 519.10 (2011), pp. 3401–3406.
- [147] X. Yu et al.: “A stable thin-film lithium electrolyte: lithium phosphorus oxynitride”. In: *Journal of the electrochemical society* 144.2 (1997), p. 524.
- [148] J. Maier: “On the conductivity of polycrystalline materials”. In: *Berichte der Bunsengesellschaft für physikalische Chemie* 90.1 (1986), pp. 26–33.
- [149] J. Jamnik; H.-U. Habermeier; J. Maier: “Information of ionic boundary effects by a novel penetration impedance technique”. In: *Physica B: Condensed Matter* 204.1-4 (1995), pp. 57–64.
- [150] J. Jamnik: “Impact of particle size on conductivity and storage capacity as derived from the core–space charge model”. In: *Solid State Ionics* 177.26-32 (2006), pp. 2543–2547.
- [151] N. Goswami; R. Kant: “Theory for impedance response of grain and grain boundary in solid state electrolyte”. In: *Journal of Electroanalytical Chemistry* 835 (2019), pp. 227–238.
- [152] Y.-H. Liu; K. T. Chen; B. H. Liu: “Fabrication of composite probe electrode used for localized impedance analysis of solid-state electrolyte LATP”. In: *Solid State Ionics* 336 (2019), pp. 11–18.
- [153] Y. Zhu et al.: “Reduced Energy Barrier for Li^+ Transport Across Grain Boundaries with Amorphous Domains in LLZO Thin Films”. In: *Nanoscale research letters* 15.1 (2020), pp. 1–8.
- [154] C. Mariappan; G Govindaraj: “Conductivity and ion dynamic studies in the $\text{Na}_{4.7+x}\text{Ti}_{1.3-x}(\text{PO}_4)_{3.3-x}$ ($0 \leq x \leq 0.6$) NASICON material”. In: *Solid state ionics* 176.13-14 (2005), pp. 1311–1318.

-
- [155] J. C. Dyre et al.: “Fundamental questions relating to ion conduction in disordered solids”. In: *Reports on Progress in Physics* 72.4 (2009), p. 046501.
- [156] D Bérardan et al.: “Room temperature lithium superionic conductivity in high entropy oxides”. In: *Journal of Materials Chemistry A* 4.24 (2016), pp. 9536–9541.
- [157] C. Choi et al.: “Radio-frequency magnetron sputtering power effect on the ionic conductivities of LiPON films”. In: *Electrochemical and solid-state letters* 5.1 (2002), A14–A17.
- [158] R. Xu et al.: “Interfacial challenges and progress for inorganic all-solid-state lithium batteries”. In: *Electrochimica Acta* 284 (2018), pp. 177–187.
- [159] S. A. Pervez et al.: “Interface in solid-state lithium battery: challenges, progress, and outlook”. In: *ACS applied materials & interfaces* 11.25 (2019), pp. 22029–22050.
- [160] Y. Liu et al.: “Interface equilibrium modeling of all-solid-state lithium-ion thin film batteries”. In: *Journal of Power Sources* 454 (2020), p. 227892.
- [161] Y. Liu et al.: “Impedance Modeling of Solid-State Electrolytes: Influence of the Contacted Space Charge Layer”. In: *ACS Applied Materials & Interfaces* (2021).
- [162] J. Maier: “Chemical resistance and chemical capacitance”. In: *Zeitschrift für Naturforschung B* 75.1-2 (2020), pp. 15–22.
- [163] X. Wang; X. Wei; H. Dai: “Estimation of state of health of lithium-ion batteries based on charge transfer resistance considering different temperature and state of charge”. In: *Journal of Energy Storage* 21 (2019), pp. 618–631.
- [164] J. Illig et al.: “Separation of charge transfer and contact resistance in LiFePO₄-cathodes by impedance modeling”. In: *Journal of the Electrochemical Society* 159.7 (2012), A952.
- [165] J. Jamnik; J. Maier; S. Pejovnik: “Interfaces in solid ionic conductors: Equilibrium and small signal picture”. In: *Solid State Ionics* 75 (1995), pp. 51–58.
- [166] J. Maier: “Ionic conduction in space charge regions”. In: *Progress in solid state chemistry* 23.3 (1995), pp. 171–263.
- [167] M. Schleutker et al.: “On the interfacial charge transfer between solid and liquid Li⁺ electrolytes”. In: *Physical Chemistry Chemical Physics* 19.39 (2017), pp. 26596–26605.
- [168] D. Morgan; A. Van der Ven; G. Ceder: “Li conductivity in Li_xMPO₄ (M= Mn, Fe, Co, Ni) olivine materials”. In: *Electrochemical and Solid State Letters* 7.2 (2003), A30.
- [169] T. Maxisch; F. Zhou; G. Ceder: “Ab initio study of the migration of small polarons in olivine Li_xFePO₄ and their association with lithium ions and vacancies”. In: *Physical review B* 73.10 (2006), p. 104301.

-
- [170] C. Ouyang et al.: “First-principles study of Li ion diffusion in LiFePO₄”. In: *Physical Review B* 69.10 (2004), p. 104303.
- [171] J. Li et al.: “Lithium ion conductivity in single crystal LiFePO₄”. In: *Solid State Ionics* 179.35-36 (2008), pp. 2016–2019.
- [172] G. Xu et al.: “First-principles investigation of the electronic and Li-ion diffusion properties of LiFePO₄ by sulfur surface modification”. In: *Journal of Applied Physics* 116.6 (2014), p. 063703.